# SINGLE MOLECULE STUDIES OF MESO/MACRO POROUS SILICA MATERIALS AND GRADIENT FILMS

by

FANGMAO YE

B.E., Hefei University of Technology, 2001

M.S., University of Science and Technology of China, 2004

AN ABSTRACT OF A DISSERTATION

submitted in partial fulfillment of the requirements for the degree

DOCTOR OF PHILOSOPHY

Department of Chemistry
College of Arts and Sciences

KANSAS STATE UNIVERSITY
Manhattan, Kansas

2009

# Abstract

The preparation of mesoporous/macroporous silica materials and polarity gradient thin film are introduced in this thesis. These porous silica materials and gradient materials have the potential applications as stationary phases for chemical separations, as materials for combinatorial catalysis and as absorbent/adsorbent layers for use in chemical or biological sensors. Single molecule spectroscopy is used to probe the chemical interaction between single dye molecule and porous silica matrix. Bulk fluorescence spectroscopy is used to investigate the properties of gradient film.

In Chapter one, the applications of single molecule spectroscopic methods to sol-gel silica materials are reviewed, which covers a subset of the recent literature in this area and provided salient examples of the new information that can be obtained by single molecule studies.

In Chapter two, both the sample preparation and experiment setup are covered.

In Chapter three, the preparation of mesoporous silica film is presented. Single molecule spectroscopy is used to probe the mass transport and molecule-matrix interactions in mesoporous thin-film systems. Three different dyes of varying size, charge, and hydrophilicity are used. Silica films with/without surfactant or containing different kind surfactant are studied. The results provide new information on mass transport through the films, evidence of reversible surface adsorption, and quantitative information on variations in these phenomena with film hydration.

In Chapter four, a new model describing how to explore the actual dye concentration in single molecule experiment with considering the molecule orientation is presented, which is verified to be correct by both experimental and simulated data.

In Chapter five, the growth process of Methylsilsesquioxane (MSQ) particle is studied by single molecule spectroscopy, in which, the MSQ particle is treated as “native” dye molecule.

In Chapter six, silica films incorporating polarity gradients are produced by using “infusion-withdrawal dip-coating” method. The gradient film is characterized by bulk fluorescence spectroscopy, water contact angle and FTIR.

In Chapter seven, a brief conclusion is drawn and future directions are presented.

# SINGLE MOLECULE STUDIES OF MESO/MACRO POROUS SILICA MATERIALS AND GRADIENT FILMS

by

FANGMAO YE

B.E., Hefei University of Technology, 2001

M.S., University of Science and Technology of China, 2004

A DISSERTATION

submitted in partial fulfillment of the requirements for the degree

DOCTOR OF PHILOSOPHY

Department of Chemistry
College of Arts and Sciences

KANSAS STATE UNIVERSITY
Manhattan, Kansas

2009

Approved by:

Major Professor
Daniel. A. Higgins

# Abstract

The preparation of mesoporous/macroporous silica materials and polarity gradient thin film are introduced in this thesis. These porous silica materials and gradient materials have the potential applications as stationary phases for chemical separations, as materials for combinatorial catalysis and as absorbent/adsorbent layers for use in chemical or biological sensors. Single molecule spectroscopy is used to probe the chemical interaction between single dye molecule and porous silica matrix. Bulk fluorescence spectroscopy is used to investigate the properties of gradient film.

In Chapter one, the applications of single molecule spectroscopic methods to sol-gel silica materials are reviewed, which covers a subset of the recent literature in this area and provided salient examples of the new information that can be obtained by single molecule studies.

In Chapter two, both the sample preparation and experiment setup are covered.

In Chapter three, the preparation of mesoporous silica film is presented. Single molecule spectroscopy is used to probe the mass transport and molecule-matrix interactions in mesoporous thin-film systems. Three different dyes of varying size, charge, and hydrophilicity are used. Silica films with/without surfactant or containing different kind surfactant are studied. The results provide new information on mass transport through the films, evidence of reversible surface adsorption, and quantitative information on variations in these phenomena with film hydration.

In Chapter four, a new model describing how to explore the actual dye concentration in single molecule experiment with considering the molecule orientation is presented, which is verified to be correct by both experimental and simulated data.

In Chapter five, the growth process of Methylsilsesquioxane (MSQ) particle is studied by single molecule spectroscopy, in which, the MSQ particle is treated as “native” dye molecule.

In Chapter six, silica films incorporating polarity gradients are produced by using “infusion-withdrawal dip-coating” method. The gradient film is characterized by bulk fluorescence spectroscopy, water contact angle and FTIR.

In Chapter seven, a brief conclusion is drawn and future directions are presented.

# Table of Contents

# List of Figures

# List of Tables

# Acknowledgements

It's been my great honor to have Dr. Daniel A Higgins be my major professor. He is responsible, smart, honest and diligent. He has endless motivation and enthusiasm in research. He aims high and works hard and always has good gains. He keeps encouraging me when I felt frustrated in research. What he taught and influenced me will benefit me the rest of my life.

I would like to thank Dr. Maryanne M Collinson for teaching me a lot in sol-gel chemistry. Dr. Yi Fu, Dr. Hanjiang Dong and Dr. Dong Dong are thanked for their great help in my research. I also thank all my group members: Aifang, Bei, Tom, Jeff, Chenchen, Xiao, Corey and Amer.

My committee members are highly appreciated for their great assistance throughout the degree process. They are Dr. Christopher Culbertson, Dr. Stefan Bossmann, Dr. Keith Hohn and Dr. Rollie Clem.

Finally, I would like to appreciate my wife for her support and help. My special thanks also go to my parents, my sister, my brother and all my friends.

# Dedication

This thesis is dedicated to my newlywed wife

Xiaofan Yang

# List of Abbreviations

| | |
|---|---|
| SMS | Single molecule spectroscopy |
| FCS | Fluorescence correlation spectroscopy |
| SMT | Single molecule tracking |
| TEM | Transmission electron microscopy |
| XRD | X-ray diffraction |
| TMOS | Tetramethoxysilane |
| BTMOS | Isobutyltrimethoxysilane |
| TEOS | Tetraethoxysilane |
| MTMOS | Methyltrimethoxysilane |
| APTEOS | 3-amino-propyltriethoxysilane |
| MSQ | Methylsilsesquioxane |
| ORMOSIL | Organically modified silica |
| CTAB | Cetyltrimethylammonium bromide |
| SDS | Sodium dodecyl sulfate |
| NR | Nile Red |
| R6G | Rhodamine 6G |
| DiI | 1,1'-dihexadecyl-3,3,3',3'-tetramethylindocarbocyanine perchlorate |
| SPDI | N,N'-bis(3-sulfonatopropyl)perylene-3,4,9,10-tetracarboxylic diimide |
| TDI | Terrylenediimide |
| ORG | Oregon green 514 |

# CHAPTER 1 - What Can Be Learned from Single Molecule Spectroscopy? Applications to Sol-Gel-Derived Silica Materials

This chapter has been published in the journal of *Physical Chemistry and Chemical Physics* under the following citation:

Fangmao Ye, Maryanne M. Collinson* and Daniel A. Higgins* "What Can Be Learned from Single Molecule Spectroscopy? Applications to Sol-Gel-Derived Silica Materials", *Physical Chemistry and Chemical Physics*, **2009**, 11, 66-82.

## 1.1 Introduction

Sol-gel-derived materials find numerous applications in a variety of fields, having been used in chemical sensors,[1-3] catalysts,[4,5] separations media,[6-8] ion-exchange coatings,[9,10] nonlinear optics[11] and solid state electrochemical devices.[12,13] Key advantages of the sol-gel process are its economy and the relative simplicity of materials preparation and modification. Typically, silica materials are prepared via acid- or base-catalyzed hydrolysis and condensation of alkoxysilanes such as tetramethoxysilane (TMOS)[14,15] in homogeneous mixtures of alcohol and water. The mild polymerization conditions (the reaction is often run at room temperature) make it possible to encapsulate many different reagents (enzymes, receptors, catalysts, dyes, cells etc.)[1-3,16-19] within the silica matrix while retaining these reagents' desired functional characteristics after gelation.

Silica materials can also be prepared, in whole or in part, from organoalkoxysilanes, which can act as network modifiers.[20-27] The resulting materials have been termed organically modified silicas (ORMOSILs).[24] The preparation of ORMOSILs allows for further control over the physical properties and chemical composition of the final materials.[20-23,25-27] Sol-gel-prepared silica materials can also be modified by reaction with organosilanes, using well-known post-synthesis procedures.[28]

While relatively simple to make, sol-gel materials are microscopically complex and thus require sophisticated tools to unravel this complexity. To date, many different methods have been used to follow the hydrolysis and condensation processes in sols prepared from both alkoxy- and organoalkoxysilanes, and to study the physical and chemical properties of the resulting gels.[14] The vast majority of these can be classified as bulk techniques. They include NMR,[29] X-ray scattering,[30] gas adsorption,[31] Raman[31] and FTIR[32] spectroscopies,

electrochemical methods,[26,33] UV-vis absorption[34,35] and fluorescence spectroscopies.[17,35-37] Such bulk studies have provided many useful insights into the average chemical and physical properties of sol-gel materials. However, almost all such materials are heterogeneous, exhibiting variations on nanometer (and longer) length scales in terms of their acidity, polarity, porosity, surface charge and other properties. Importantly, such variations may not be random, leading to certain classes of heterogeneity (i.e. due to phase separation, domain formation, etc.) that may be masked, overlooked or otherwise misinterpreted when observed by bulk methods alone.

A number of research groups have recently begun to use single molecule spectroscopic methods as a means to better understand the impacts of nanoscale heterogeneity on the properties of sol-gel-derived silica materials. Single molecule fluorescence experiments probe many of the same phenomena probed by bulk methods, while also providing detailed new information about individual nanoscale environments and materials microheterogeneity.[34,35,38-42] In such studies, the silica materials are investigated by doping them with very low (i.e. nanomolar) concentrations of fluorescent dyes. The dye molecules are then spatially isolated from each other using sample scanning, beam scanning, or wide-field optical microscopy methods and their emission characteristics probed.[40] Since individual molecules and/or individual nanoscale environments are interrogated one at a time in single molecule experiments, detailed new information on the variations in materials properties is obtained. By judicious choice of the probe molecule, materials properties such as surface charge, surface silanol density, matrix polarity and matrix acidity can be investigated. By recording the translational or rotational motions of charged or neutral dyes of different sizes, molecular mobility within these materials can also be explored.

This chapter is focused specifically on the use of single molecule fluorescence microscopy and spectroscopy as means to probe sol-gel-derived silica materials. The purpose is

to provide representative examples of the experiments that have been performed to date and the important new knowledge that has been gained. Pioneering studies of similar materials prepared by other methods are not included.[43-46] This chapter begins with a discussion of the sol-gel process. The majority of the discussion is then devoted to reviewing studies of molecule-matrix interactions, molecular mobility and other silica materials properties by single molecule methods. It concludes with a brief discussion of challenges and future directions.

## 1.2. Materials Synthesis

### *1.2.1 The Sol-gel Process*

Scheme 1.1 depicts a representative view of some of the processes that occur during the acid-catalyzed hydrolysis and condensation of TMOS.[14,15]

$$Si(OMe)_4 + H_2O + H^+ \xrightarrow{\text{Hydrolysis}} Si(OMe)_{4-n}(OH)_n + n\ MeOH$$

$$2\ Si(OMe)_{4-n}(OH)_n \xrightarrow{\text{Condensation}} (OH)_{n-1}(OMe)_{4-n}Si\text{-}O\text{-}Si(OMe)_{4-n}(OH)_{n-1} + H_2O$$

**Scheme 1.1.** Salient processes involved in the acid-catalyzed hydrolysis and condensation of TMOS.

Hydrolysis and condensation of the precursor begins immediately after preparation of the sol. As hydrolysis and condensation proceed, a rigid silica matrix, the gel, is formed. The final structure, morphology and porosity of the gel are highly dependent upon the ratio of precursor silane to water, the nature (acid or base) and concentration of the catalyst, and how the materials are processed and dried.[14,15,47] In acid-catalyzed processes, the precursors tend to form highly crosslinked networks of relatively low porosity, while in base-catalyzed preparations, colloidal particles are produced that subsequently aggregate and react to give xerogels (dried gels) that

have greater interstitial porosity.[14] Two-step acid-base procedures have also been developed to take advantage of the benefits of both methods.[48]

### *1.2.2 Organically Modified Silicas (ORMOSIL)*

ORMOSILs[20-23,25-27] are typically prepared via the cohydrolysis and condensation of the alkoxysilanes (such as TMOS) with organoalkoxysilanes. In this chapter, the focus is entirely on these so-called Type II ORMOSILs.[23] Typical precursors are represented as R'-Si$(OR)_3$, where R is typically methyl or ethyl and R' can be virtually any organic group, including methyl, ethyl, phenyl and acid- or amine-terminated substituents. Use of these precursors allows for control over the degree of crosslinking in the gel, and the reactivity, polarity, surface charge, acid/base properties, etc. of the pores found within. A distinct advantage of ORMOSIL methods is that the organic functional groups are covalently attached to and dispersed throughout the silicate framework. Covalent attachment of organic substituents to the external and internal (pore) surfaces can also be accomplished after synthesis by further reaction with species such as organically modified chlorosilanes.[28] ORMOSILs have recently been shown to be useful in the preparation of superhydrophobic materials,[49] and as platforms for biomolecule immobilization.[1-3,17]

### *1.2.3 Surfactant Templated Mesoporous Materials*

Mesoporous silica materials that contain pores of controlled size and organization can also be prepared by the sol-gel process by utilizing surfactants as "site-directing agents."[50,51] Lamellar, cubic or hexagonal ordering of ~ 2-50 nm sized pores/channels within the resulting gel can be achieved.[52,53] Pore size and organization are determined by the chemical structure and concentration of the specific surfactants employed.[54]

Surfactant-containing mesoporous silica can be used and/or characterized without further modification, with the surfactant phase providing hydrophobic channels that facilitate transport of some molecules and strongly adsorb others.[55-57] More commonly, they are calcined or Soxhlet-extracted to remove the surfactant, leading to formation of purely inorganic mesoporous silica. Removal of the surfactant may lead to pore collapse and an increase in materials disorder.[52] The surfaces of mesoporous silicas can also be further derivatized with organic functional groups in-situ or ex-situ to control pore surface properties.[28]

### *1.2.4 Silica Monoliths and Thin Films*

Sol-gel derived silica materials may be prepared as monoliths (bulk gels) or thin films. Monoliths are prepared by pouring the sol into a macroscopic vessel. Upon gelation a porous, solvent-filled gel is produced that is the same size and shape as the vessel. Upon drying, a xerogel is formed.[47] Thin films are commonly prepared on planar substrates by aerosol methods,[58] spin coating,[59]dip coating,[59,60] or electrochemical deposition,[33] and are typically less than 1 μm thick.[47] Silica thin films are often significantly less porous than corresponding monoliths because gelation and evaporation in films occur simultaneously in a very short period of time (seconds).[47] In monolith formation these processes take place over a substantially longer period (days to weeks).[47] The thin film configuration is most often used in sensing applications because of the short path length for diffusion.[47] Although exceptions exist,[61] the vast majority of single molecule studies have been performed on silica films, and such films will be the primary focus of the discussion below.

## 1.3. Single Molecule Studies of Sol-gel-derived Materials

Single molecule studies of sol-gel-derived materials provide distinct advantages over similar bulk investigations in that they allow for materials heterogeneity to be directly probed

and individual chemical events and molecular-scale environments (including rare ones) to be observed and characterized. Taken together, the range of ongoing bulk and single molecule studies promises a more complete, in-depth understanding of molecule-matrix interactions, mass transport phenomena and matrix polarity, acidity and porosity properties of silica materials.

### *1.3.1 Single Molecule Spectroscopic and Microscopic Methods*

Single molecule fluorescence experiments are most commonly performed by sample-scanning or beam-scanning confocal microscopy or by wide-field imaging methods.[38-42,61] To detect single molecules, the molecules must be spatially isolated from each other, although early work relied on spectral isolation.[62,63] To achieve spatial isolation, the samples to be investigated are doped to very low dye concentrations (i.e., 0.01~1nM). An ultra small detection volume (~1 fL) is then attained by using a high numerical aperture microscope objective for illumination of the sample and collection of the resulting fluorescence. The combination of low dye concentration and small detection volume makes it possible to detect the fluorescence from one molecule at a time. The use of thin silica films also facilitates single molecule detection by further restricting the volume probed.[64] Out-of-focus background due to light scattering by the sample or emission from molecules at different sample depths is virtually eliminated with thin films. Background reduction in this case can easily exceed that afforded by confocal detection methods for thicker samples.[40]

In a typical single molecule experiment, the individual molecules are first located by recording a fluorescence image of a portion (a few hundred square micrometers) of the sample. The single molecules frequently appear in such images as bright round fluorescent spots of diffraction-limited size and comprising Gaussian intensity profiles. In sample-scanning experiments, these spots (single molecules) are subsequently positioned one at a time in the

detection volume of the microscope and their time-resolved and/or spectrally-resolved emission characteristics are recorded. In wide-field experiments, repeated images of the same area are recorded to follow the motions of the individual molecules in time and space. Both confocal and wide-field experiments can also be performed with spectral and polarization selectivity to monitor energy transfer between molecules (i.e. as in fluorescence resonance energy transfer experiments)[65] and orientational motions of the individual molecules, respectively.[56,66,67]

Single molecule experiments require selection of appropriate dye molecules. The dye molecules to be employed must have large excitation cross-sections (~ $3x10^{-16}$ $cm^2$ or larger) and high fluorescence quantum yields (~ 20% or larger). They must also be relatively photostable (i.e. capable of surviving millions of excitation/emission cycles). Finally, to serve as probes of materials properties, they must exhibit some sensitivity to the property of interest (i.e. pH, polarity, ionic interactions, pore size, etc.). Figure 1.1 depicts the chemical structures of representative dyes that have been used in single molecule studies of sol-gel-derived silica materials to date.

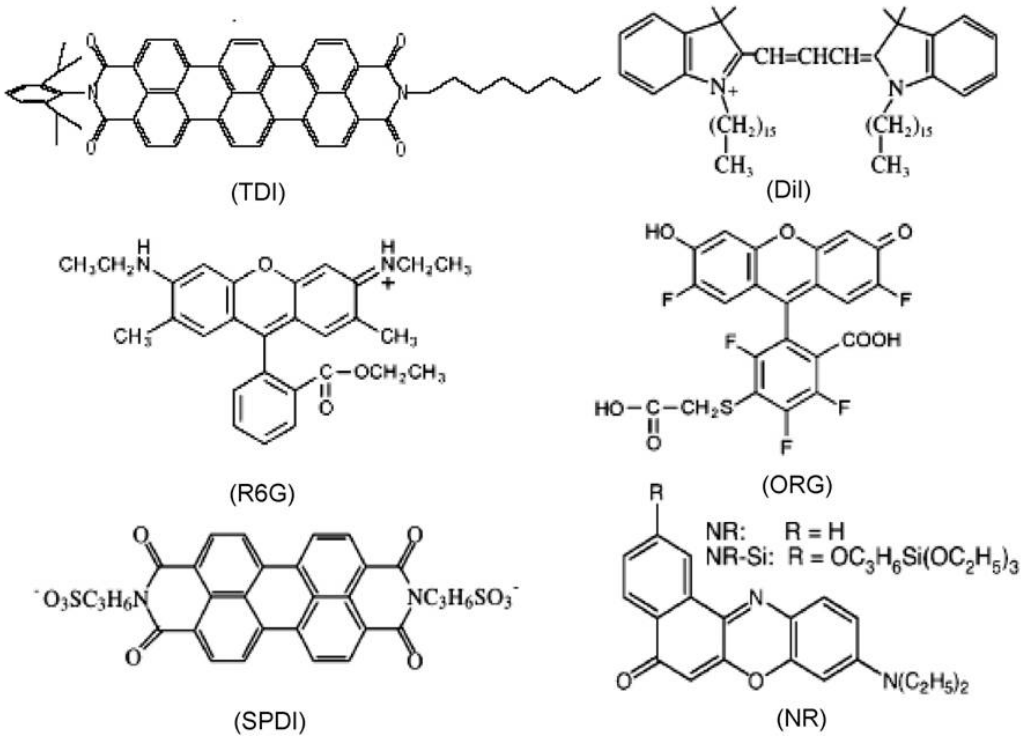


**Figure 1.1.** Chemical structures of dye molecules commonly used to probe silica materials.

### *1.3.2 Noncovalent Molecule-Matrix Interactions*

Interactions between dopant molecules and the silica matrix are of relevance to a number of potential applications, including those in chemical sensing, separations and catalysis.[1-8,68] Such interactions impede the diffusion of molecules through the matrix, slowing reaction rates and lengthening sensor response times. Generally, there are four possible types of noncovalent interactions that can occur between dopants and the silica matrix. These include ionic interactions, hydrogen bonding, hydrophobic interactions, and physical confinement (i.e. steric effects).[17,35] Ionic interactions readily occur between cationic species and anionic sites (i.e., deprotonated silanols, Si-O$^-$) on the silica surface, but they may also occur between dopants and other charged sites in ORMOSILs and surfactant-templated materials. Hydrogen bonding interactions can also occur between dopants and surface silanol (Si-OH) groups and similar functional groups in ORMOSILs.[35,69] Hydrophobic interactions occur between nonpolar surface

sites and nonpolar functional groups on dopant molecules and are of greatest importance in ORMOSILs and surfactant-containing mesoporous systems. Physical confinement becomes important when the pore size in a particular sample is similar to the size of the probe molecule. All of these forms of noncovalent interactions may lead to irreversible or periodic molecular adsorption or entrapment events or to partitioning of dopants into different sample regions.

A number of bulk spectroscopic methods have been employed to better understand molecule/matrix interactions in sol-gel materials. Included are electrochemical methods,[33]FTIR,[32] fluorescence spectroscopy[17,35,36] and anisotropy,[70,71] and NMR.[72-75] In many such studies, molecule/matrix interactions have been invoked to explain certain observations. For example, in electrochemical studies by the Collinson group,[33,76,77] they noted that the apparent diffusion coefficients of redox molecules entrapped in silica or ORMOSIL monoliths was strongly dependent on the charge and the presence of hydrogen-bonding groups on the probe molecule. They postulated that specific molecule/matrix interactions influenced molecular diffusion. However, such interactions could not be directly observed from the electrochemistry alone. Single molecule methods provide the ability to directly observe such interactions and distinguish their contributions from those of slow diffusion due to increased local viscosity. Importantly, single molecule studies are also well suited to characterization of thin films, which are often technologically more useful, especially in sensing applications.

#### *1.3.2.1. Ionic Interactions.*

Molecule-matrix interactions that are ionic in nature have been probed at the single molecule level by monitoring either the rotational or translational mobilities of fluorescent dyes. For example, the Yip group[66,78] has employed several different dye molecules carrying different charges (neutral, positive, negative) to probe such interactions in acid-catalyzed TEOS-derived

silica thin films. In one of their studies,[66] positively charge rhodamine 6G (R6G, Figure 1.1) and negatively charge oregon green 514 (ORG, Figure 1.1) were selected as molecular probes. These molecules were doped into silica films at nanomolar concentrations and the individual molecules were subsequently located by confocal fluorescence microscopy. The polarization of the fluorescence emitted by each molecule (specifically its emission dichroism) was then analyzed and used to assess the degree of rotational mobility exhibited by each molecule. Those that exhibited a time-invariant nonzero dichroism were classified as being rotationally immobile (i.e. "fixed"), while those that gave zero dichroism were concluded to be mobile (i.e. "tumbling"). Finally, those that showed distinguishable time-dependent changes in dichroism were classified as being of intermediate orientational mobility.

As reported, a 7-fold increase in the population of freely tumbling ORG molecules (14%), relative to R6G (2%) was found. The fewer tumbling R6G molecules were attributed to ionic interactions between the cationic dye and the anionic silica surface. The increased tumbling of anionic ORG was ascribed to repulsive interactions with the matrix. However, the relatively small populations of tumbling ORG and R6G molecules, and the relatively minor changes in mobility brought about by exposure of the matrix to water and pH 7 buffer, were taken as evidence that physical entrapment and hydrogen bonding also play major roles in governing mobility in this system.

Ionic interactions with the silica framework and entrapped surfactants have also been explored by monitoring the translational diffusion of single molecules. The Higgins and Collinson groups have recently used single molecule methods to probe such interactions in surfactant (cetyltrimethylammonium bromide, CTAB)-containing mesoporous films.[55,57] In one such study, cationic, anionic and neutral dyes were employed to probe molecular mobility under

both dry and hydrated film conditions.[57] Dye diffusion was initially explored by fluorescence imaging in a sample-scanning confocal microscope. The images obtained provided evidence of the relative strengths of molecule-matrix interactions in each case. Those that interacted strongly with the matrix yielded fixed, round fluorescent spots having Gaussian intensity profiles, while mobile molecules produced fluorescent streaks in the images.

Individual sample regions were subsequently positioned within the focal volume of the microscope and single-point fluorescence time transients recorded. Observation of constant fluorescence signals, followed by clear bleaching events were attributed to entrapment of molecules at fixed sites, due to strong molecule-matrix interactions.[57] In contrast, molecules that exhibited a high degree of mobility produced transients comprised of repeated fluorescence bursts, with little or no evidence of bleaching. However, even mobile molecules produced evidence of reversible molecule-matrix interactions via the occasional appearance of events in which the signal remained constant (and above background) for time periods too long to be explained by diffusion.[45,46] Such events were ascribed to reversible molecular adsorption, and are typically masked in bulk studies of molecular mobility.[46]

In these studies of CTAB-containing materials, an uncharged dye, Nile Red (NR, Figure 1.1), was observed to be mobile under all conditions, while an anionic dye, a sulfonated perylene diimide (SPDI, Figure 1.1), was found to be immobile.[57] The latter observation was attributed to strong ionic interactions between the dye and cationic surfactant. Evidence for strong interactions between the cationic dye 1,1'-dihexadecyl-3,3,3',3'-tetramethylindocarbocyanine perchlorate (DiI, Figure 1.1) and an anionic surfactant, sodium dodecyl sulfate (SDS), was also obtained. In contrast, SPDI and DiI were found to interact less strongly with SDS and CTAB,

respectively. These results clearly demonstrate the importance of ionic molecule-matrix interactions in these films.

#### *1.3.2.2 Hydrogen Bonding.*

Hydrogen bond formation between the matrix and dopant molecules is also reflected in the data described above from the Higgins and Collinson groups.[55] Such interactions are best depicted in the single point fluorescence time transients obtained from mesoporous materials doped with NR. The silica surface in these materials is expected to be covered with silanol groups, to which NR can hydrogen bond via its quinonal oxygen.[79] The appearance of bursts of constant fluorescence in the transients that were too long to be explained by diffusion alone were taken as strong evidence of reversible hydrogen bonding of NR to fixed matrix sites. Further analysis of the time transient data[45] provided a means to measure the distribution of adsorption times, as is discussed below.

#### *1.3.2.3 Hydrophobic Effects.*

To our knowledge, hydrophobic interactions have not yet been clearly linked to distinguishable surface adsorption events in single molecule studies of sol-gel systems, perhaps because of the very weak nature of these interactions. Hydrophobic effects have, however, been linked to partitioning and solubility-related phenomena in organically modified materials, leading to enhanced mobility of some dye molecules. For example, the relatively facile diffusion of NR through "dry" CTAB- and SDS-containing mesoporous silica films observed by the Higgins and Collinson groups was attributed to partitioning of the dye molecules into hydrophobic film regions.[55,57] The surfactants in these materials likely act as a solvent phase that facilitates NR mobility.

#### *1.3.2.4 Physical Confinement.*

Physical entrapment of molecules within the silica framework has been invoked in a number of papers to explain the conformational,[64] translational[55,57] and rotational[66,78] immobility of some dyes. Such explanations are reasonable for many sol-gel-derived films prepared in the absence of templating agents (i.e. surfactants). In these cases, the native "pores" present in the films may actually arise from "templating" of the surrounding matrix by the dye itself. Under these circumstances, the dye molecules may be permanently entrapped in such environments.

Some of the best demonstrations of the role played by physical confinement in governing molecular mobility come from work by the Bräuchle group.[56,80] In a recent report,[56] these researchers clearly showed that terrylenediimide (TDI, Figure 1.1) molecules found within CTAB-templated mesoporous materials assumed a well-defined orientation, with their long-axes aligned parallel to the long axis of the mesopores. Importantly, alignment was maintained in both dry materials, where the molecules appeared completely immobile, and solvent-loaded films, in which the molecules diffused primarily along one dimension (through the pores), while remaining in the aligned state. The dimensions of TDI were noted to be 1.1 nm X 2.5 nm and the pores 2-3 nm in diameter. It was also noted that the surfactant found within the pores may further restrict molecular motions, leading to the dramatic orientational confinement effects observed.

### *1.3.3 Molecular Mobility*

Bulk measurements of the translational and rotational mobility of molecules doped into sol-gel materials have been made by a variety of techniques, including electrochemical methods,[76,77,81,82] fluorescence anisotropy[70,71] and NMR.[72-75] The Collinson group, for example, has used electrochemical methods to measure the apparent diffusion coefficients, D, of redox

probes doped into sol-gel monoliths during the gelation, aging, and drying processes.[76,77,83] The molecules employed were of similar sizes but carried different charges. The magnitude of D in each case and the rate at which it changed during drying was clearly dependent on the charge of the redox probe and its size, relative to the silica pore size.[76,77,83] However, details such as the heterogeneity in D and the fraction of dopants interacting with the matrix could not be determined.

Electrochemical methods have also been used to study the behavior of redox molecules trapped in thin silica films.[84,85] However, it is much harder to measure D in thin films using electrochemistry because the redox current obtained depends on both D and the concentration of electroactive species. The research groups of DeArmond and Collinson showed that only a small fraction of the total concentration of a given redox probe is actually electroactive.[84,85] Hence, only rough estimates of D could be obtained. No specifics regarding reversible surface adsorption or physical confinement could be extracted from the data. Since single molecule methods frequently provide the means to distinguish between diffusion phenomena and molecule/matrix interactions (see above), they allow for more accurate measurements of diffusion coefficients, determination of relative populations of mobile and immobile species, and assessment of adsorption/desorption dynamics.

#### *1.3.3.1 Methods and Models.*

Translational diffusion has been explored at the single molecule level in silica materials by two different methods: fluorescence correlation spectroscopy (FCS)[86] and single molecule tracking (SMT).[87,88] These complementary techniques are now widely employed to probe molecular mobility under a variety of environmental conditions and for silica materials prepared by different methods.[55-57,89-91]

As applied here, FCS involves the recording of single-point fluorescence time transients using a confocal microscope. Such transients usually incorporate signal fluctuations that may have a number of origins. In cases where these fluctuations are caused by diffusion of single molecules into and out of the microscope detection volume, the results can be used to determine the molecular diffusion coefficient. For this purpose, the time transients obtained are first autocorrelated to find the distribution of time scales over which the signal fluctuates.[86]

The properly normalized autocorrelation function, $C(\tau)$, is calculated from time transient data as follows:

$$C(\tau) = \frac{\langle i(t)i(t+\tau)\rangle}{\langle i(t)\rangle^2} - 1 \qquad (1.1)$$

In Eqn. 1.1, $i(t)$ and $i(t+\tau)$ represent the fluorescence intensity at times t and $t+\tau$, respectively, while the brackets < > indicate the time-averaged value is taken.

To determine the relevant diffusion coefficient(s) and to distinguish between signal fluctuations involving molecular diffusion and adsorption/confinement, the autocorrelated data are subsequently fit to an appropriate model decay function. The choice of the model is made based upon careful inspection of the time transient data. The appearance of fluorescence bursts exhibiting constant fluorescence (aside from shot noise) for time periods too long to be explained by rare diffusive events are usually attributed to the reversible (or irreversible) adsorption of the dye to the sample surface. In cases where such events are not apparent, it is usually concluded that observed variations in burst lengths arise from multicomponent diffusion, due primarily to sample heterogeneity. Single point time transients can be easily recorded with 50-100 μsec time resolution, or they can be recorded on a single photon basis and subsequently binned.[49] Such high time resolution allows for diffusion coefficients to be measured even in bulk solution.

A variety of models have been used to explain results obtained from silica materials. For example, Dai and coworkers[61] used a two component diffusional model to fit their autocorrelation data in single molecule studies of R6G diffusion in a commercial mesoporous glass. Similarly, Martin et al. utilized this model to fit data obtained from NR molecules diffusing through ORMOSIL films.[92] In contrast, Fu and coworkers[55]and Ye, et al.[57] employed a model that includes both two-dimensional diffusion and reversible surface adsorption to fit data obtained from surfactant-containing and calcined mesoporous films.[43,45,46] The mathematical expression of this model is as follows:

$$C(\tau) = \frac{A_d}{1 + D\tau / s^2} + A_a \exp(-\tau k) \tag{1.2}$$

Here, D is the diffusion coefficient for the dye, $s^2$ defines the excitation area, k is the rate constant for desorption of adsorbed species and $A_d$ and $A_a$ are the amplitudes of the diffusion and adsorption components, respectively.

Single molecule tracking provides a more direct means for following single molecule diffusion.[88] In SMT, the sample is subjected to wide-field illumination by a laser source. The illuminated field of view is subsequently collected and imaged onto a charge-coupled device (CCD) detector, where a "movie" depicting sample emission in time is recorded. The single molecules in each image appear as diffraction-limited fluorescent spots that may move from frame to frame.[88] The fluorescent spots observed are fit to two-dimensional Gaussian profiles to precisely determine the molecular position in each frame. Under high signal-to-noise conditions, the molecular position can readily be determined to better than 10 nm.[89] The motion of the individual molecules is then reconstructed by determining the relative positions of each molecule in many successive frames.

SMT methods have the distinct advantage that the actual path (or trajectory) taken by a molecule can be recorded and long-term adsorption or entrapment events directly visualized. While SMT is a very powerful method in these respects, the results obtained are sometimes limited by the finite trajectory lengths that can be recorded, due to photobleaching. With currently available detectors, SMT studies are also limited to relatively slow diffusion, since data cannot be recorded with the same time resolution as single point time transients.

A common method to determine diffusion coefficients from SMT data is to plot the mean square displacement (MSD) of each molecule vs. time. According to the Einstein equation for single-component two-dimensional (2D) diffusion, this plot should exhibit a linear dependence on time:

$$\mathrm{MSD} = \langle r^2(t) \rangle = 4Dt \tag{1.3}$$

Here, r(t) is the displacement of the molecule from its initial location at time t, and D is its diffusion coefficient. The brackets < > indicate that an average is taken over all observed steps for a given t. Fitting of such data over an appropriate fraction of the total trajectory time (for which sufficient signal averaging occurs) has been used in a number of papers to determine D values.[87,93] However, McCain and Harris[90] have pointed out that D can be obtained to higher accuracy by instead calculating the distribution of r or $r^2$ per step.

#### *1.3.3.2 Measurement of Diffusion Coefficients.*

Hellriegel and coworkers have investigated the diffusion of single streptocyanine molecules in disordered macro/mesoporous sol-gel glasses.[80] In these studies, silica materials with pore sizes of 3 nm (M3) and 22 nm (M22) were prepared. They subsequently used SMT to follow the molecules as they migrated through these materials. As reported, the streptocyanine molecules in M22 yielded trajectories like those expected for simple Fickian diffusion over

distances as large as 5 μm, while those in M3 suggested the molecules were entrapped in fixed locations for significant periods of time. In M3, most of the dyes (80%) were concluded to be physically entrapped in regions ranging from 50-200 nm in size. Much less entrapment (20% of the molecules) was observed for M22, as would be expected for a physical (steric) entrapment mechanism. The results obtained indicate that the average streptocyanine molecule in M22 moves with a diffusion coefficient of $4.7 \times 10^{-9}$ $cm^2/s$ while that in M3 moves more slowly, with $D = 3.5 \times 10^{-10}$ $cm^2/s$. An ~ 5-fold spread in the diffusion coefficients obtained from different single molecules in both silicate materials was observed, indicative of the level of sample heterogeneity.

Single molecule diffusion in surfactant-templated mesoporous materials has been studied by the Higgins and Collinson groups[55,57] and by the Bräuchle group.[56,67] The former employed single point fluorescence time transients and FCS analysis to measure molecular diffusion coefficients. Both CTAB-containing and calcined thin films (with 770 nm and 400 nm thicknesses, respectively) were studied. Molecular mobility in these films was investigated under both dry and hydrated (20-50% relative humidity, RH) conditions. Three different dye molecules (NR, DiI and SPDI, Figure 1.1) were employed to probe the effects of molecule matrix interactions, as discussed above.

In the CTAB-containing films, anionic SPDI molecules were found to adsorb at fixed locations under all conditions, due to strong interactions with the cationic surfactant (see above). In stark contrast, neutral NR molecules exhibited facile diffusion under all conditions (20-50% RH), yielding an average D of $2.4 \times 10^{-10}$ $cm^2/s$ in dry (20% RH) films and a slightly larger D of $2.7 \times 10^{-10}$ $cm^2/s$ in hydrated (50% RH) films. NR mobility was attributed to its partitioning into the hydrophobic inner regions of the surfactant micelles. Among the three dyes employed, DiI

was found to be most sensitive to changes in film hydration, with average D values of $0.9 \times 10^{-10}$, $1.3 \times 10^{-10}$, and $3.0 \times 10^{-10}$ $cm^2/s$ obtained in films exposed to 30%, 40%, and 50% RH environments, respectively.

Single molecule diffusion studies also provide information on the relative importance of diffusion and reversible surface adsorption or physical entrapment in a given system. In the studies by the Higgins and Collinson groups[55,57] information on the relative contributions of adsorption and diffusive events to observed signal fluctuations was obtained from the relative amplitudes of these two components in fits of the autocorrelation decays to Eqn. 1.2. Fitting of these data also provides information on the amount of time the molecules spend adsorbed to the surface. In these studies, signal fluctuations from diffusing NR molecules were found to comprise only 43% of the autocorrelation decay amplitude under dry (20% RH) conditions and 58% in hydrated films (50% RH). Similarly, NR molecules were found to spend an average of 25 s in an adsorbed state in dry materials and about half as long under hydrated conditions. These observations indicate that water facilitates NR diffusion and desorption from the silica surface.

In calcined films, all three dyes were found to be immobile under dry conditions. Immobility in these samples was attributed to strong dye-matrix interactions that occur in the absence of solvent (water). In contrast, all three dyes were found to be mobile in films probed at 50% RH. The average diffusion coefficients were measured to be $4.0 \times 10^{-10}$, $3.1 \times 10^{-10}$, and $2.9 \times 10^{-10}$ $cm^2/s$, for SPDI, DiI, and NR, respectively. These results show SPDI is the most mobile of the three, likely because of repulsive interactions between the anionic dye and anionic silica surface, which may cause its exclusion from the smallest silica pores.

Dai and coworkers[61] used FCS to study three-dimensional diffusion of R6G in mesoporous glass with a pore size of 13 nm and negligible micropores. Three models describing single component diffusion, two component diffusion and diffusion coupled with adsorption were tested in fitting the autocorrelation data. In the correlation curve obtained at a distance of 10 μm into the mesoporous glass, three different models are used to fit the data. The single component model failed to fit the data properly, while the two-component models proved much better. Assuming two-component diffusion, the results obtained indicated that 38% of the molecules moved with $D_1=6.81\times10^{-7}$ $cm^2/s$ and 62% of the time they exhibited $D_2=4.84\times10^{-8}$ $cm^2/s$. It was concluded that the slower component may arise from multiple contacts between the molecules and the pore walls. Fitting with the diffusion/adsorption two-component model indicated that 80% of the molecules moved freely through the materials with $D=4.89\times10^{-7}$ $cm^2/s$, while the remainder reversibly adsorbed to the silica surface, exhibiting a mean desorption time of 67 ms. While both two-component models fit the data, it was concluded the latter was more plausible, due to the possibility for ionic interactions between positively charged R6G and the negatively charged silica surface.[61]

Some of the most dramatic results on single molecule diffusion in mesoporous silica have come from recent SMT studies by the Bräuchle group.[56,67,80,89,93,94] In one of their studies,[56]this group investigated the mobility of TDI molecules in CTAB-containing silica held under dry air and under a saturated chloroform atmosphere. The TDI molecules were found to be immobile under dry conditions and mobile when exposed to chloroform vapor. Most interestingly, the trajectories obtained conclusively demonstrated that the molecules migrated along one dimension (1D) within the mesopores (i.e., along the cylindrical channels). The 1D trajectories spanned distances of several micrometers, and the molecular long axis of each dye molecule was found to

orient parallel to the channel axis even while the molecules were moving. As noted above, the physical shape of TDI (1.1 nm X 2.5 nm) and steric interactions with the matrix likely prevented the molecules from freely rotating in the channels.

As reported, best fits to these data were obtained using a function that accounted for both 1D diffusion and adsorption. Furthermore, their MSD results were not perfectly linear in time, as would be expected for a random walk, but rather tended towards smaller values at longer times. The latter observation is good evidence for confined diffusion and was attributed to the presence of "dead ends" in the channels of these materials. The data show an average D value of $3.9 \times 10^{-12}$ $cm^2/s$, and the average molecule spent 18% of its time adsorbed to the silica surface. These plots also clearly depict the distribution in D and hence, the level of materials heterogeneity.

In another study by the Bräuchle group,[67] TDI diffusion in hexagonal, lamellar and mixed hexagonal/lamellar templated mesoporous films was investigated. These materials were prepared by controlling the amount of a longer-chain surfactant (Brij 56) used in sol preparation. In pure lamellar films, doughnut-shaped images of TDI emission in SMT images indicated that the molecules again assumed a constant orientation while moving laterally in two dimensions through the lamellar phase. In contrast, the results obtained from pure hexagonal films showed that the TDI molecules were rotating rapidly as they moved in down the mesoporous channels. In mixed films, both doughnut-shape and Gaussian fluorescence patterns appeared. The results obtained also showed that the lamellar and hexagonal channels were interconnected, as evidenced by time dependent changes in the fluorescence patterns obtained from each molecule and from alternation between 2D and 1D motions during single tracking periods. Other studies by this same group[94] employed both transmission electron microscopy (TEM)[95] and SMT to

prove the molecules were moving along the mesopore channels. It was concluded that there were five structural elements in two-dimensional hexagonal mesoporous films: straight segments, curved segments, domain boundaries, "disordered" regions and connective channels.

#### *1.3.3.3 Materials Heterogeneity.*

As described in previous bulk studies,[35,37,96] silica materials derived from the sol-gel process are expected to be very inhomogeneous. These inhomogeneities can lead to both spatial and temporal variations in molecular mobility, among other materials properties. Such phenomena have been studied at the single molecule level by both FCS and SMT methods.

For example, Harris and coworkers[97] have used total internal reflection fluorescence methods (TIR-FCS) to probe the diffusion of dye-labeled poly(amidoamine) (PAMAM) dendrimers in silica films prepared by the Stöber process.[98] PAMAM dendrimers were selected as probes due to their monodispersity and spherical structure, ensuring that dispersion observed in the data arose primarily from silica heterogeneity. The dependence of molecular diffusion on the size of the dendrimers (three generations were employed) in relation to the size of the pores was studied. The studies revealed that the large dendrimers were excluded from pores formed between small (27nm) particles, suggestive of a low number of pore defects. Smaller dendrimers were found to explore a wider range of pore structures, experiencing a greater level of pore tortuosity and reflecting the level of heterogeneity in pore size/shape in these materials.

Martin-Brown, et al.[92] have also used single molecule methods (primarily FCS) to study dye diffusion within ORMOSIL films. Commercial NR and a silanized NR derivative (NR-Si, Figure 1.1)[92] were used as probes in this study. ORMOSIL films were prepared from acid-catalyzed sols containing varying mole ratios of TEOS and isobutyltrimethoxysilane (BTMOS). Images and single point fluorescence time transients with FCS analysis provided evidence of

molecule mobility. In 33% BTMOS films, discrete, permanent photobleaching events were observed, consistent with immobile molecules. In contrast, transients recorded in 90% BTMOS films provided clear proof of translational diffusion for both dyes. This result was most surprising for the case of NR-Si, which was expected to covalently attach to the silica matrix.

FCS analysis procedures were applied to the time transients and the resulting autocorrelations fit to a 2D, two-component diffusion model.[92] Both molecules yielded fast and slow diffusion components. The fast components for NR and NR-Si yielded, on average, D = $1.2\times10^{-9}$ $cm^2/s$ and $2.9\times10^{-10}$ $cm^2/s$, respectively, with both slow components 100-fold smaller. The ~3-fold difference in the diffusion coefficients for NR and NR-Si indicated that the NR-Si molecules were indeed bound to a component of the silica matrix, but this component was comprised of liquid-like silica oligomers. It was concluded these were organically-modified silica oligomers that had phase separated from the inorganic components of the film. Imaging results[99] showed these components could be spatially resolved under certain circumstances.

### *1.3.4 Polarity Properties*

An in-depth understanding of the polarity properties of silica materials is required for many of their applications.[35] The polarity of the matrix plays a role in governing partitioning of molecules into and out of silica materials. It can also impact chemical reactions and charge transfer processes occurring within the matrix. Bulk fluorescence and absorption spectroscopies have long been used to probe the average polarity of silica materials,[17,35,37] with perhaps the most significant scientific questions arising in ORMOSILs.[35,37,96] For example, Brennan, et al.[100] have used 7-azaindole (7AI) and 6-propionyl-2-dimethylaminonaphthalene (PRODAN), both solvatochromic dyes, to examine ORMOSILs prepared from TEOS and a minority fraction of methyltriethoxysilane (MTES), propyltrimethoxysilane (PTMOS) or dimethyldimethoxysilane

(DMDMS). The results showed that internal materials polarity was dominated by the solvent composition from immediately after gelation until ~ 5-7 days later for MTES and DMDMS containing films. Afterwards, a point was reached in some of the materials where the polarity properties of the organic matrix component began to take over. Both blue shifts in the emission maxima and broadening of the spectra were observed. The latter was attributed to formation of at least two different classes of environments having distinct polarity properties, while the former could reflect partitioning of the dyes into regions of high organic content.

While the spectral linewidths obtained from bulk studies are reflective of sample heterogeneity, they only provide an average view of materials properties and are difficult to quantitatively interpret in terms of the actual distribution of environments present. Single molecule methods provide a means to investigate the polarity properties of individual nanometer-scale environments, thus allowing for the entire inhomogeneous distribution probed by a given dye to be mapped. Such methods also provide the means to characterize sample heterogeneity through a number of different statistical parameters: the mean, median, and most common environments can be determined, as can the width and skewness (if present) of the distribution. Finally, the populations and properties of rare environments can also be assessed.

The Higgins group has recently described single molecule methods that are useful for characterizing the polarity properties of organic polymers.[101] These same methods were also applied to ORMOSIL thin films.[79,99] In these studies, NR was loaded into the ORMOSILs at nanomolar concentrations and used to sense materials polarity. NR was selected because it is one of the most solvent-sensitive fluorescent dyes known.[102] Its solvent sensitivity arises from the large change in dipole moment associated with its lowest-energy electronic transition, which has been classified as an intramolecular charge-transfer transition.[103,104]

In these single molecule studies, fluorescence spectra were acquired, curve fit, and analyzed using a modified form of Marcus theory for charge-transfer transitions.[105-107] Of the range of available polarity models,[108,109] the charge-transfer model was selected because it allows for the most information to be derived from single-molecule data. Specifically, information on both the static and dynamic polarity properties of the materials can be obtained. These properties are reflected in the environment-dependent shift in the transition energy, $\Delta\Delta G°$, and the reorganization energy, $\lambda$, respectively, of the matrix (and solvent) dipoles surrounding each molecule.[101] Polar environments yield larger $\Delta\Delta G°$ values, whereas nonpolar regions give smaller values. Likewise, more dynamic environments yield relatively larger $\lambda$ values and rigid environments smaller values. The approximations and assumptions involved in this analysis are described in the original manuscripts.[79,99,101]

The ORMOSIL films studied[79,99] were derived from binary sol mixtures containing either 3-(triethoxysilyl)propionitrile (CNS) and TEOS or BTMOS and TEOS. Sols having different compositions (defined by the mole percent of organic precursor in the sol) were prepared, doped with NR, and spin cast as thin films on glass substrates. Sample-scanning fluorescence microscopy was then used to locate the individual molecules and to collect their fluorescence spectra.

Most of the distributions depicted could be classified as bimodal, multimodal or simply non-Gaussian, providing clear evidence for nonrandom variations in the film properties. The presence of the associated classes of environments was attributed in part to hydrogen bonding of some NR molecules to the matrix. However, the results were more generally attributable to (nonequilibrium) phase separation of organic- and inorganic-rich film domains, as had been previously proposed from bulk studies.[100,110,111] Phase separation could have resulted from

differences in the hydrolysis and condensation rates of the precursors[112]or from the mutual immiscibility of the precursors. As with all dye-based polarity studies, preferential partitioning of the dye into certain environments could have biased the observed distributions, as addressed by Bardo, et al.[79] Nevertheless, these distributions prove that in some cases the "average" environments reflected in bulk spectroscopic results may not adequately reflect the actual materials properties.

The inhomogeneous distributions observed also allow for more detailed classification of the sample environments. For example, it can be concluded that the most common environments probed were significantly more polar and less dynamic than the average environments. This observation may indicate that the aforementioned phase separation may only occur in rare circumstances, leading to the observed tails to lower and higher values of $\Delta\Delta G°$ and $\lambda$, respectively. It is also of interest that the static and dynamic polarity properties for BTMOS-containing films change abruptly at about 50% BTMOS, while the properties of CNS-containing samples change gradually. The incorporation of liquid-like oligomers in films of high BTMOS content is the likely cause,[92] suggesting the properties of the BTMOS films may be closer to their equilibrium values than in films of lower organic content, where the properties may be kinetically controlled.

### *1.3.5 Matrix Acidity*

The hydrogen bonding and ionic molecule-matrix interactions discussed above arise from the presence of protonated and deprotonated silanol species in the silica materials.[113] These silanols are weakly acidic and the extent to which they are protonated or deprotonated depends upon their individual $pK_a$s and on the pH of the environment in which each is found. The $pK_a$ of silanol groups on silica surfaces is known to vary between ~ 4.5 and 9.[113,114] Silanol $pK_a$s in

silica films will vary with the density of silanol groups present and the organic content of the environment (e.g. in ORMOSILs or due to solvent).

The acidity properties of the silanols found in/on sol-gel-derived materials have been studied by several bulk methods, including temperature-programmed desorption (TPD),[50,115] FTIR,[32,116] Raman[69] and NMR spectroscopies.[50,115] Though these studies have provided valuable information on the average acidity of the relevant surface sites, they provide little information on the level of heterogeneity present. Sample heterogeneity is known to be important in several applications of sol-gel-derived materials, including in the response of silica-based pH sensors. Representative bulk work in this area is taken from the Saavedra group, in which sol-gel methods were used to deposit thin silica films as waveguiding and indicator layers in pH sensing devices.[117] In this study, it was found that the pH indicator dye responded over an unexpectedly broad range of pH values. It was concluded that the sensing dye was entrapped in "chemically inequivalent microenvironments" that caused the dye to respond differently in each.[117] In the same study, hysteresis in the sensor data was attributed to the presence of indicator molecules that responded slowly to pH changes.

Single molecule methods have the potential to provide valuable new insight into the origins of such observations. As with all single molecule studies, the initial selection of an appropriate pH-sensitive fluorescent dye is required. The dye selected should be highly fluorescent and exhibit clear pH-dependent changes in its emission and/or excitation spectra, but little or no change in emission yield. It should also have a $pK_a$ similar to that of the species to be probed. C.SNARF-1, which has a $pK_a$ of 7.5, is a nearly ideal probe for studying the effects of silanol site properties and was employed by Fu, et al. in recent studies of silica film acidity.[118] A slightly different form of this dye was used in earlier single molecule studies of agarose gels.[119]

The protonated form of C.SNARF-1 emits in a band centered at 580nm, while the deprotonated form emits near 640nm. The ratio of single molecule emission in these two bands ($R=I_{580}/I_{640}$) can be used as a probe of the pH of the local environment surrounding each molecule.

In the studies by Fu, et al., the local acidity properties of films prepared via the acid-catalyzed hydrolysis and condensation of TEOS were investigated.[118] It was concluded the local environments in "as-prepared" films had an average pH of ~4.8. The range of R values obtained was consistent with a 1-2 pH unit variation in the local acidity. Variations in the concentration of residual acid catalyst and in the local silanol $pK_a$s were the likely cause of these pH variations.

The extent to which local film acidity could be altered/controlled by exposure to external solutions of known pH was also explored. In these studies, the silica films were treated by immersion in various pH solutions for different lengths of time (1 h and 8 h). Histograms of the R values obtained are shown in the original paper. Each distribution appears to be Gaussian in shape and monomodal, as evidenced by the fits appended to each data set. This observation suggests that variations in the acidity properties are random. Hence, the mean acidity properties could have been accurately determined by bulk spectroscopic methods. However, such a conclusion could not have been drawn without first recording these data.

The mean acidity values obtained by fitting the R distributions provide an initial view of film acidity properties. These data are plotted vs. treatment pH and fit to a Henderson-Hasselbalch expression as a means to characterize the apparent pH dependent response in each series of experiments.[120] As depicted in the original paper, the R values showed the same qualitative trend to smaller values with increasing treatment pH, as observed in bulk solution phase experiments. However, the trend was much more gradual in the films treated for only 1 h, and was most similar to bulk solution results for films treated for 8 h, exhibiting a sharp

transition around the $pK_a$ of the dye. Importantly, the R values obtained at high pH in the 1 h treated films were significantly larger than in the 8 h treated samples, indicating that some molecules remained protonated even after treatment in high-pH solutions for 1 h. This observation indicated that some environments were inaccessible on this time scale, a conclusion that is consistent with those from bulk studies,[121,122] and which is also reflective of sample heterogeneity.

The widths of the R distributions provide the best view of heterogeneity in terms of film acidity properties. The results obtained by Fu and coworkers[118] demonstrated that film heterogeneity (reflected by the $2\sigma$ values obtained) was strongly dependent on treatment time, as reflected in the uniformly narrower distributions obtained from films treated for 8 h, relative to those obtained after only 1 h. These differences were again attributed to kinetic limits to changes in the local pH, due to entrapment of some molecules in tightly constrained pores within the film.

The distribution widths ($2\sigma$) also provide a means for probing the influence of the surface silanols on the local pH. As shown in the paper, the distributions obtained after treatment at pH 8 and 9 were the most narrow (near the noise-limited width), whereas those obtained after treatment at pH 7 were broadest. At pH 7, the average pH is close to the $pK_a$ of the dye, where it is most sensitive to changes in local acidity.[119] The distribution widths at pH < 7 and pH > 9 were therefore concluded to reflect significant heterogeneity in the film acidity properties, likely resulting from the presence of residual acid and silanol $pK_a$ variations. In contrast, the much narrower distributions observed at pH 8 and 9 indicated the local environments were very homogeneous in this pH range. Enhanced materials homogeneity was attributed to buffering of the local pH by the majority surface silanols, which likely have $pK_a$ values of 8.5-9.[113,114]

## 1.4. Single Nanoparticle Studies

A significant limitation of the single molecule experiments described above is the short lifetime of the dyes employed. Under ambient conditions, such dye molecules usually photobleach after only a few seconds of continuous illumination,[123] limiting the number of spectroscopic measurements that can be made, and the precision of the results obtained. One possible route to improved measurements would be to instead employ strongly luminescent or scattering metal[124-127] or inorganic nanoparticles,[128] or luminescent organic polymer nanoparticles.[129] Nanoparticles that are sensitive to and report on their chemical environment are now being developed.[130]

Gold nanoparticles have been employed previously as probes of sol-gel-derived silica materials. For example, Akbarian, et al. have demonstrated the photochemical production and optimization of gold nanoparticles in a silica matrix for surface enhanced Raman scattering (SERS) experiments.[124] They used their silica-based SERS substrates to detect pyrazine molecules diffusing into the matrix. Such measurements could also readily be performed at the single particle level[125,127,131] to obtain information on materials heterogeneity.

The intrinsic light scattering properties of silica nanoparticles can also be used to probe matrix properties. For example, in bulk studies, Nakanishi et al. have employed scattering methods to follow the sol-gel process in pore-forming materials[132] prepared by polymerization-induced phase separation methods.[48,133,134] The macroporous sol–gel-derived monoliths obtained are an intriguing class of materials that have attracted considerable attention owing to their unique structural features and potential applications in catalysis, separations, superhydrophobic materials, drug delivery, chemical sensors, and optics.[53,133-135]

Dong, et al.[136] have recently used in situ microscopic methods and confocal correlation spectroscopy (CCS)[137] to follow the formation of thin macroporous monoliths of MTMOS-

derived materials from before phase separation to well after gelation at the single-pore/single-nanoparticle level. The acid catalyzed sol-gel process employed led to formation of silica nanoparticles very early after sol preparation. These nanoparticles were found to efficiently scatter light in a confocal microscope, providing an intrinsic probe of the sol-gel process and the growth and aggregation of the individual silica nanoparticles. Confocal images of the evolving materials allowed for direct observation of phase separation in the sol, forming two distinct phases, one high in silica polymer/nanoparticle concentration (i.e., regions exhibiting relatively strong light scattering, the matrix) and one of low silica content (regions exhibiting relatively weak scattering, the pores). The time evolution in the size, shape, and position of these domains was followed by optical microscopy, through gelation.

Single point time transients recorded in various regions of interest (i.e. within individual pores and in the matrix) were recorded and used to follow the silica nanoparticle growth and aggregation processes. Autocorrelation data obtained were fit to a two-component diffusion model and used to determine the nanoparticle diffusion coefficients. Prior to phase separation, all of the data could be fit to a single diffusional component, consistent with a monomodal, random distribution of MSQ particle sizes. After phase separation, many of the autocorrelation data showed clear evidence for a bimodal distribution of particles, reflecting the presence of some small particles having relatively large diffusion coefficients, while the majority of particles were larger, yielding smaller D values. The details will be presented at Chapter 5.

## 1.5. Silica Thin Film with Polarity Gradient.

Silica film polarity gradients may provide the means to control environmental polarity, regulate surface adhesion, drive mass transport, etc. for a range of diverse applications in separations, sensing and catalysis. As to our knowledge, silica film polarity gradients have not

yet been reported. We recently developed a method called “infusion-withdrawal dip-coating” to prepare a sol-gel derived polarity gradients. Bulk fluorescence spectra (Nile Red) were acquired as a function of position along each gradient. These data provide strong evidence for the presence of polarity gradients in these films. Water contact angle data acquired along the gradients provide valuable supporting evidence, depicting a monotonic increase in contact angle along the gradient direction. FTIR microscopy results demonstrate that the methyl content of the films increases from top to bottom. In near future, single molecule study will be performed to investigate the nanoscale characteristics of the gradients. The details on how to prepare and characterize the gradient will be introduced in Chapter 6.

## 1.6. Conclusions and Future Directions

The aim of this part of thesis is to review some of the recent single molecule studies of sol-gel derived silica materials. Single molecule methods for probing molecule/matrix interactions in dye-doped silica materials have been described. Studies of dopant mobility within silica materials using FCS and SMT methods have also been covered and the relevance of the results, especially with respect to the quantitative measurement of diffusion coefficients in the presence of host-guest interactions, have been highlighted. Likewise, recent single molecule studies of sol-gel matrix polarity and acidity properties have been reviewed. The ability of all such studies to provide detailed and valuable new information on materials heterogeneity was demonstrated.

The studies described above, along with other studies not described in this chapter prove that single molecule methods represent an invaluable set of tools for the study of silica materials. They have already provided a better understanding of the nanoscale properties of these technologically useful and fundamentally interested materials and will continue to do so for the foreseeable future. However, improvements to the methods presently employed are still required to fully understand silica materials. For example, dyes that better probe a single class of materials properties, without yielding data perturbed by other effects are required. Likewise, dye molecules that are more photostable are also required so that more spectroscopic information can be derived from them at higher signal-to-noise ratios. Luminescent or strongly-scattering nanoparticles may serve as substitutes for dyes in the future,[124,126,130] assuming such particles can be tailored to exhibit sensitivities to specific materials parameters, as can already be achieved using fluorescent dyes.

# CHAPTER 2 - Experimental Section

## 2.1 Sample Preparation

### *2.1.1 Preparation of Mesoporous Silica Thin Film*

#### *2.1.1.1 As-synthesized Film*

Silica sols were prepared by mixing tetramethoxysilane (TMOS, 0.5ml), water (0.24ml), absolute ethanol (1.57ml) and HCl (0.10 ml of 0.1 M HCl) in a small vial. The sol was stirred for 1 h after addition of the above components and was then allowed to sit for an additional 24 h at room temperature. Cetyltrimethylammonium bromide (CTAB, Aldrich) or sodium dodecyl sulfate (SDS, Aldrich) was then dissolved in the solution by vigorous stirring for 1 h. The final molar ratio for the silicate composites was typically 1:5.6:8:0.003:0.2 for TMOS:$H_2O$:Ethanol:HCl:CTAB and 1:16.8:8:0.003:0.05 for TMOS:$H_2O$:Ethanol:HCl:SDS. For the preparation of dye-doped mesoporous films, either a methanolic solution of Nile Red (NR, Aldrich), a methanolic solution of 1,1'-dihexadecyl-3,3,3',3'-tetramethylindocarbocyanine perchlorate (DiI, Invitrogen) or an aqueous solution of homemade N,N'-bis(3-sulfonatopropyl)perylene-3,4,9,10-tetracarboxylic diimide (sulfonated perylene diimide, SPDI, see the preparation below) was added to a portion of the above sol to yield a total dye concentration of 0.5 nM. Immediately after addition of the dye, ≈ 65 μL of the sol was spin cast (30s at 6000 RPM) onto a clean glass coverslip (Fisher Premium). These films are transparent with film thickness of 770±60 nm by profilometry (XP-2 Ambios Technology; Santa Cruz, CA) in Dr Culbertson's lab. The films were dried overnight at room temperature in a desiccator in the dark prior to use. Films studied without further treatment are referred to as "as-synthesized" films. Small angle X-ray diffraction (XRD) data from the CTAB-containing films indicate they

incorporate hexagonally-organized mesopores of 35 Å periodicity (d-spacing), with the pores running parallel to the film plane. XRD data from SDS-containing films show they incorporate lamellar structures of 37 Å periodicity (see Chapter 3).

Two different types of as-synthesized films were studied by single molecule methods. Dry as-synthesized films were maintained in a dry environment (dry air, 20% RH) throughout the recording of images and time transients. Rehydrated as-synthesized films (i.e. incorporating water within the mesopores) were stored in a humid environment (humidified air, i.e. 30, 40 or 50% RH) for approximately 12 h prior to use. They were maintained under the same humid atmosphere throughout data collection. The rehydration setup is shown in Figure 2.1

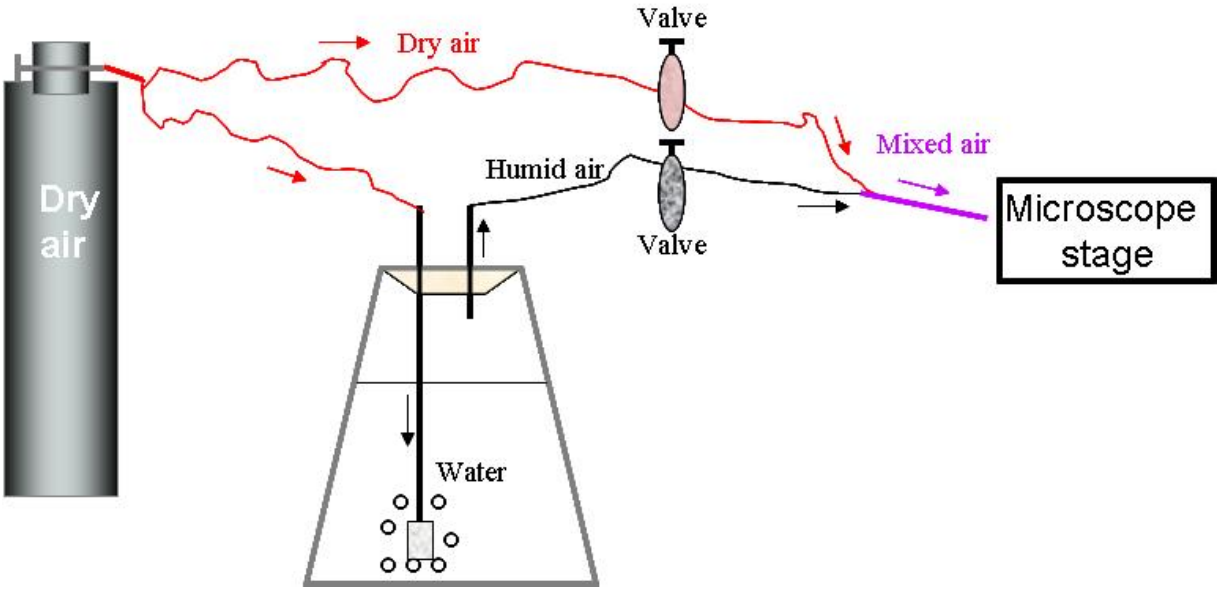


**Figure 2.1.** Rehydration setup.

### *2.1.1.2 Calcined Film*

Surfactant-free mesoporous silica films were obtained using a similar procedure described above, followed by calcination of the films in a furnace (1500 Barnstead/Thermolyne). In this process, the films were first heated at 160 ˚C for 90 min. The temperature was then slowly increased (1 ˚C/min) to 350 ˚C, where it was held for 5 h. Figure 2.2 shows this

calcination process. The calcined films were subsequently treated in an air plasma (Harrick Plasma) for 2-3 min to remove residual luminescent impurities that otherwise yielded significant background in the single molecule experiments. The calcined, plasma treated films were then reloaded with dye by soaking them in 2 nM methanolic solutions of Nile Red for 1 h, followed by rinsing with ethanol to remove loosely bound dye. These films were also dried in a desiccator overnight before use. The resultant films were referred to as "calcined" films. It should be noted that the calcined film for SDS-contented silica film collapsed completely under calcination and did not show any structure periodicity. Therefore, we focused on the calcined CTAB-contented film, which was 400±30 nm thick and the mesopores have collapsed and disordered somewhat, exhibiting 24 Å periodicity (see Chapter 3).

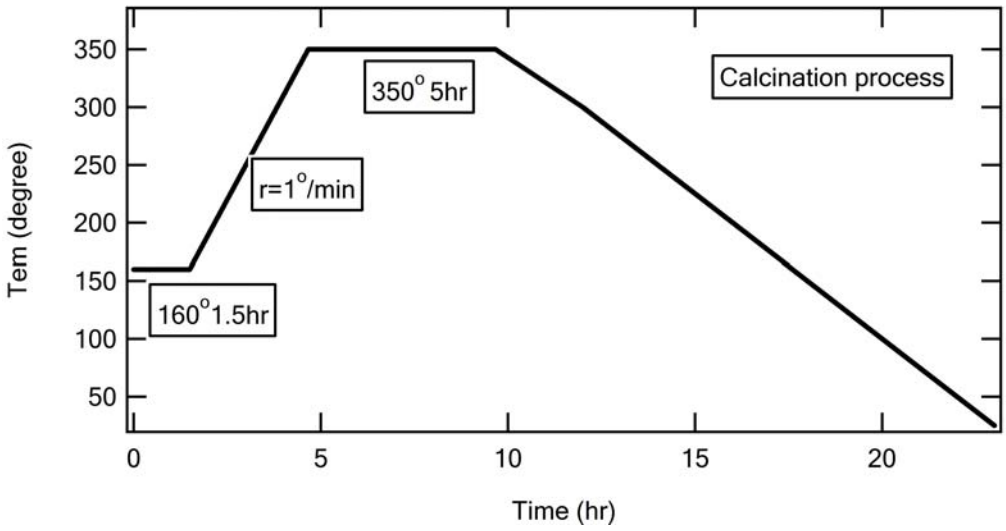


**Figure 2.2.** Calcination process in the preparation of calcined MCM film.

Similar to the as-synthesized films, two different types of calcined-reloaded samples were studied by single molecule methods. Dry calcined films were maintained in a dry environment (dry air, 20% RH) throughout the recording of images and time transients. Rehydrated calcined films (i.e. incorporating water within the mesopores) were stored in a humid environment

(humidified air, 50% RH) for approximately 12 h prior to use. They were maintained under the same humid atmosphere throughout data collection.

Both dry and rehydrated as-synthesized and calcined films were used in Chapter 3 and Chapter 4.

#### *2.1.1.3 Synthesis of SPDI*

The fluorescent dye, SPDI, was prepared by Corey Weitzel, using the following procedure. To 140 mL pyridine in a 250 mL round bottom flask was added 220 mg perylene 3,4,9,10-tetracarboxylic dianhydride, 162 mg zinc acetate and 234 mg 3-aminopropane sulfonic acid, yielding a molar ratio of 1:1:3 for perylene dianhydride, zinc acetate, and aminopropane sulfonic acid. The reaction mixture was refluxed under nitrogen for 7 days. The solid product was then collected by vacuum filtration and rinsed with 3:1 (by volume) ethyl acetate/hexane. The crude solid was dried in a vacuum oven at 80$^{o}$C for 8 h. The product was purified by first dissolving it in slightly basic water and removing the insoluble solids by centrifugation. The product was then precipitated from solution by pouring it into an equivalent volume of 2 M HCl, followed by cooling in an ice bath for 1 h. The final product was collected by centrifugation, with the dark red solid being transferred to a fritted filter and rinsed with cold 1:1 (by volume) isopropanol/ether. Finally, the purified solid was dried in a vacuum oven for 12 h at 80$^{o}$C. Ethanol solutions of the final product were strongly fluorescent and yielded absorption and emission spectra peaked at 525 nm and 565 nm, respectively.

### *2.1.2 Preparation of MSQ Films*

#### *2.1.2.1 Bulk MSQ Samples*

All chemicals employed, including methyltrimethoxysilane (MTMOS, >98%), nitric acid ($HNO_3$), water (HPLC grade) and methanol (MeOH, HPLC grade) were obtained from Aldrich

and were used as received. Bulk samples were prepared as below. 0.50 mL of MTMOS and 0.14 mL of MeOH were first mixed in a small vial (O.D. X H: 12 X 35mm). After 5 min, 0.13 mL of 1M $HNO_3$ was quickly added. The mixture was then vigorously agitated for 1 min at room temperature. The reaction was really fast and gave off a lot of heat, as evidenced by the glass vial becoming really hot to the touch. The final mole ratios of Si:$H_2O$:MeOH were 1:2:1.

#### *2.1.2.2 MSQ Films*

Preparation of MSQ films was performed 20 min after preparation of the sol as described in the bulk MSQ samples section. In this procedure, a 1.5 μL aliquot of the sol was dropped onto the center of a microscope cover slide. These cover slides had been cleaned by vacuum plasma before use. The slide was then quickly covered with a second cover glass to spread the sol and to prevent its evaporation. The sol in between the two cover glasses is readily visible since its color had changed slightly from colorless to a little dark. The sample was discarded if there were air bubbles confined between these two slides. The films obtained were determined to be 2-5 μm thick by optical microscopy (see Chapter 5).

### *2.1.3 Preparation of Silica Thin Film with Polarity Gradients*

Glass coverslips (Fisher Premium) and silicon wafers (Silicon Inc.) were both employed as substrates. Prior to use, all substrates were first cleaned in fresh Piranha solution (Caution, Piranha solutions are extremely dangerous); they were subsequently cleaned a second time in an air plasma. This two-step process ensured rigorous removal of all organic contaminants.

#### *2.1.3.1 TMOS-coated Sublayer*

The clean substrates were subsequently coated with a sol-gel-derived silica "sublayer" to aid in adhesion of the gradient materials. Tetramethoxysilane (99%, TMOS, Fisher) was used as the silica precursor. Sols were prepared in a 1:11.5:5.1:0.006 (TMOS:$H_2O$:Ethanol:HCl) mole

ratio and were allowed to age for one day, prior to use. Sublayers were produced by spin-coating the sol onto the substrate (100 μL, 30 s at 6000 rpm). The resulting sublayer was uniform and had a thickness of ~180 nm, as determined by both profilometry and ellipsometry. All sublayer-coated substrates were dried in a dessicator for one day, prior to further use.

#### *2.1.3.2 Bulk Spin-cast Films*

TMOS bulk spin-cast films were prepared by spin casting a TMOS sol prepared in a 1:80:5.3:0.095 (TMOS:Ethanol:$H_2O$:$NH_4OH$) mole ratio and subsequently aged for 6 h onto a cover glass. MTMOS bulk spin-cast films were obtained by spin casting a MTMOS sol prepared in a 1:10:4:0.072 (MTMOS:Ethanol:$H_2O$:$NH_4OH$) mole ratio and subsequently aged for 6 h onto a cover glass.

#### *2.1.3.3 Spin-cast Films on TMOS-coated Sublayer*

Silica films having uniform composition and polarity properties were also prepared and were used to verifying the interpretations of data obtained from the gradients. For this purpose, TMOS (TMOS:$H_2O$:Ethanol:$NH_4OH$=1:80:5.3:0.095) and MTMOS (MTMOS:Ethanol:$H_2O$:$NH_4OH$ =1:10:4:0.072) sols were prepared as described above and aged for 6 h. Sols containing different molar fractions of TMOS and MTMOS were then obtained by mixing appropriate amounts of each of these sols. Mixed sols containing 0%, 20%, 40%, 60%, 80% and 100% MTMOS (relative to total silica content) were prepared and vigorously mixed for 20 min. These sol mixtures were then spin cast onto both clean and sublayer-coated substrates. All such films were dried in a dessicator at room temperature for 2 days prior to use.

#### *2.1.3.4 Gradient Film*

Production of silica film polarity gradients employed time-varying mixtures of two different sols. The first was a TMOS sol prepared in a 1:80:5.3:0.095

(TMOS:Ethanol:$H_2O$:$NH_4OH$) molar ratio and subsequently aged for 6 h. The second was any one of three different sols prepared using methyltrimethoxysilane (97%, MTMOS, Fisher). These latter sols were prepared using different volumes of ethanol to dilute the sol. Sols were prepared in 1:10:4:0.072, 1:20:8:0.072 and 1:40:13:0.072 (MTMOS:Ethanol:$H_2O$:$NH_4OH$) molar ratios. These sols are designated throughout Chapter 6 as 1:10, 1:20, and 1:40 MTMOS sols. Table 2.1 shows the recipes for all the sols.

| Component (mL) | TMOS/ MTMOS | EtOH | 0.1M HCl | 1.0M $NH_4OH$ | $H_2O$ | Aging time (hr) |
|---|---|---|---|---|---|---|
| TMOS (sublayer) | 0.8 | 1.6 | 0.32 | N/A | 0.8 | 24 |
| TMOS | 0.28 | 9.0 | N/A | 0.18 | 0.18 | 6 |
| MTMOS (1:10) | 2.0 | 7.0 | N/A | 1.0 | 1.0 | 6 |
| MTMOS (1:20) | 1.05 | 8.0 | N/A | 0.5 | 1.0 | 6 |
| MTMOS (1:40) | 0.6 | 9.0 | N/A | 0.29 | 1.0 | 6 |

**Table 2.1.** Recipes for different TMOS and MTMOS sols

Gradient films were deposited on the sublayer-coated substrates in a custom built glass reservoir designed to simultaneously minimize sol volume, decrease sol evaporation and allow for stirring to homogenize the sol mixture. A diagram of the apparatus and a photograph of the reservoir are shown in Figure 2.3. The glass reservoir includes a rectangular upper region having dimensions of 3.5cm × 0.5cm × 3.0cm (L × W × H) that was designed to admit one inch substrates. The lower portion of the reservoir was comprised of a small cylindrical vial (D=1cm, H=1cm) that facilitated stirring of the sol mixture. Two small glass tubes were installed at fixed locations inside the reservoir for infusion and withdrawal of the sols. All depositions were

performed with the reservoir mounted atop a pneumatic vibration isolation table, with the reservoir housed in a closed Plexiglas box.

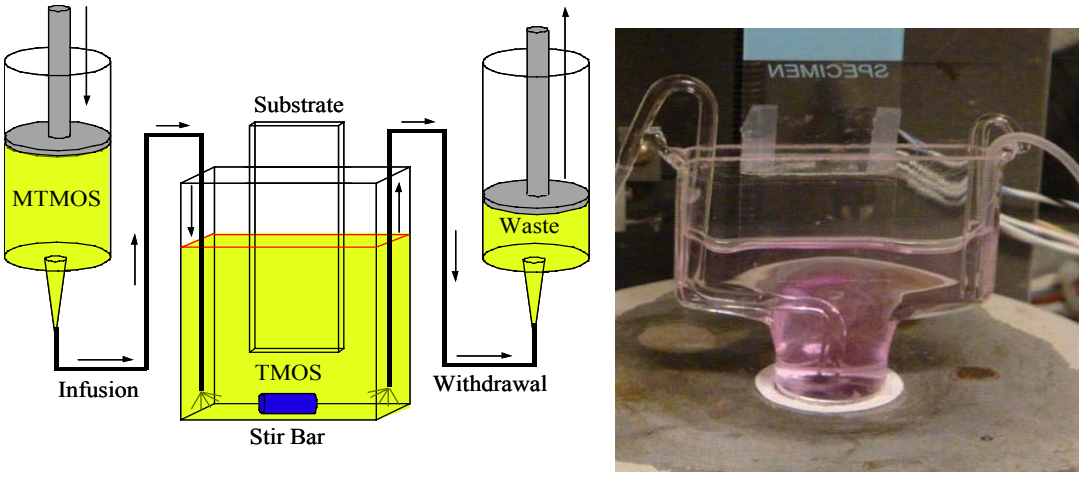


**Figure 2.3.** Diagram of "infusion-withdrawal" dip-coating method used to prepare silica film gradients (left) and photograph of the apparatus (right). Synchronized syringe pumps are used to 1) infuse an MTMOS sol into the TMOS-filled deposition reservoir and 2) withdraw the resulting mixed sol from the reservoir. The withdrawal rate is set faster than infusion so that the sol slowly recedes down the face of the substrate.

Deposition of silica film polarity gradients was accomplished as follows. A sublayer-coated substrate was first suspended in the middle of the reservoir. The initial TMOS sol (see above) was transferred into the reservoir, submersing all but the top 1-2 mm of the substrate. The MTMOS sol (see above) selected for a given deposition was then loaded into a syringe and mounted in a syringe pump (NE-1000, New Era Pump Systems, Inc.). The syringe was attached to the reservoir via flexible plastic tubing. Gradient deposition proceeded by slowly infusing the MTMOS sol into the reservoir. The mixed sol contained in the reservoir was simultaneously withdrawn using a second, synchronized syringe pump also attached to the reservoir through flexible plastic tubing. The infusion pump was set to deliver MTMOS sol at a rate of 10.0 mL/h, while the other was set to withdraw 14.2 mL/h of mixed sol. The sol within the reservoir was

carefully stirred at a constant rate, using a magnetic stir bar throughout this process. Prior to the start of deposition, it was verified that sol stirring produced no detectable movement of the sol surface. The difference in infusion and withdrawal rates led to a steady decrease in the height (~ 0.3 mm/min) of the sol in the reservoir, with an overall change of ~ 1.8 cm. The entire "infusion-withdrawal dip-coating" process lasted for ~ 1 h. After deposition, residual sol clinging to the bottom of the substrate was gently removed using a Kimwipe. The final gradient films were dried in a dessicator for 2 days.

Preparation of dye-doped silica gradients was performed only on glass coverslips and proceeded exactly as described above, except that both sols incorporated Nile Red (NR) at ~ 1 μM concentration. In some cases, gradients were simultaneously prepared on two coverslips, using the same sol mixture. In this case, the two substrates were assembled back-to-back with a thin film of glycerin between them. The thin layer of glycerin prevented silica deposition on the backside of the substrates. Without the glycerin layer, inadvertent coating of the substrate backside was found to interfere with the determination of polarity properties from the Nile Red emission.

## 2.2 Instrumentation

### *2.2.1 Single Molecule Setup*

All single-molecule studies were conducted on a sample scanning confocal microscope, Figure 2.4. Briefly, this system is built on an inverted epi-illumination microscope (Nikon TE-200). Light from either a green helium-neon laser (543.5 nm, used for NR and DiI) or from an argon ion laser (514 nm, used for SPDI) was reflected from an appropriate dichroic beamsplitter into the back aperture of an oil immersion objective (Nikon Plan Fluor, 1.3 numerical aperture, 100X magnification). This objective was used both for illuminating the sample, yielding a

nearly diffraction limited focus of ≈ 300 nm $1/e^2$ radius, and for collecting the resulting single molecule fluorescence. The incident laser power was always maintained in the 200-400 nW range (estimated from measurements made external to the microscope). An electronic shutter was used to control illumination of the sample. Fluorescence collected from the sample was isolated from the excitation light by passage back through the dichroic beamsplitter, an appropriate holographic notch filter, and a bandpass filter. A single-photon-counting avalanche photodiode was used as the detector.

In this paragraph, I will go through the detailed description of several important components in a confocal microscope. The first is the microscope objective, which is the most important part of the microscope. The objective is used for focusing of the incident laser beam onto the sample. The numerical aperture (NA) of an objective is a measure of its light focusing/gathering power, and is defined as: $NA = n\sin\theta$. Here, n represents the refractive index of the medium between sample and lens and $\theta$ is half the angle subtended by the lens at its focus. Since the objective is used for both sample illumination and signal collection, the quality of the confocal setup is often determined by the quality of the objective used. In my setup, a 100X oil immersion objective (Nikon Plan Fluor) with an NA of 1.3 was used. The second component is a dichroic mirror, which is used to reflect short wavelength light and let longer wavelengths pass. It helps to eliminate residual excitation light (laser) and allows the collection and excitation processes to be accomplished through the same objective. A fixed angle is usually employed for the placement of the mirror to obtain the optimal reflective and transmissive properties. The third one is the scanning stage, which has two types, sample scanning and laser scanning. A piezo-electric sample scanning stage (Queensgate) was used in my setup, which had a position accuracy of ~3nm in X and Y directions. The maxima position (X and Y) range is from -40 μm to +40 μm.

The fourth one is the detector. Generally, there are three single molecule detectors, Charged Coupled Device (CCD), Avalanche Photo Diode (APD) and Photo Multiplier Tube (PMT). The former two (CCD and APD) were used in my setup. The CCD (Roper Scientific) was used for the collection of single molecule emission spectra, while the APD (EG&G) was employed during acquisition of fluorescence images and single point time transients. The fifth one is the pinhole. The pinhole is an important component which is used to minimize the detection volume and to increase the signal-noise-ratio (SNR) by blocking the out-of-focus signal from the sample. Usually, it has a diameter of 10 to 100 μm and in practice, this size should be set as close as possible to the full width at half maximum (FWHM) of the Airy diffraction pattern generated by the lens at the pinhole's position. In the single molecule experiments in this thesis, the pinhole was not applied and the obtained image and time transient without a pinhole has high enough SNR because most the samples were very thin (several hundreds nm) and the APD was sufficiently small (170 μm). As a result, the difficult pinhole alignment process can be skipped and lots of time was saved. The last important component addressed is the excitation source, a laser, which is used to excite the fluorescent dye molecule. The selection of the laser depends on the fluorescent dye to be employed so that high excitation and emission efficiency can be achieved. In this thesis, two different lasers have been used: a green helium-neon laser (543.5 nm) was used for NR and DiI (see Chapter 3) and an argon ion laser (514 nm) was employed to excite SPDI (see Chapter 3).

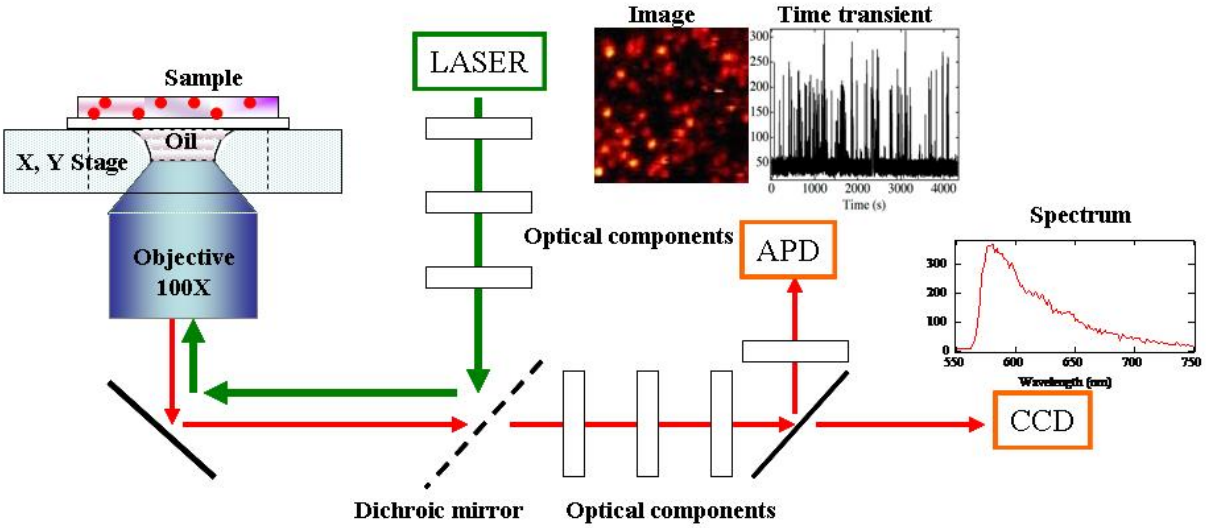


**Figure 2.4.** Sample scanning confocal microscopy. Optics components include lens, flipper mirror, notch filter, bandpass filter, longpass filter.

The alignment of the microscope and detector was verified prior to every experiment. Carboxylate-modified microspheres (0.5μm, red fluorescent, 580nm/605nm) were used to do the alignment for the helium-neon laser (543.5nm), while different carboxylate-modified microspheres (0.2μm, orange fluorescent, 540nm/560nm) were employed for the alignment for the argon ion laser (514 nm).

A typical experiment proceeds as follows. Fluorescence images were acquired by raster scanning the sample above the focused laser spot, using a "closed-loop" piezo-electric stage. The fluorescence signal was integrated for 40 ms per pixel in 100×100 pixel images. The duration for a typical fluorescence image was ~7 min. Single-point fluorescence time transients were obtained by positioning selected sample regions in the laser focus and recording the spectrally integrated fluorescence in time. Individual transients were recorded for up to 3 h, with a typical dwell time of 80 ms. he obtained images were loaded into the ImageJ program (http://rsbweb.nih.gov/ij/) to do further analysis. While the acquired time transient was reloaded

with Igor Pro using a macro to get detained information. Out-of-focus images and time transients were abandoned.

### *2.2.2 Bulk Fluorescence Spectrum Setup*

Fluorescence spectra were obtained from NR-doped gradients and spin-coated films using a home-built fluorescence microscope (see Figure 2.5). Light (~1 μW) from a green HeNe laser (543.5 nm) was used to excite fluorescence in the samples. This light was focused into the back aperture of a 50X (NA=0.55) air objective, producing a 20 μm diameter spot in the sample. The same objective was used to collect the sample fluorescence and direct it through a 543 nm holographic notch filter (Kaiser Optical) and into a 0.15 m spectrograph (Acton Research). A liquid-$N_2$-cooled CCD (Princeton Instruments) was used to record the spectra. ~1L liquid $N_2$ was added to the cooler. Spectra were acquired after the temperature had stabilized at -80 $^oC$. They were taken every 1(±0.2) mm along the gradient, using a 30 s integration time.

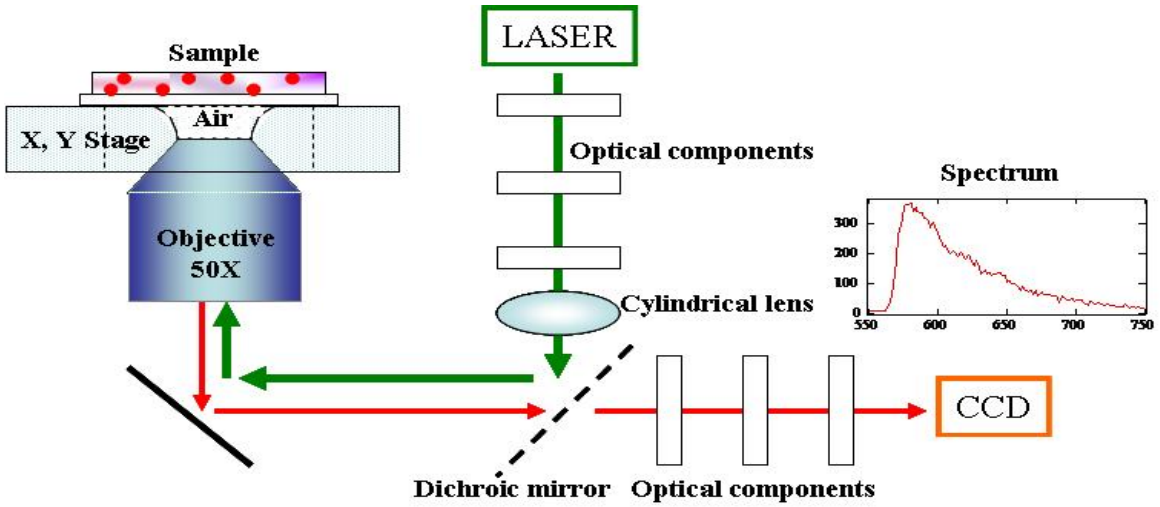


**Figure 2.5.** Fluorescence microscope to take NR spectrum. A cylindrical lens is employed to obtain a large focus area. A 50X air objective was used to minimize the sample contamination by oil in an oil immersion objective.

# CHAPTER 3 - Probing Chemical Interactions at the Single Molecule Level in Mesoporous Silica Thin Films

Two papers have been published based on the research work mentioned in this chapter with the following two citations:

Yi Fu, Fangmao Ye, William G. Sanders, Maryanne M. Collinson* and Daniel A. Higgins* "Single Molecule Spectroscopy Studies of Diffusion in Mesoporous Silica Thin Films", *J. Phys. Chem. B*, **2006**, *110*, 9164.

Fangmao Ye, Daniel A. Higgins* and Maryanne M. Collinson* "Probing Chemical Interactions at the Single Molecule Level in Mesoporous Silica Thin Films ", *J. Phys. Chem. C*, **2007**, *111*, 6772.

In this work, Dr. Yi Fu performed most of the single molecule experiments for Nile Red under dry (20RH) conditions. Mr. Corey R. Weitzel helped to synthesize SPDI, which was used as a negatively charged dye in single molecule study.

## 3.1 Introduction

Mesoporous silica materials prepared by templating silica sols with surfactant assemblies have attracted considerable interest since their discovery more than a decade ago.[50,51] Although once limited to powders and monoliths, the preparation of mesoporous thin films incorporating hexagonal, lamellar, and/or cubic mesophases by either dip coating or spin coating a templated sol onto a suitable substrate is now routine.[54,70,117,138-145] Mesoporous silica films have many advantages over more thoroughly studied "disordered" sol-gel-derived films.[47] These include long-range order, tunable pore size, and narrow pore size distributions. Their surfaces can also be easily modified with specific functional groups[146-148] and they can be loaded with analytical reagents (i.e., dyes)[70,140,141,149-151] via post-synthesis or *in-situ* procedures.

Dye-doped mesoporous materials have numerous applications in the areas of pH sensing,[151] photochromism,[152] solid-state lasers,[153-155] and waveguide assemblies.[155] Of utmost importance to these applications are the mobility of the entrapped dye, its location, and the frequency and strength of its interactions with the pore surfaces, all of which play a profound role in governing ultimate device performance characteristics. Bulk fluorescence spectroscopy has long been used to obtain an average picture of these and other relevant materials properties.[37] For example, the formation of mesoporous thin films during dip coating has been probed by fluorescence methods.[70,141,156] Fluorescence spectroscopy has also been used to characterize the location, accessibility, and interactions of entrapped dyes.[157,158] Unfortunately, the underlying single particle motions and rare events associated with the detailed mechanism(s) of mass transport and molecule-matrix interactions are masked in such bulk experiments.

Proper function of these mesoporous films in their technological applications requires that analytes, reagents and/or products freely migrate into and out of the materials on a

reasonable time scale. The rate at which a given molecule moves through these materials is impacted by the size of the molecule, its charge, the size and configuration of the mesopores, the presence/absence of surfactant, the chemical properties of the pore surfaces and the solvent content of the film.[32,55,76,77,81,82,159,160] Importantly, molecular mobility can also be severely altered by adsorption to reactive sites on the silica surface and by binding of the molecule to the surfactant (when present).[32,55,82,159] In some instances (i.e. separations and catalysis) brief, reversible adsorption events, coupled with efficient mass transport may be desirable. In others, surface adsorption events may be detrimental to device function, leading to the slow response of some sensors[161] and well-known peak tailing in chromatographic applications.[44] Molecules may even become irreversibly adsorbed within the materials, leading to slow "poisoning" of the matrix. A complete understanding of the origins of these and other effects is required if the functional properties of these materials are to be fully optimized. As a result, considerable effort has been directed towards a fundamental understanding of the partitioning of molecules, their mobilities, and the extent of interactions with the surfactant (if present) and the silica surface.[35,55,61,75,90,92,97,98,140,157,158,160,162]

In this chapter, single molecule fluorescence imaging and spectroscopy[38,39,41] are used to study the mass transport and matrix interactions of dye molecule trapped in mesoporous silica thin films of predominately hexagonal order. Dye mobility, dye binding and surface adsorption phenomena in dry and hydrated surfactant-containing and surfactant-free mesoporous silica films are investigated using single molecule spectroscopic methods. Three different dyes are employed to probe a range of relevant materials properties. Nile Red (NR), a neutral, hydrophobic dye provides information on hydrogen bonding interactions and hydrophobic effects in the films. DiI, a cationic dye incorporating long alkane tails, serves as a probe of ionic interactions with the

silica pore surfaces and charged surfactant head groups. Finally, a sulfonated perylene diimide (SPDI) is used as a complementary negatively charged probe of ionic interactions. Quantitative data on the rate of dye molecule diffusion, the extent of surface adsorption and surfactant binding and the duration of reversible surface adsorption events under a range of different conditions are presented. FCS methods[86] have previously allowed for the characterization of single molecule Brownian motion[44,163,164] and rare strong adsorption events[44,61,164] in related materials. FCS methods and single particle tracking[165] have also been applied to the study of such phenomena in commercial and monolithic ordered mesoporous materials by the Dai group[61] and by Brauchle and coworkers.[160] Related studies of disordered mesoporous films have been reported by the Harris group.[90] While much was learned in these earlier studies, they dealt with fundamentally different materials (some were monoliths) that were prepared by different methods. It is particularly noteworthy that monoliths and thin film mesoporous materials are expected to have different properties in part because of differences in the rates at which hydrolysis, condensation, and solvent evaporation occur. This work deals specifically with materials that have not previously been studied by single molecule methods: surfactant-containing and calcined mesoporous thin films of hexagonal order. The results show there is clear temporal heterogeneity in the mobilities of dye molecules found within these films. Frequent, reversible adsorption of the dye to the surfactant-silica interface is noted in both surfactant containing materials and those that have been calcined, reloaded with dye, and rehydrated by exposure to humid environments. What's more, as expected, different behaviors (diffusion rate, adsorption rate, sensitivity to the hydration degree, etc.) for three different dyes are observed.

## 3.2 Experimental Section

### *3.2.1 Sample Preparation.*

Samples were prepared as follows. Silica sols were prepared by mixing tetramethoxysilane (99%, TMOS, Aldrich), deionized water, absolute ethanol and HCl in a small vial. The sol was stirred for 1 h after the addition of the above components and was then allowed to sit for an additional 24 h at room temperature. Cetyltrimethylammonium bromide (CTAB, Aldrich) or sodium dodecyl sulfate (SDS, Aldrich) was then dissolved in the solution by vigorous stirring for 1 h. The final molar ratios of the components in these sols were typically 1:5.6:8:0.003:0.2 for TMOS:$H_2O$:Ethanol:HCl:CTAB and 1:16.8:8:0.003:0.05 for TMOS:$H_2O$:Ethanol:HCl:SDS. For the preparation of dye-doped mesoporous films, either a methanolic solution of Nile Red (NR, Aldrich), a methanolic solution of 1,1'-dihexadecyl-3,3,3',3'-tetramethylindocarbocyanine perchlorate (DiI, Invitrogen) or an aqueous solution of N,N'-bis(3-sulfonatopropyl)perylene-3,4,9,10-tetracarboxylic diimide (sulfonated perylene diimide, SPDI) was added to a portion of the above sol to yield a total dye concentration of 0.5 nM. Approximately 65 μL of the sol was then spin cast (30s at 6000 RPM) onto a clean glass coverslip (Fisher Premium) immediately after addition of the dye. The films were subsequently dried overnight at room temperature in a desiccator before use. The thickness of these films was determined by profilometry (Ambios Technology; Santa Cruz, CA) to be 770±60 nm. Small angle X-ray diffraction (XRD) data from the CTAB-containing films indicate they incorporate hexagonally-organized mesopores of 35 Å periodicity (d-spacing), with the pores running parallel to the film plane. XRD data from SDS-containing films show they incorporate lamellar structures of 37 Å periodicity. Films studied without further treatment are referred to as "as-synthesized" films throughout this chapter.

Surfactant-free mesoporous silica films were obtained by calcining the as-synthesized (CTAB containing) films in a furnace. In this process, the films were first heated at 160$^{o}$C for 90 min. The temperature was then increased to 350$^{o}$C at a rate of 1$^{o}$C/min, where it was held for 5 h. After cooling to room temperature, the films were treated in an air plasma (Harrick Plasma) for 2-3 min to remove residual luminescent impurities that otherwise yielded significant background in the single molecule experiments. The calcined, plasma treated films were then reloaded with dye by soaking them in 1 nM dye solution for 1 h, followed by rinsing with ethanol to remove loosely bound dye. These films were also dried in a desiccator overnight before use. The final thickness of the calcined films was measured to be 400±30 nm. XRD data from these films are also consistent with hexagonal mesopores. However, the mesopores in the calcined films have collapsed and disordered somewhat, exhibiting 24 Å periodicity.[55]

Both dry and rehydrated as-synthesized and calcined samples were studied. Dry as-synthesized and calcined-reloaded films were maintained in a dry environment (i.e. under dry air at 20% relative humidity (RH)) throughout the recording of images and time transients, as described below. Rehydrated as-synthesized and calcined films were stored at a controlled humidity (i.e. 30, 40 or 50% RH) for ≈ 12 h prior to use. They were maintained under these same humidity conditions throughout data collection.

### *3.2.2 Instrumentation.*

All single-molecule studies were conducted on a sample scanning confocal microscope that had been described previously[79,99] and was shown in Figure 2.4 in Chapter 2. Briefly, this system is built on an inverted epi-illumination microscope (Nikon TE-200). Light from either a green helium-neon laser (543.5 nm, used for NR and DiI) or from an argon ion laser (514 nm, used for SPDI) was reflected from an appropriate dichroic beamsplitter into the back aperture of

an oil immersion objective (Nikon Plan Fluor, 1.3 numerical aperture, 100X magnification). This objective was used both for illuminating the sample, yielding a nearly diffraction limited focus of ≈ 300 nm $1/e^2$ radius, and for collecting the resulting single molecule fluorescence. The incident laser power was always maintained in the 200-400 nW range (estimated from measurements made external to the microscope). An electronic shutter was used to control illumination of the sample. Fluorescence collected from the sample was isolated from the excitation light by passage back through the dichroic beamsplitter, an appropriate holographic notch filter, and a bandpass filter. A single-photon-counting avalanche photodiode was used as the detector.

Fluorescence images were acquired by raster scanning the sample above the focused laser spot, using a "closed-loop" piezo-electric stage. The fluorescence signal was integrated for 40 ms per pixel in the 100×100 pixel images. Single-point fluorescence time transients were obtained by positioning selected sample regions in the laser focus and recording the spectrally integrated fluorescence in time. Individual transients were recorded for up to 3 h, with a typical dwell time of 80 ms. All single molecule experiments were performed under controlled humidity conditions at 20, 30, 40 and 50% RH as noted above.

### *3.2.3 Simulations.*

Simulated time transients[43] and fluorescence images were employed to help interpret the experimental time transients and images.[92] In these studies, simulated data were numerically generated for perfectly homogeneous samples. Molecules were positioned randomly in a 30 X 30 $\mu m^2$ region with an areal density near 0.5 molecules/$\mu m^2$. The exact parameters used in each simulation are defined in the individual instances where such data are used (see below). The number of molecules present in the region was kept constant by having molecules that diffuse

out of one edge of the region "wrap around" to reenter on the opposite side. During each time slice, $\Delta t$, each molecule was displaced from its previous position by a step of random size. The step size probability distribution was a Gaussian with a mean-square width of $2D\Delta t$ in each of the two dimensions simulated (in the sample plane). All molecules were assigned the same D value. This value was varied somewhat, as defined below, but was nominally held near $2x10^{-10}$ $cm^2/s$, consistent with experimental results. The Gaussian excitation spot was positioned at the center of the 30 X 30 $\mu m^2$ region and had a variance, $s^2$, of $2.3x10^{-10}$ $cm^2$. The maximum signal from each single molecule was set to 200 counts per data point. Signal variations due to rotational motions were not included in the simulations. A background signal equivalent to 20% of the signal was added to each transient. Random variations were also added to the signal and background counts to simulate the effects of shot noise. Time transients obtained in this manner were then treated identically to the experimental data.

## 3.3 Result and Discussion

### *3.3.1 X-ray Diffraction.*

Figure 3.1 shows typical XRD patterns obtained from the mesoporous films before and after calcination. The XRD pattern of the as-synthesized (i.e. surfactant-containing) silica film is most consistent with a hexagonal structure, having characteristic (100) and (200) peaks at $2\theta$ = 2.59˚ and 4.96˚, respectively. These results yield a d-spacing of ≈ 35±0.5 Å. The absence of the (110) diffraction peak (expected at $2\theta$ = 4.41˚) indicates that the channels run parallel to the substrate surface. Two smaller peaks observed in the $2\theta$ = 2-4$^o$ region likely indicate the films also incorporate some features of 3D hexagonal or cubic symmetries. XRD data obtained after removal of the CTAB by calcination (i.e. in the dry films) exhibit a less intense, broad, single

peak at 2θ = 3.70˚, corresponding to a d-spacing of 23.9 Å (see Figure 3.1). These results reflect a 30% contraction and possible disordering of the mesoporous structure during calcination. Little or no change in the film structure is observed upon rehydration at 50% RH (data not shown). Neither addition of Nile Red to the sol, nor its addition to the calcined films cause observable changes in any of these structures.

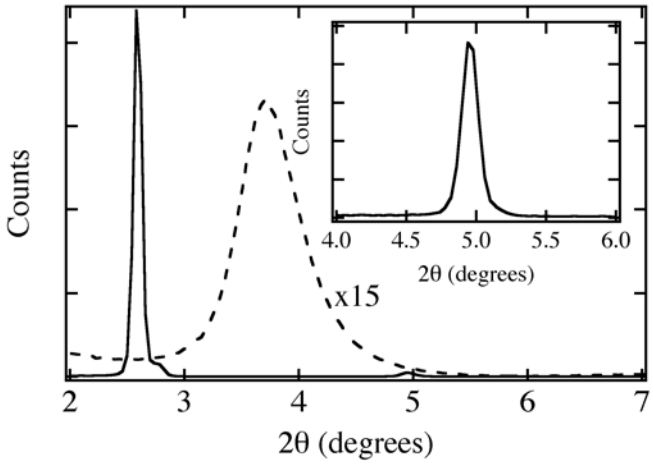


**Figure 3.1.** Small angle X-ray diffraction data for the as-synthesized (——) and dry calcined (- - - -) mesoporous silica thin films. The intensity of the broad peak from the calcined sample has been increased 15-fold. The inset depicts the (200) peak from the as-synthesized sample.

### *3.3.2. FTIR spectrum.*

FTIR spectra of as-synthesized (surfactant-containing) mesoporous silica films and rehydrated and dry calcined mesoporous films are shown in Figure 3.2. These spectra were recorded for films deposited on silicon substrates. The broad absorption peaks around 3265 $cm^{-1}$ (strong) and 1630 $cm^{-1}$ (weak) for the as-synthesized film indicate there is some water entrapped in the surfactant-filled mesopores.

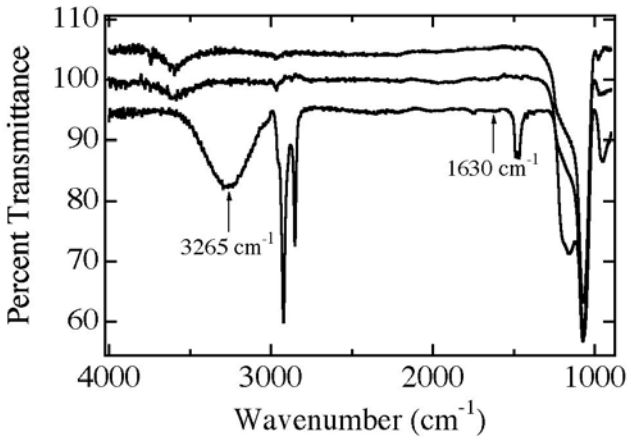


**Figure 3.2.** FTIR spectra obtained from as-synthesized (lower spectrum), rehydrated (middle) and dry calcined (upper spectrum) mesoporous silica films deposited on silicon substrates. The baselines on all spectra have been flattened and offset in the cases of the as-synthesized and dry calcined films.

### *3.3.2 General Properties of NR, DiI and SPDI.*

Figure 3.3 shows the chemical structures of the three dyes used in these studies. Both NR[79,99,101,166] and DiI[167-169] have been used in numerous single molecule studies to date. While SPDI has not been used previously in such investigations, closely-related perylene diimides have.[170-172] The bulk absorption and emission maxima (all in ethanol solution) are located at 550 nm and 625 nm for NR, 545 nm and 585 nm for DiI, and 525 nm and 565 nm for SPDI, respectively. Because the SPDI absorption and emission maxima occur to the blue of those for DiI and NR, two different lasers were used for excitation of the three dyes.

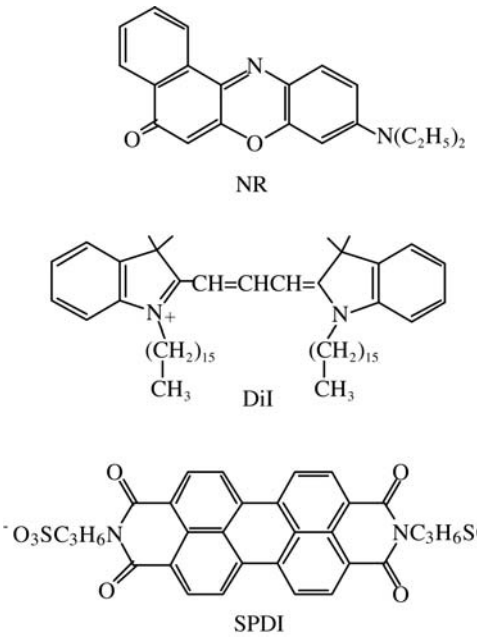


**Figure 3.3.** Chemical structures for NR, DiI and SPDI.

NR, DiI and SPDI were selected for use specifically because they are expected to have different interactions with the silicate matrix, residual solvent and/or the surfactant. NR is an uncharged molecule; DiI has one positive charge and two eighteen-carbon alkane tails; and SPDI can have up to two negative charges, depending on the pH. NR is expected to be the most hydrophobic of the three and should exhibit the best solubility in the organic regions of the micelles within as-synthesized silica films. Its only interactions with the silica matrix are expected to occur via hydrogen bonding to its quinonal oxygen.[79] Because of its surfactant-like nature, DiI should also be positioned within the surfactant phase of the as-synthesized materials. However, its cationic headgroup should be located in the ionic outer regions of the micelles. It is also expected to exhibit strong ionic interactions with the negatively-charged silica surface. Finally, the anionic SPDI molecules are also expected to position themselves near the ionic outer regions of the surfactant micelles. The SPDI molecules are expected to show the weakest interactions with the silica matrix.

All three dyes possess "rigid" chromophores of approximately the same shape and size, having oblong structures with long dimensions of 12-14 Å. The only significant difference in molecular size arises from the presence of bulky alkane groups on DiI. The largest dimensions of all three molecules fall in the 13-22 Å range, with overall size increasing in the order NR < SPDI < DiI. Because these size variations are small and occur predominantly along a single molecular dimension, they are not expected to play a dominant role in determining molecular mobility.

### *3.3.3 Imaging and Image Autocorrelation.*

#### *3.3.3.1 Image.*

Typical 10 X 10 $\mu m^2$ fluorescence images recorded for an as-synthesized mesoporous film doped with Nile Red and a dry calcined film reloaded with Nile Red are shown in Figures 3.4A,B. An image obtained from an undoped, calcined dry film is also shown for comparison (Figure 3.4C), as is a simulated image (Figure 3.4D). Images like those shown in Figures 3.4A,B are most frequently used to locate single molecules and specific sample regions for further analysis. However, they also give initial, qualitative information on the molecular scale properties of the films. Images obtained from the as-synthesized films incorporate a few bright round fluorescent spots of diffraction-limited size, but are dominated by the many "streaks" that appear. These image streaks are reflective of line-by-line variations in the single molecule emission. Images recorded for rehydrated calcined films imaged at 50% RH were virtually indistinguishable from those of the as-synthesized films and were also dominated by "streaks". In contrast, the dry (imaged at 20% RH) calcined films show predominantly round fluorescent spots (having Gaussian intensity profiles), with relatively few fluctuations occurring on a time scale similar to the image pixel time. Bulk FTIR spectra of these films show that the as-

synthesized films contain the most water, followed by the rehydrated calcined films, while the dry calcined films incorporate little or none.

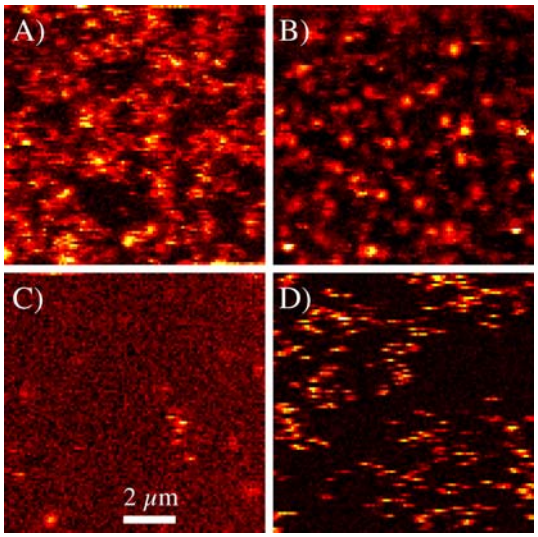


**Figure 3.4.** Fluorescence images of 10 x 10 $\mu m^2$ sample regions recorded for (A) as-synthesized mesoporous silica containing Nile Red at sub-nanomolar concentrations, (B) a dry calcined mesoporous film (imaged at 20% RH) also containing Nile Red in low concentrations, and (C) a blank image recorded for a calcined film, absent Nile Red. (D) Simulated image obtained assuming an areal molecular density of 0.5 molecules/$\mu m^2$, with each molecule having a diffusion coefficient of $2x10^{-10}$ $cm^2/s$.

The bright round image spots in the dry calcined films are attributable to fluorescence from single molecules entrapped at fixed positions, whereas the streaks arise from temporal variations in the single molecule excitation and/or emission rates.[79,92,99] These temporal variations could result from translational and rotational diffusion,[66] spectral diffusion,[173] triplet blinking,[174] and/or variations in the quantum yield due to the formation of a nonfluorescent twisted internal charge transfer (TICT) state. The TICT state in Nile Red forms most readily in polar media.[79,99,175]

The relative numbers of "spots" and "streaks" observed in a given image have been shown previously to depend on the presence of residual solvents and the exact procedures used

in film drying.[79,92,99,123,175] It has also been shown that certain dye-doped organically-modified silicate films exhibit significant image streaking due to rapid molecular diffusion through fluid-filled environments found within these films.[92,99] It was concluded that the fluid-filled domains were comprised of liquid-like organosilicate oligomers.

The hydrated surfactant assemblies of the as-synthesized films and the "water-filled" pores of the rehydrated calcined samples are believed to behave as the "fluid-filled" domains, facilitating translational (and rotational) diffusion. Comparison of the experimental and simulated fluorescence images shown in Figures 3.4A and 3.4D reveals that they are qualitatively similar, indicating translational diffusion could indeed be the root cause of the image streaks. The simulated image shown was obtained as described above, assuming a molecular density of 0.5 molecules/$\mu m^2$, with each molecule having a diffusion coefficient of $2x10^{-10}$ $cm^2/s$. The pixel time and simulated "scan rate" were identical to those used in the recording of the experimental data.

It is noteworthy that some streaks appear even in images of the dry calcined samples, and that some round spots are found in images otherwise dominated by streaks. In the dry calcined samples, many such fluorescence fluctuations can be attributed primarily to triplet blinking[174]and possible quantum yield fluctuations due to intermittent formation of the TICT state.[79,99,175] The round spots observed in the as-synthesized films are due to molecules entrapped at fixed locations on the imaging time scale. Such spots do not appear in the simulated images (Figure 3.4D), suggestive of either substantial heterogeneity in the diffusion coefficient for different film regions, or momentary adsorption of the diffusing species to the silica surface. Distinction between these two mechanisms can only be made by the recording and analysis of time transients, as described below.

### *3.3.3.2 Image Autocorrelation.*

Quantitative information on the molecule-matrix interactions occurring in dye-doped mesoporous silica films is obtained by fluorescence correlation spectroscopy (FCS) methods.[44,55,86] Accurate results in FCS studies can only be obtained when detailed knowledge of the excitation spot size in the sample is available. Such information is obtained in the present studies by recording and autocorrelating fluorescence images of dye-doped mesoporous films incorporating immobile single molecules.[176]

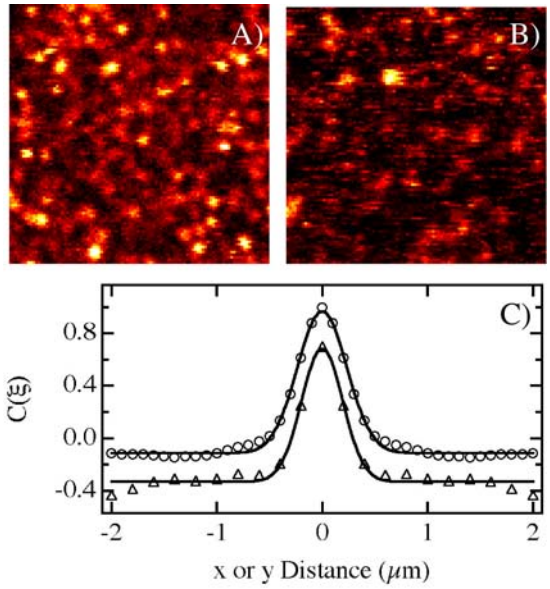


**Figure 3.5.** A) Fluorescence image of a calcined mesoporous silica film reloaded with DiI and recorded under dry (20% RH) conditions. B) Fluorescence image of a similar DiI-doped film imaged at 50% RH. Both images are of 10×10 $\mu m^2$ regions. C) Autocorrelations along the horizontal (circles) and vertical (triangles) directions for the image shown in A). Fits to Eqn. 3.2 are depicted by the solid lines.

Images of dry (20% RH) calcined films doped to nanomolar levels with any of the three dyes are observed to incorporate bright round fluorescent spots, consistent with excitation and emission of single molecules entrapped at fixed positions. Figure 3.5A shows a representative fluorescence image of a DiI-doped dry calcined film. Proof that the molecules are entrapped at

fixed locations on the experimental time scale is reflected in the autocorrelation functions obtained from such images.

Autocorrelations of the images were calculated as follows:[176]

$$C(\xi) = \frac{\langle i(x)i(x+\xi)\rangle}{\langle i(x)\rangle^2} - 1 \tag{3.1}$$

Here, i($x$) represents an intensity trace taken along the horizontal ($x$) or vertical (y) image directions. The brackets indicate that the average over all points in each trace is taken. Figure 3.5C depicts the average autocorrelation functions obtained in the x and y directions[92] for the image shown in Figure 3.5A. The data density in the y direction is half that in the x direction for experimental reasons (i.e. bidirectional scanning was employed).[92]

Images of samples incorporating fixed molecules yield autocorrelation functions that are readily fit to the following Gaussian expression:

$$C(\xi) = A\exp\left(-\left(\frac{\xi}{2s}\right)^2\right) + B \tag{3.2}$$

In Eqn. 3.2, $s^2$ represents a measure of the excitation spot size (i.e. the beam variance),[44] and A and B are constants. Images of dry calcined films doped with DiI and acquired using 543.5 nm excitation yielded a mean beam variance of $2.6(\pm0.2)\times10^{-10}$ cm$^2$. Similarly, image autocorrelation data derived from dry calcined films doped with SPDI and imaged using 514.5 nm excitation could also be fit to Eqn. 3.2 and yielded a similar mean beam variance of $2.7(\pm0.2)\times10^{-10}$ cm$^2$. Because these two beam variances are the same within experimental error, all subsequent autocorrelation functions (both temporal and spatial) were analyzed using $s^2 = 2.6\times10^{-10}$ cm$^2$.

In contrast to the dry calcined films described above, images recorded for rehydrated as-synthesized and calcined films frequently exhibit obvious line-by-line variations in single molecule emission. Figure 3.5B shows a representative image of a rehydrated (50% RH) DiI-doped calcined sample, depicting such behavior. Previous studies have shown that Brownian motion of the molecules is an important contributor to the "streaky" appearance of these images.[79,92,99] Image autocorrelations can provide information on the relative contributions of fixed and mobile molecules to the image contrast. However, because these data incorporate both temporal and spatial information, and because the data density is limited, accurate information on molecular mobility cannot readily be obtained from this analysis. Therefore, image autocorrelation procedures were used almost exclusively for determining the beam focus size.

### *3.3.4 Fluorescence Time Transients and Autocorrelations.*

#### *3.3.4.1 Fluorescence Time Transients.*

FCS data obtained from single point time transients provides the most accurate means for exploring diffusion and molecule-matrix interactions in the mesoporous silica films.[44,45,55,61,160,164] Time transients obtained from the different samples studied exhibit distinctly different behaviors that are consistent with a variable level of molecular mobility. Figure 3.6A shows a representative time transient obtained from a rehydrated (50% RH) DiI-doped as-synthesized film, which is similar to those time transiets recorded from NR doped as-synthesized (dry and rehydrated) and DiI-doped as synthesized (30RH, 40RH and 50RH) and SPDI doped rehydrated calcined film. The transient exhibits short bursts of fluorescence separated by periods over which only background counts are observed. These bursts continue to occur even over extremely long times (hours), indicating that they arise from the translational diffusion of different single molecules into and out of the detection volume of the microscope. This behavior

stands in stark contrast to that depicted in Figure 3.6B, which shows a representative time transient obtained from a dry (20% RH) as-synthesized DiI-doped sample, which is similar to those time transiets recorded from NR doped calcined(dry) and DiI-doped as synthesized (20RH) and SPDI doped as-synthesized (dry and rehydrated) and SPDI calcined film (dry). Here, a constant level of emission (aside from shot-noise fluctuations) is observed for a brief period of time, after which the signal abruptly and permanently drops to background. This latter behavior is consistent with detection of a single, immobile dye molecule.

Upon closer inspection of transients like the one shown in Figure 3.6A, it is clear that they often depict a mixture of behaviors. For example, Figure 3.6C shows an expanded region of the transient given in Figure 3.6A, depicting a fluorescence burst that is too long to be attributed to translational diffusion of a molecule through the excitation volume. The event shown has a duration of ≈ 26 s, while the average burst length due to diffusing molecules in this transient is 0.7 s. Furthermore, the fluorescence signal observed during this event is relatively constant, aside from shot noise fluctuations. As has been discussed for surfactant-containing samples[55,160] these events can be attributed to strong, reversible surface adsorption of the dye molecules. Similar events are observed for all three dyes in different samples studied under certain conditions (see below).

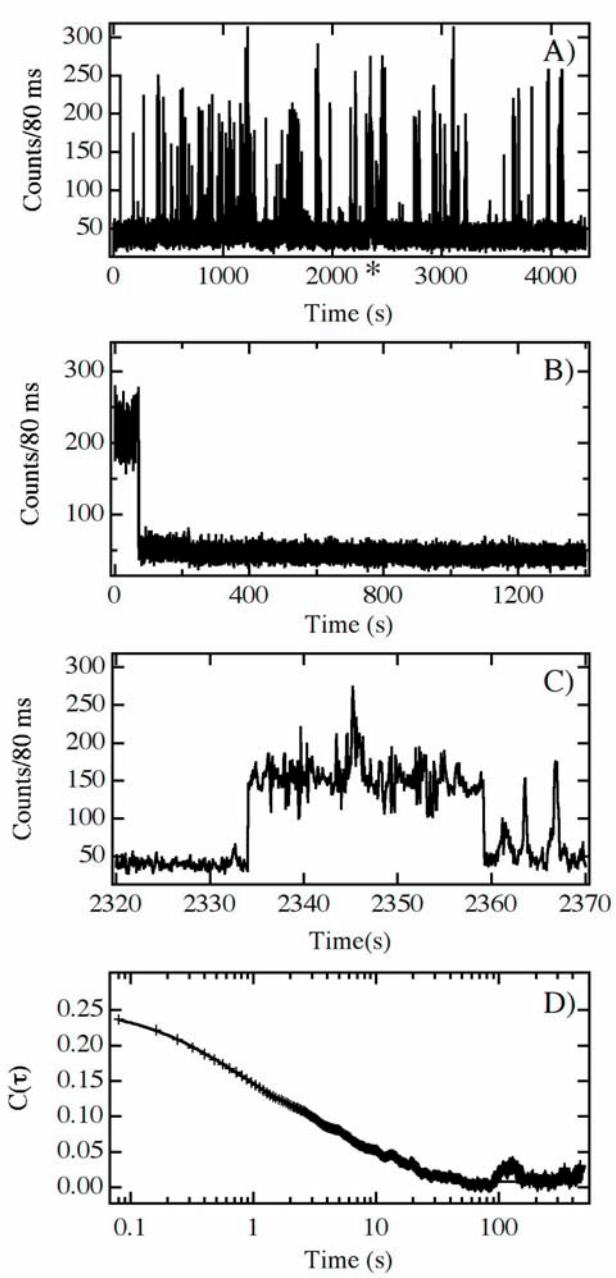


**Figure 3.6.** A) Representative fluorescence time transient recorded for DiI in a rehydrated (50% RH) as-synthesized mesoporous silica film. B) Fluorescence transient recorded for a fixed DiI molecule in a dry (20% RH) as-synthesized film, C) Expanded region from A depicting a long burst event. The expanded region in A is marked by an asterisk. D) Autocorrelation of the time transient shown in A (symbols) and its fit to Eqn. 3.4 (solid line).

***3.3.4.2 Autocorrelation.***

Characterization of molecular diffusion and surface adsorption phenomena in the present studies was accomplished by recording numerous single-point fluorescence time transients for the full range of samples studied. Autocorrelation of the transients obtained in the presence of mobile molecules provides quantitative data on the rate of single molecule diffusion and the duration of reversible adsorption events. It also provides a measure of the relative contributions of diffusion and reversible adsorption to the fluorescence fluctuations observed.

Single point autocorrelation functions, $C(\tau)$ were calculated as follows:

$$C(\tau) = \frac{\langle i(t)i(t+\tau)\rangle}{\langle i(t)\rangle^2} - 1 \tag{3.3}$$

In Eqn. 3.3, i(*t*) represents the fluorescence time transient. Time transients analyzed here were all recorded with 80 ms resolution. The autocorrelated data were subsequently fit to a model decay function selected for its inclusion of both two-dimensional diffusion (within the film plane) and reversible surface adsorption, as defined in Eqn. 3.4:[43,44,61]

$$C(\tau) = \frac{A_d}{1 + D\tau / s^2} + A_a \exp(-\tau k) \tag{3.4}$$

Here, D is the diffusion coefficient for the dye, $s^2$ is the beam variance (determined above), k is the rate constant for desorption of adsorbed species and $A_d$ and $A_a$ are the amplitudes of the diffusion and adsorption components of the decay, respectively. In the data presented below, the relative contributions of diffusion and adsorption to the time transients are employed. The relative $A_d$ and $A_a$ values were obtained by normalizing each to the total amplitude of the decay:

$$A_d(\text{relative}) = \frac{A_d}{A_d + A_a} \tag{3.5}$$

Figure 3.6D presents the autocorrelation function obtained from the time transient shown in Figure 3.6A. Also shown in Figure 3.3D is the curve fit obtained using Eqn. 3.4. This particular fit yields a diffusion coefficient of $3.7\times10^{-10}$ $cm^2/s$, a desorption rate constant (k) of 0.080 $s^{-1}$ and a relative $A_d$ of 0.70. This same procedure was used to analyze several hundred time transients obtained from the full range of samples studied herein. The results are described below in separate sections for the as-synthesized and calcined samples.

As a caveat to the model in Eqn. 3.4, it should be noted that several different phenomena, including triplet blinking[174] and other fluorescence fluctuations[166,170,175] can also lead to similar autocorrelation decays. However, no evidence of triplet blinking was observed in transients recorded with 80 ms resolution. Likewise, time transients recorded as a function of incident power showed no detectable power dependence, indicating the majority of fluctuations observed were not due to photoinduced phenomena. Therefore, it is concluded that molecular mobility is the dominant cause of the observed fluorescence fluctuations.

As expected, the DiI, NR and SPDI dyes all show dramatically different time dependent behaviors in the as-synthesized and calcined samples. The behavior observed in each case also exhibits a marked dependence on the level of film hydration, as determined by the ambient RH. Table 3.1 presents $A_d$, D, and k values obtained from the majority of samples studied. Since the entire inhomogeneous distribution is obtained in single molecule studies, Table 3.1 reports both the average (bulk like) and the most common values obtained. Results from CTAB-containing films will be discussed first, followed by those obtained from SDS-containing films. Those of the calcined films are presented last.

| Dye | Sample | RH | Mean or Peak[1)] | D ($x10^{-11}$ $cm^2/s$) | $A_d$ (relative)[2)] | k ($s^{-1}$) | No.[4)] |
|---|---|---|---|---|---|---|---|
| DiI | As synthesized | 20 | | NA [5)] | | | |
| | | 30 | Mean | 9±2[3)] | 0.37±0.05 | 0.06±0.02 | 65 |
| | | | Peak | 2.2±0.1 | 0.32±0.01 | 0.014±0.002 | |
| | | 40 | Mean | 13±2 | 0.44±0.05 | 0.07±0.02 | 74 |
| | | | Peak | 8.4±0.3 | 0.37±0.01 | 0.045±0.009 | |
| | | 50 | Mean | 30±8 | 0.51±0.04 | 0.10±0.03 | 79 |
| | | | Peak | 14.4±0.3 | 0.50±0.01 | 0.044±0.001 | |
| | Calcined | 20 | NA | | | | |
| | | 50 | Mean | 31±5 | 0.56±0.04 | 0.052±0.009 | 77 |
| | | | Peak | 24.3±0.6 | 0.55±0.01 | 0.040±0.001 | |
| SPDI | As synthesized | 20 | NA | | | | |
| | | 50 | | | | | |
| | Calcined | 20 | NA | | | | |
| | | 50 | Mean | 40±4 | 0.58±0.04 | 0.08±0.01 | 83 |
| | | | Peak | 32.8±0.3 | 0.59±0.01 | 0.056±0.001 | |
| NR | As synthesized | 20 | Mean | 24±8 | 0.43±0.04 | 0.04±0.01 | 79 |
| | | | peak | 10.3±0.1 | 0.35±0.01 | 0.037±0.002 | 79 |
| | | 50 | Mean | 27±9 | 0.58±0.07 | 0.07±0.02 | 20 |
| | Calcined | 20 | NA | | | | |
| | | 50 | Mean | 29±5 | 0.53±0.03 | 0.048±0.008 | 72 |
| | | | Peak | 21.0±0.3 | 0.51±0.01 | 0.031±0.001 | |

**Table 3.1.** Mean and peak diffusion coefficients, $A_d$(relative) and desorption rate constant (k) for the three dyes under different RH (20, 30, 40 or 50 RH) and in different films (as-synthesized or calcined).

[1)]peak value from Gaussian fitting, [2)]$A_d(\text{relative})=A_d/(A_d+A_a)$, [3)]error bars indicate 95% confidence interval, [4)]number of time transients, [5)]NA indicates the molecules photobleach or diffusion is too slow to detect.

## 3.5 As-synthesized CTAB-Containing Mesoporous Silica Films.

Transients obtained from SPDI molecules in CTAB-containing films almost exclusively end in discrete, irreversible photobleaching events (i.e. similar to that shown in Figure 3.6B), indicating the molecules are adsorbed at fixed locations in these films. Importantly, this behavior is observed under all conditions investigated (i.e. 20-50% RH). In this case, there are obviously strong interactions between the dye and the film that occur even when the film is hydrated. It is known that charged, water-soluble perylene diimides form strong, water-insoluble ionic complexes with oppositely-charged surfactants.[177,178] These strong ionic interactions are the likely cause of SPDI immobility in the CTAB-containing materials. It is concluded the SPDI molecules are located at the silica/surfactant interface, near the charged surfactant head groups. While the nonpolar conjugated ring structure of SPDI suggests it should be soluble in the interior of the micelles, the molecules would remain mobile under such circumstances (see NR data below). Since virtually all SPDI molecules appear to be adsorbed at fixed sites in these materials, such hydrophobic effects are clearly less important. While SPDI could form hydrogen bonds to the silica surface via its imide oxygens, such effects are concluded to be negligible, because of the immobility of these molecules even in hydrated films.

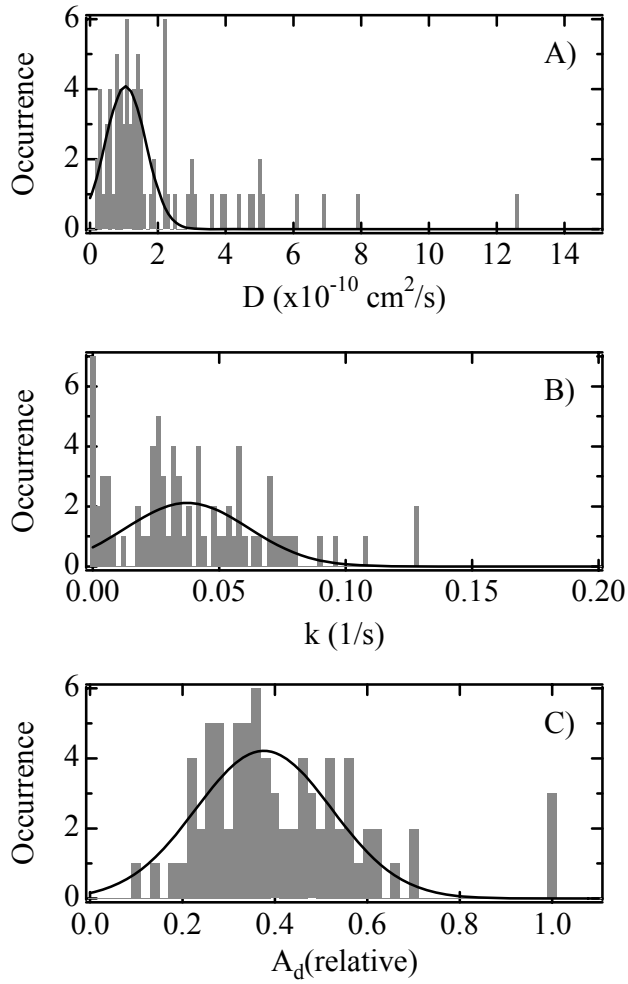


**Figure 3.7**. Histograms showing the distributions of measured D values (A), k values (B), and amplitudes (C) of the diffusional component of the autocorrelation decays relative to total decay amplitude for as-synthesized samples.

In contrast to SPDI, NR shows different results. Figure 3.7 depicts histograms of the diffusion coefficients and desorption rate constants obtained by fitting all 79 autocorrelations (see table 3.1). From these data, an average D of 2.4(±0.8)x10$^{-10}$ cm$^2$/s (error bars indicate the 95% confidence interval) is obtained for Nile Red in the as-synthesized mesoporous films. Fitting of the histogram in Figure 3.7A to a Gaussian function yields a value for the most common D of 1.1x10$^{-10}$ cm$^2$/s. Likewise, average and most common values for k are determined

to be 0.040 $s^{-1}$and 0.037 $s^{-1}$, respectively, consistent with a characteristic mean desorption time of 25(±9) s. Similarly, an average D of 2.6(±1.0)x$10^{-10}$ $cm^2/s$ and a mean desorption time of 40(±10) s are obtained from the rehydrated calcined samples. Note that the mean desorption times reflect the average length of time the molecules spend adsorbed to the silica surface, while the simulated time transients yielded only very few rare diffusive events of this same length.

The widths of the D and k distributions shown in Figure 3.7 are believed to be due almost entirely to errors associated with fitting the autocorrelation data.[92] They do not appear to reflect a significant level of heterogeneity in either diffusional or adsorption/desorption processes. This conclusion is consistent with sample heterogeneity occurring over length scales much smaller than the diffraction limited focus of the microscope.

Figure 3.7 also depicts a histogram showing the apparent relative contributions of diffusion and adsorption to the autocorrelation decays (see Eqn. 3.5) for the as-synthesized samples. An average relative $A_d$ of 0.43(±0.04) is obtained for the as-synthesized films, along with an average relative $A_a$ of 0.57(±0.04). For the rehydrated calcined samples, similar results are obtained with $A_d$ = 0.6(±0.1) and $A_a$ = 0.4(±0.1). These results indicate that a significant fraction of each autocorrelation decay arises from reversible adsorption events in both the as-synthesized and rehydrated calcined samples. However, the frequency of adsorption is clearly different, with the $A_d$ (and $A_a$) values differing at better than the 95% confidence level between the two samples.

Furthermore, NR mobility is only modestly dependent on the level of film hydration, exhibiting an average D of 27×$10^{-11}$ $cm^2/s$ in hydrated (50% RH) films. While this value differs modestly from that observed in the dry films, the change in D over the range of samples studied is relatively small compared to that observed for DiI (see below).

The mobility of NR likely results from its hydrophobic nature, which makes it soluble in the nonpolar regions of the CTAB micelles. Unlike SPDI, however, NR is uncharged, and therefore has no ionic interactions with the surfactant headgroups. As a result, NR spends much of its time moving through the fluid, nonpolar regions of the micelles. Water incorporated in the films even under dry conditions may also play a role in NR mobility. As shown in Figure 3.2, FTIR spectra recorded for dry (20% RH) as-synthesized films cast on silicon substrates exhibit a relatively strong, broad absorption at 3265 $cm^{-1}$, consistent with the presence of bulk water in these films. However, the weak dependence of NR mobility on the ambient RH suggests the surfactant phase itself plays a dominant role in facilitating dye molecule motions.

While the NR molecules are highly mobile in these films, their time transients also exhibit clear evidence of frequent, reversible surface adsorption. Long fluorescence bursts exhibiting stable emission are observed (similar to that shown in Figure 3.6C). It is concluded the molecules occasionally approach the silica surface, where they form hydrogen bonds with surface silanols. The average time each molecule spends adsorbed (1/k) to the surface under dry conditions (20% RH) was found to be 25 s. The average duration of the adsorption events was also found to depend on the level of film hydration, yielding a value of 14 s in hydrated films (50% RH). Likewise, the diffusive component of the autocorrelation decay makes a dominant contribution at high RH ($A_d = 0.58$) while the absorptive component dominates at low RH ($A_d = 0.43$). Such behavior is expected since water molecules will effectively compete with NR for the hydrogen bonding sites on the silica surface in the hydrated thin films. The length of time each NR molecule spends adsorbed to the surface is thus reduced.

Among the three dyes employed, DiI is the most sensitive to changes in film hydration. DiI molecules in the dry (20% RH) as-synthesized samples appear to be adsorbed at fixed

locations and do not move on the experimental time scale. This result contrasts with that of NR, for which the molecules were observed to be relatively mobile under these same conditions. The DiI molecules then become significantly more mobile as the ambient RH is increased. Figure 3.8 depicts histograms of the D values obtained. The average D is measured to be $9\times10^{-11}$ $cm^2/s$, $13\times10^{-11}$ $cm^2/s$ and $30\times10^{-11}$ $cm^2/s$, in films hydrated at 30, 40 and 50% RH, respectively. The most common values, reflecting the peak of each inhomogeneous distribution are measured to be $2.2\times10^{-11}$ $cm^2/s$, $8.4\times10^{-11}$ $cm^2/s$, and $14.4\times10^{-11}$ $cm^2/s$ under these same conditions.

The immobility of DiI at 20% RH indicates that the molecules are strongly adsorbed to the silica surface under these circumstances. Were it found entirely within the nonpolar regions of the surfactant micelles, it would be expected to be mobile even in the dry films, as was observed for NR. The much stronger "permanent" adsorption of DiI under dry conditions suggests adsorption involves strong ionic interactions of the cationic dye with the anionic silica surface. Silica surfaces are known to have pI ≈ 2,[113] suggesting the surfaces in these mesoporous materials are negatively charged, even under the low pH conditions (pH ≈ 3.8) used in their preparation. Dramatically enhanced DiI mobility under hydrated conditions then results from solvation of the ionic dye and surface species.

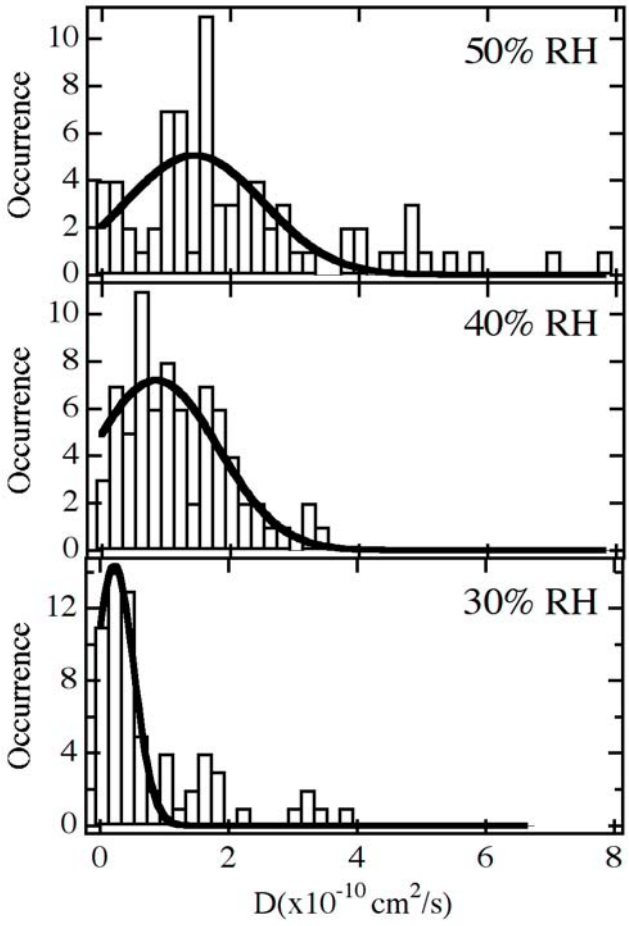


**Figure 3.8**. Histograms showing the distribution of measured D values for DiI-doped as-synthesized mesoporous silica films characterized at 50% RH, 40% RH and 30% RH. The solid lines depict the Gaussian fits to each histogram used to determine the peak of the distribution.

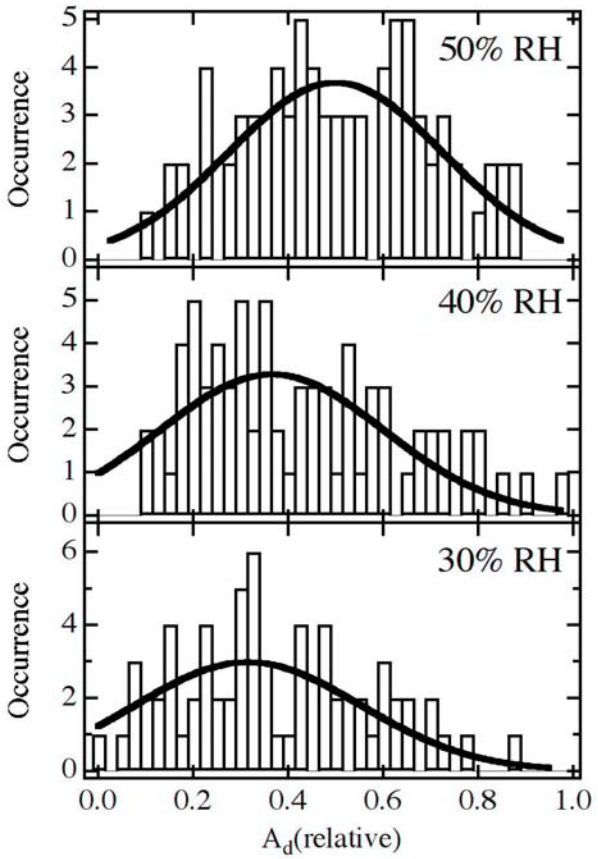


**Figure 3.9**. Histograms showing the distribution of measured $A_d$(relative) values for DiI-doped as-synthesized mesoporous silica films characterized at 50% RH, 40% RH and 30% RH. The solid lines depict the Gaussian fits to each histogram used to determine the peak of the distribution.

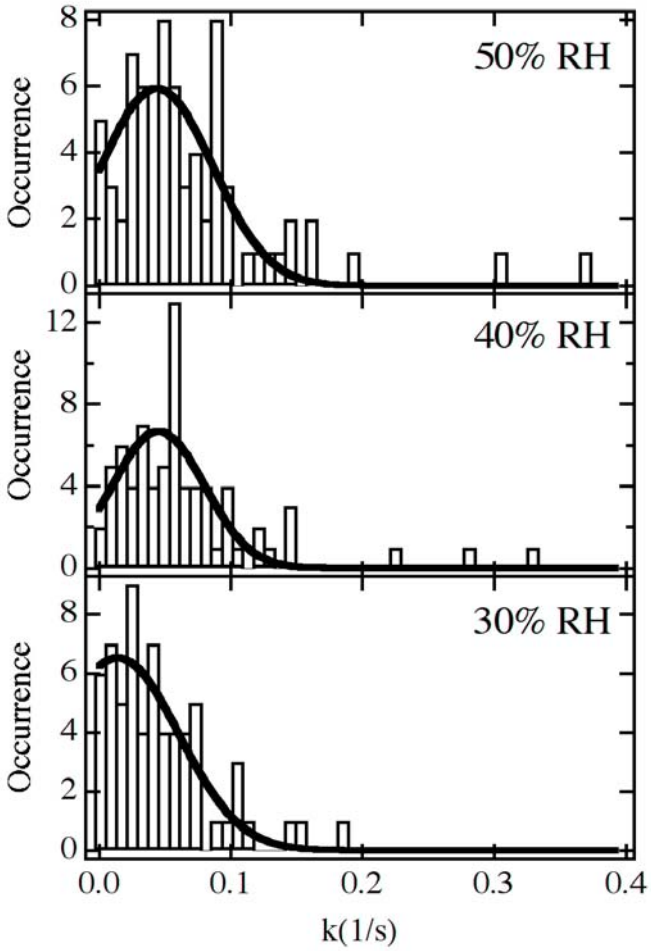


**Figure 3.10**. Histograms showing the distribution of measured k values for DiI-doped as-synthesized mesoporous silica films characterized at 50% RH, 40% RH and 30% RH. The solid lines depict the Gaussian fits to each histogram used to determine the peak of the distribution.

The differences between average and most common D values reported above result from "tailing" of the distributions to higher D values (see especially Figure 3.8, 30% RH), which biases the average results. The observation of these higher D values reflects sample inhomogeneity. Differences in film properties may depend on depth, with more open pores near the film surface allowing for most rapid diffusion. They may also reflect variations in the water content of individual pores throughout the films. Unfortunately it is not possible to determine the exact origins of this heterogeneity at present.

DiI also exhibits evidence of both diffusion and reversible surface adsorption (i.e. as in Figure 3.7C) in the time transients obtained from as-synthesized films. This behavior is strongly dependent on film hydration. As might be expected, the relative contributions of diffusing species increases as the humidity is increased. Figure 3.9 plots histograms of the values obtained. Average $A_d$ values of 0.37, 0.44 and 0.51 were determined from these data for 30, 40 and 50% RH, respectively. Similarly, the average duration of DiI adsorption events become shorter with increasing hydration. Figure 3.10 plots histograms of the average k values obtained, yielding average adsorption times (1/k) of 17 s, 14 s, and 10 s at 30, 40 and 50% RH, respectively. The most common values for these parameters are again observed to be different from the mean values due to sample heterogeneity. The results are consistent with increasing solvation of the dye molecules and dissociation of ionic molecule-matrix complexes under high humidity conditions.

It is unlikely that differences in the sizes of the dye molecules employed play a significant role in governing the above behavior. XRD data indicate the average pore diameter in these materials is ≈ 35-37 Å. All three molecules are smaller than the average pore size and therefore are expected to readily enter most pores. Furthermore, it has also been shown that

interfacial interactions are more important than pore size in determining molecular mobility in monolithic mesoporous materials.[77]

## 3.6 As-synthesized SDS-Containing Mesoporous Silica Films.

To confirm the importance of ionic interactions between the dyes, surfactant and the silica surface, as synthesized films containing SDS were also prepared and implemented in FCS studies of NR, DiI and SPDI mobility. SDS is an anionic surfactant and gives rise to films of lamellar structure, as deduced by small angle X-ray scattering.[141]

Time transients obtained from NR-doped samples again show that the molecules move freely in both dry (20% RH) and hydrated (50% RH) films, yielding average D values of 23.4 x $10^{-11}$ $cm^2/s$ and 27.6 x $10^{-11}$ $cm^2/s$, respectively. The similarities in NR mobility for CTAB and SDS-containing materials provide strong support for the conclusion that hydrogen bonding interactions with the silica matrix and hydrophobic interactions with the micelles are most important in governing its mobility.

Unlike in the CTAB-containing films, SPDI is mobile in the SDS-containing films. Its mobility is strongly dependent on the level of film hydration, yielding average D values of 6 x $10^{-11}$ $cm^2/s$ and 43 x $10^{-11}$ $cm^2/s$ in dry (20% RH) and hydrated (50% RH) films, respectively. The dramatically enhanced mobility of SPDI in the SDS-containing films provides support for the conclusion that its immobility in the CTAB-containing materials results from strong ionic interactions with the surfactant. No such interactions occur between SPDI and SDS, both of which are anionic. These results are consistent with the interpretations of previous bulk studies in which similarly-charged dyes and surfactant species were concluded to repel each other.[158]

DiI is only observed to be mobile in the most highly hydrated SDS-containing films (i.e., at 50% RH). A D value of 30.2 x $10^{-11}$ $cm^2/s$ is obtained under these conditions. In contrast, DiI

was observed to be mobile under relatively low humidities (30% RH) in CTAB-containing films. The reduced mobility of DiI in the SDS films is likely due to relatively strong interactions between the anionic SDS head groups and the cationic DiI molecules. In highly hydrated films, these ionic interactions are disrupted by solvation and the molecules become mobile. These results also suggest that the ionic interactions between DiI and SDS are not as strong as those between SPDI and CTAB. This difference may be due to delocalization of the positive charge on DiI (see Figure 3.3) and the presence of two, localized negative charges on SPDI.

## 3.7 Calcined Mesoporous Silica Films.

Characterization of calcined films provides a means to further explore the mechanisms for dye diffusion and surface adsorption in surfactant-free mesoporous silica films. All studies on calcined films described here were conducted using samples prepared from CTAB-templated sols. When calcined, the structure of CTAB-containing films contracts by 30% and becomes more disordered, but otherwise maintains its hexagonal structure.[179] The average pore size in these materials was found to be 24 Å, from XRD data. Due to film disorder, pores as large as 30 Å were also found to be present. As in the as-synthesized materials, all three dyes are small enough to enter these pores. In contrast to the CTAB-containing materials, the lamellar SDS-containing films collapsed upon calcination,[54,141] and therefore could not be used.

Aside from the change in pore size and order mentioned above, calcination also has a direct impact on film composition. Not only is the surfactant removed from the mesopores, but calcination also yields markedly drier films. Furthermore, the number of surface silanol groups is also reduced and the number of Si-O-Si bonds is increased. Nevertheless, the presence of residual surface silanols and trace amounts of water is reflected by the presence of small absorption peaks observed at 3743 $cm^{-1}$ (sharp, free Si-OH) and 3598 $cm^{-1}$ (broad, hydrogen-

bonded Si-OH) in FTIR spectra of calcined films prepared on silicon substrates.[55,180] The broad, relatively strong absorption of bulk water (3265 $cm^{-1}$) seen in the as-synthesized samples is no longer present. As will be shown below, the water remaining in the calcined films is too little to facilitate molecular diffusion, while the residual surface silanols are still sufficient to impact molecular mobility and surface adsorption in hydrated calcined films.

All three dyes are observed to be immobile (i.e. they exhibit clear, irreversible photobleaching events) in dry (20% RH) calcined films. Immobility in these samples likely arises from strong dye-matrix interactions that occur in the absence of solvent (water). This observation also demonstrates the importance of the hydrated surfactant micelles in facilitating molecular mobility in the as-synthesized samples.

For the rehydrated (50% RH) calcined samples, all three dyes are found to be mobile. Figure 3.11 depicts a bar-graph showing the average D, $A_d$, and adsorption time (1/k) values obtained. For SPDI, DiI and NR, average diffusion coefficients of $40\times10^{-11}$ $cm^2/s$, $31\times10^{-11}$ $cm^2/s$ and $29\times10^{-11}$ $cm^2/s$, respectively, were obtained. The mean $A_d$ values measured for these three dyes were 0.58, 0.56 and 0.53, while their mean adsorption times (1/k) were 13 s, 19 s and 21 s, respectively. Heterogeneity similar to that observed in the as-synthesized films is also observed here, as reflected by the differences between the mean and most common values of these parameters. Overall, the results show that the SPDI molecules are the most mobile of the three and spend the least time adsorbed to the silica surface. DiI and NR exhibit smaller (and similar) diffusion coefficients and spend relatively more time adsorbed to the silica surface.

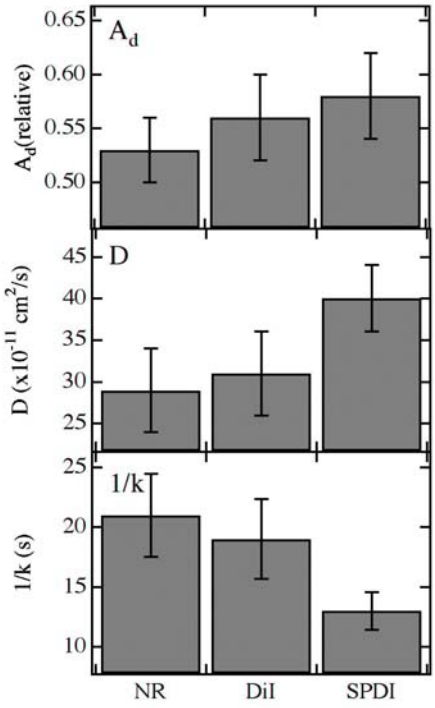


**Figure 3.11**. The measured mean $A_d$(relative) (top), D (middle) and 1/k (mean adsorption time) (bottom) values for the three different dyes in rehydrated (50% RH) calcined mesoporous silica films. Error bars show the 95% confidence interval on each parameter.

The "water-filled" pores of the hydrated calcined films clearly provide the fluid environment necessary for translational diffusion of the dye molecules. The variations in the diffusion coefficients for the three dyes may reflect subtle differences in their mobilities, due to differences in their structures and hence their abilities to fit within pores of somewhat variable geometry (as reflected by film disordering upon calcination). However, the D values obtained (Figure 3.11) do not follow a clear size-dependent trend. SPDI is most mobile, while NR is least mobile. While molecular size may play some role in governing molecular mobility, it is clearly not the dominant factor and other mechanisms must be considered.

It is also likely that ionic interactions play a significant role, especially in the differences observed between SPDI and the other two dyes. Anionic SPDI will tend to avoid the negatively

charged silica surface, spending the majority of its time in central pore regions. Because of its negative charge, SPDI may even be excluded from the smallest pores found in these films.[181] It may therefore be concluded that SPDI probes film environments that are different (and perhaps more like bulk solvent phases) than are probed by DiI and NR. These latter two dyes are expected to spend more time near the pore surfaces and diffusing through smaller pores, leading to lower overall D values. The importance of surface interactions in these results is also supported by the $A_d$ and k values obtained from the three dyes. NR and DiI spend the longest time (on average) adsorbed to the silica surface, and also most frequently exhibit reversible adsorption events.

Comparisons of the results obtained in as-synthesized films to those from calcined films may also be drawn from the data presented herein. While these comparisons are made difficult by the dramatic sample-dependent differences in composition, solvent content and pore size, some of the observed behaviors are interesting and worth noting. For both DiI-and NR-doped samples, surface adsorption times were observed to be significantly longer in the hydrated calcined films than in the as-synthesized films. Similarly, dye diffusion was also slightly faster in the calcined films. While the exact origins of these observations are unknown, they may reflect interactions of the dye molecules with the surfactant phase in the as-synthesized materials. The surfactant phase likely provides a solvating medium, preventing long-term surface adsorption while also providing a (more viscous) medium through which the molecules can diffuse. Once the surfactant has been removed, the molecules spend more time adsorbed to the surface and diffuse more rapidly through the less viscous medium of water-filled (albeit smaller) pores. Figure 3.12 shows a model for diffusion and adsorption of Nile Red within the as-synthesized and rehydrated calcined films.

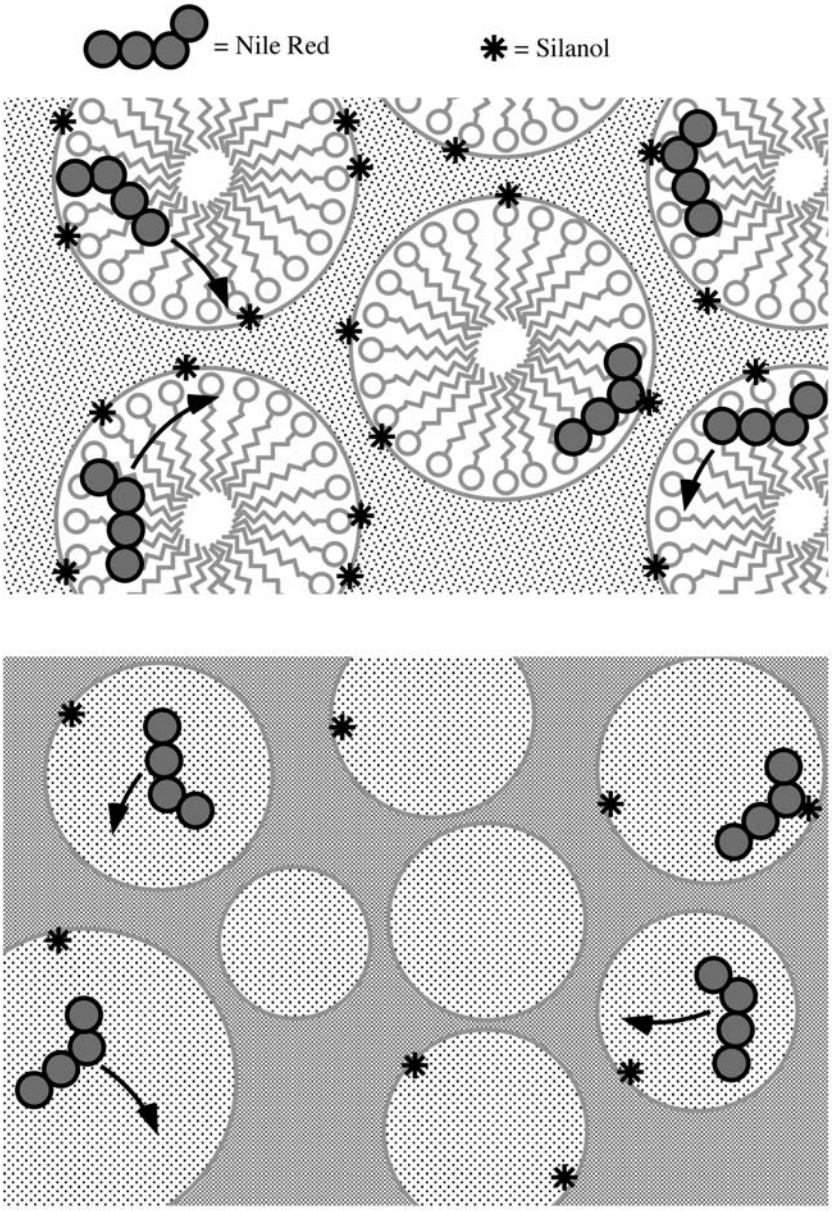


**Figure 3.12**. Model for diffusion and adsorption of Nile Red within the as-synthesized (top) and rehydrated calcined (bottom) films. The dye moves relatively freely through the surfactant-filled and/or hydrated pores, periodically encountering surface silanols (stars) on the silica pore surfaces to which it can hydrogen bond, leading to reversible adsorption events.

## 3.8 Conclusions

Single molecule imaging and fluorescence correlation spectroscopy have been employed to probe single molecule diffusion and surface adsorption in as-synthesized (i.e. surfactant-containing) mesoporous silica thin films and in calcined, plasma-treated mesoporous films. Both dry and rehydrated as-synthesized and calcined samples were investigated. The results of these studies provide valuable information on the rates of mass transport and surface adsorption events of most relevance to applications of these and other mesoporous materials in chemical separations, sensing and optical device applications. Important new information on mass transport and molecule-matrix interactions in mesoporous thin-film systems has been obtained using single molecule spectroscopic methods. Three different dyes of varying size, charge, and hydrophilicity were used. Neutral NR molecules were found to be highly mobile in surfactant-containing films, regardless of the level of film hydration (as controlled by the ambient RH), while also showing strong evidence for reversible adsorption to the silica surface. It was concluded NR spends much of its time diffusing through the nonpolar, hydrated regions of the surfactant micelles, but also comes in periodic contact with the silica surface, to which it can reversibly bind. In contrast, anionic SPDI molecules were found to be immobile under all conditions studied in CTAB-containing films, due to extremely strong ionic interactions between SPDI and the oppositely charged surfactant. Finally, cationic DiI molecules were found to exhibit dramatic humidity-dependent mobilities and also showed evidence for reversible surface adsorption. DiI was concluded to be incorporated in the surfactant micelles and to form strong ionic bonds with the negatively charged silica surface. Studies performed in SDS-containing films provided further support for these conclusions. Overall, results from the surfactant-containing films are consistent with those of previous studies in which molecule-matrix

interactions were probed by bulk-spectroscopic means.[140,157,158] Unlike these previous studies, however, the present results also provide relevant new information on mass transport through the films, evidence of reversible surface adsorption, and quantitative information on variations in these phenomena with film hydration.

# CHAPTER 4 - Molecular Orientation and its Influence on Autocorrelation Amplitudes in Single Molecule Imaging Experiments

This chapter has been published in *Analytical Chemistry*:

Fangmao Ye, Maryanne M. Collinson* and Daniel A. Higgins* "Molecular Orientation and its Influence on Autocorrelation Amplitudes in Single Molecule Imaging Experiments", *Anal. Chem.* **2007**, *79*, 6465.

## 4.1 Introduction

Autocorrelation functions derived from temporally or spatially fluctuating fluorescence signals[40,86] are now widely applied in studies of biomolecule dynamics,[119,182-185] Brownian motion,[44,45,55,57,61,92,160,164,175,186] reversible surface adsorption,[44,45,55,57,61,164] molecular reorientation,[187-189] and other phenomena.[169,175,190,191] The autocorrelation data obtained provides valuable information on the characteristic time scales or distances over which the signal fluctuations occur. Such information is derived from the "rate" at which the autocorrelation function decays. Importantly, the concentration of a species of interest can also be obtained from the amplitude of autocorrelation decay data. In early work, Koppel[179] and Elson and Magde[86] showed that under background-free conditions, the amplitude of the autocorrelation function scales as the inverse of the average concentration of objects in the detection volume. A more complicated concentration dependence arises in the presence of background.[179] Autocorrelation methods have since been widely employed for determining concentrations (or relative concentrations) of protein aggregates,[192,193] cell receptors[176,194] and cytosolic proteins,[195] and fluorescent microspheres.[195] The concentration dependence of autocorrelation amplitudes obtained in single molecule studies of diffusion in solution,[196,197] near surfaces,[164] and in thin films[55,57,61,92] has also been discussed.

Implicit in much of the previous work referenced above is the assumption that the individual objects being detected exhibit no polarization dependence in either their excitation or emission processes. Entirely different results are obtained when the objects absorb or emit polarized light. The former assumption is valid when the objects being detected are stained at relatively high concentrations (i.e., as in the case of fluorescent spheres[195,198]) so that the dye molecules themselves do not individually contribute to the signal fluctuations. It is also valid in

solution-phase single molecule studies of free diffusion in which the molecules rapidly and randomly reorient on the relevant experimental time scale (i.e., the signal averaging time). Situations in which this assumption is not valid include solution-phase experiments like those described by Aragón and Pecora,[199] in which the molecules being probed reorient relatively slowly. In this case, the polarization sensitivity of the optical system must be taken into account to properly relate the autocorrelation amplitude to the concentration of diffusing species.

Several single molecule studies reported in the recent literature provide additional examples of situations in which the polarization sensitivity of the optical system must be accounted for when interpreting autocorrelation decay amplitudes. Included are all single molecule imaging studies in which the single molecules being detected are adsorbed or entrapped in or on thin-film materials in fixed orientations.[55,57,92,199] Additional examples include studies of single molecule diffusion in organically modified silica films,[92,199] single molecule diffusion and surface interactions in mesoporous silica materials,[55,57,61,66,90,160] and studies of solution-phase diffusion coupled with reversible molecular adsorption at chemically-modified silica surfaces.[43-45,164,200] In many of these latter reports, the single molecules exhibit either permanent or reversible molecular adsorption in (or on) the materials of interest. Hence, the molecules are expected to remain in fixed orientations for relatively long periods of time. It should be noted that use of unpolarized or circularly polarized light for excitation and detection purposes does not yield the result expected for rapidly reorienting molecules. The optical systems (i.e. microscopes) used in all such studies exhibit sufficient polarization sensitivity to yield altogether different results.

In this chapter, the full concentration dependence of the autocorrelation amplitude in the presence of orientationally-fixed single molecules is presented. Derivation of the proper

expression, taking into account both polarization-dependent excitation and emission phenomena, relies on a combination of concepts from several previously published models.[86,179,199,201,202] Both simulated and experimental data are then used to conclusively demonstrate the applicability of this model in the analysis of single molecule image autocorrelation data. The experimental data employed in this analysis was obtained from dry dye-doped mesoporous silica films.[55] To help demonstrate the importance of orientation phenomena in determining autocorrelation amplitudes, the single molecule imaging results are also compared to simulated and experimental results from rapidly diffusing and reorienting molecules. Data obtained from hydrated mesoporous silica thin films are used to demonstrate the lack of orientation sensitivity in this case,[55] for which the well-known[179] dependence on concentration and background alone is recovered. The conclusions drawn are of relevance to any correlation spectroscopy experiments in which there is potential for orientation/polarization sensitivity (e.g., temporal or spatial, single molecule or otherwise).

## 4.2 Experimental Section

### *4.2.1 Sample Preparation.*

Calcined mesoporous silica films were prepared as described previously.[55] Briefly, silica sols were obtained by mixing tetramethoxysilane (TMOS), water, absolute ethanol and HCl in a small vial and stirring for 1 h. After 24 h, the sol was doped with cetyltrimethylammonium bromide (CTAB) and stirred for 1 h. The final molar ratio for the composite was typically 1:5.6:8:0.003:0.2 (TMOS:$H_2O$:Ethanol:HCl:CTAB). A small aliquot (65 μL) of the sol was then spin cast (30s at 6000 RPM) onto a clean glass coverslip (Fisher Premium). The film was subsequently dried overnight at room temperature in a desiccator and calcined in a furnace. During calcination, the films were first heated at 160$^{o}$C for 90 min. The temperature was then

increased to 350°C at a rate of 1°C/min and was held there for 5 h. After calcination, the films were treated for 2-3 min in an air plasma to remove residual luminescent impurities. Small angle X-ray scattering results show the mesopores in these films take on a collapsed, hexagonal organization of modest order.[55] Film thickness was determined to be ≈ 400±30 nm, by profilometry.

All fluorescence images and time transients were recorded using films that had been loaded with DiI (1,1'-dihexadecyl-3,3,3',3'-tetramethylindocarbocyanine perchlorate, Invitrogen) after calcination and plasma treatment. Loading was achieved by soaking the calcined/plasma treated slides in a dilute methanolic solution of DiI for 1 h. A series of dye concentrations was employed to obtain films incorporating different amounts of dye. The specific dye concentrations used in individual experiments are defined below. After loading of the films, excess dye was removed by rinsing with ethanol. The dye-loaded films were subsequently dried in a desiccator overnight before use.

Both "dry" and "hydrated" samples were employed. Films classified as "dry" were maintained in dry air (20% relative humidity, RH) during storage and imaging. "Hydrated" films were stored at 50% RH for ≈ 12 h prior to use, and were studied under these same conditions. As we have shown in the Chapter 3, high RH conditions result in hydration of the film and a dramatic increase in dye mobility.

### *4.2.2 Instrumentation.*

All studies were conducted on a sample scanning confocal microscope shown in Figure 2.4 in Chapter 2. Briefly, this system is built upon an inverted epi-illumination microscope. A "closed-loop" X,Y stage was employed for sample positioning and imaging. Light from a green helium-neon laser (543.5 nm) was used to excite DiI in all experiments. Prior to incidence on

the sample, the laser light was first passed through appropriate bandpass filters and polarization optics. Linearly polarized laser light thus produced was subsequently reflected from a dichroic beamsplitter into the back aperture of an oil immersion objective (1.3 numerical aperture, NA). This objective was used both for focusing the excitation light into the sample and for collecting the resulting sample fluorescence. A nearly diffraction limited focus of ≈ 300 nm $1/e^2$ radius was produced in the sample. The incident power at the sample was estimated to be less than 200 nW in all experiments. Fluorescence collected from the sample was isolated from residual excitation light by passage back through the dichroic beamsplitter, a holographic notch filter, and a bandpass filter. A single photon counting avalanche photodiode was used as the detector. Total (i.e. unpolarized) fluorescence was detected. Pulses from the detector were counted using a National Instruments counter-timer card (PCI-6602).

Fluorescence images of dry samples were acquired by raster scanning the sample above the focused laser spot. The fluorescence signal was integrated for 40 ms at each pixel in the 100×100 pixel images. Single-point fluorescence time transients were obtained from hydrated samples by positioning selected sample regions in the laser focus and recording the spectrally integrated fluorescence in time. Individual transients were up to 3 h in length, with a dwell time of 80 ms.

## 4.3 Results and Discussion

### *4.3.1 Description of the Model.*

The derivation of the autocorrelation function for polarization-independent excitation and emission of single particles has been reported previously.[86,179] The dependence on several parameters, including concentration, is demonstrated in these derivations, for conditions under which either the fluorescence signal[86] or background[179] dominate. Likewise, the autocorrelation

function expected for polarization-dependent excitation and emission of molecules exhibiting rotational and translational diffusion in solution has been reported.[199] Here, a modified derivation, demonstrating the dependence on molecular orientation, experimental configuration and concentration for orientationally-fixed molecules in single molecule imaging experiments is given. This model is also applicable to interpretation of temporal single molecule autocorrelation data in situations where the molecules repeatedly and reversibly adsorb to materials surfaces[43-45,55,57,200,203] in fixed orientations.

Here, the sample fluorescence in the image plane is defined as i(x,y). Fluorescence images recorded at sufficiently low concentrations exhibit signal fluctuations due to Poisson-distributed variations in the number of molecules present in the detection volume. The relative mean square fluctuations observed in such images are given by:

$$\frac{\left\langle \left(\delta i(x,y)\right)^2 \right\rangle}{\left\langle i(x,y)\right\rangle^2} = \frac{\left\langle \left(i(x,y) - \left\langle i(x,y)\right\rangle\right)^2 \right\rangle}{\left\langle i(x,y)\right\rangle^2} \tag{4.1}$$

where, the brackets ($\langle\ \rangle$) indicate that the average over the entire image is taken.

The value obtained from Eqn. 4.1 yields the amplitude of the autocorrelation decay required for concentration determinations.[86] However, its value incorporates significant contributions from uncorrelated fluctuations (i.e. Poisson distributed shot noise and unresolved dynamics, such as might arise from triplet blinking[174]). The shot noise contributions to Eqn. 4.1 may often be removed by subtracting $1/\langle i(x,y)\rangle$ from its value.[191] Unfortunately, fluctuations due to other processes cannot readily be subtracted. Therefore, the autocorrelation amplitude is best obtained from the full autocorrelation function, $G(\xi,\psi)$:

$$G(\xi,\psi)=\frac{\langle(\delta i(x+\xi,y+\psi))(\delta i(x,y))\rangle}{\langle i(x,y)\rangle^2}=\frac{\langle(i(x+\xi,y+\psi)i(x,y))\rangle}{\langle i(x,y)\rangle^2}-1 \qquad (4.2)$$

where $G(\xi,\psi)$ describes the relative mean square fluctuations as a function of position $\xi,\psi$ in the image. Note that Eqn. 4.2 reduces to Eqn. 4.1 when $\xi,\psi = 0$. By curve fitting the experimentally determined $G(\xi,\psi)$ (for $\xi,\psi > 0$) to an appropriate expression, a good estimate of the autocorrelation amplitude, G(0,0), can be obtained. G(0,0) can then be related to the average concentration of a single analyte species present in the detection volume.[86,179]

The dependence of the numerator and denominator in Eqns. 4.1 and 4.2 on concentration, molecular orientation and excitation/detection parameters are given in the following sections.

*Average Signal* $\langle i(x,y)\rangle$. The signal from the detection volume, for molecules in fixed orientations defined by the usual angles $\phi,\theta$ in spherical polar coordinates is given as:

$$i(\phi,\theta)=PK(\phi,\theta)VC(\phi,\theta)+PVB \qquad (4.3)$$

The x,y coordinates have been suppressed in Eqn. 4.3 to simplify the expression. Here, P is the incident power in photons/sec, V is the detection volume, $K(\phi,\theta)$ describes the orientation-dependent (and position dependent) excitation and detection efficiency, $C(\phi,\theta)$ describes the number density (or concentration) of molecules at a particular orientation, and B is the background per unit volume. The latter may arise from elastic and/or inelastic scattering from the sample matrix.[40]

The orientation dependence of K results from the interaction of the polarized incident optical fields with the (fixed) transition dipoles of the molecules. Contributions to this term also arise from the emission-angle-dependent and polarization-dependent collection efficiency of the high NA objective most often used in single molecule experiments.[201,202] Lastly, the position

dependence of K arises from the Gaussian intensity profile of the focused incident light. For single molecule detection with linearly-polarized incident light and unpolarized emission detection, $K(\phi,\theta)$ may be written as:

$$K(\phi,\theta) = K'\left|\hat{\mu}(\phi,\theta)\cdot\hat{E}_{inc}\right|^2 F_{exc}F_{det}(\phi,\theta) \tag{4.4}$$

In Eqn. 4.4, K' represents the peak orientation- and position-independent excitation and detection efficiency, $\hat{\mu}(\phi,\theta)$ the molecular transition dipole, $\hat{E}_{inc}$ the incident optical field, $F_{exc}$ the position-dependent excitation efficiency in the microscope, and $F_{det}(\phi,\theta)$ the orientation dependent detection efficiency. The dependence of these variables on various experimental parameters is outlined below. Specifically, K' includes terms like the excitation cross-section of the molecule, the quantum efficiency of emission and detection, etc. $F_{exc}$ is readily replaced by its average value, which for a Gaussian intensity profile in the microscope focus is simply half its peak value (i.e, $F_{exc} = 0.5$).

The second term in Eqn. 4.4 (incorporating $\hat{\mu}(\phi,\theta)$ and $\hat{E}_{inc}$) describes part of the orientation dependence of K. Here, $\hat{\mu}(\phi,\theta)$ and $\hat{E}_{inc}$, both of unit magnitude, are defined as:

$$\hat{\mu}(\phi,\theta) = \begin{pmatrix} \sin\theta\cos\phi \\ \sin\theta\sin\phi \\ \cos\theta \end{pmatrix},\ \hat{E}_{inc} = \begin{pmatrix} 1 \\ 0 \\ 0 \end{pmatrix} \tag{4.5a,b}$$

The nonzero z-component (along the optical axis) of the incident field has been neglected (Eqn. 4.5b) as it is typically small compared to the lateral field components.[202]

The orientation dependent detection efficiency in Eqn. 4.4 is given by $F_{det}(\phi,\theta)$ and results from variations in the efficiency at which light is collected by the high NA objective, for a

given transition dipole orientation. Employing the results of Axelrod[201] and Ha, et al.,[202] $F_{det}(\phi,\theta)$ is given by:

$$F_{det}(\phi,\theta) = 1 + \left(\frac{2K_3}{K_1} - 1\right)\cos^2\theta \tag{4.6}$$

for which $K_1$ and $K_3$ are defined by the angular range, $\theta_{obj}$, over which the objective collects light:

$$\begin{aligned} K_1 &= 3/32\left(5 - 3\cos\theta_{obj} - \cos^2\theta_{obj} - \cos^3\theta_{obj}\right) \\ K_3 &= 1/8\left(2 - 3\cos\theta_{obj} + \cos^3\theta_{obj}\right) \end{aligned} \tag{4.7a,b}$$

For the 1.3 NA objective used in these studies (with immersion oil having n=1.52), $\theta_{obj} = 58.8^o$, $K_1 = 0.285$ and $K_3 = 0.0731$. Inserting these parameters into Eqn. 4.6 yields $F_{det}(\theta,\phi) \approx 1\text{-}0.5\cos^2\theta$.

Lastly, for implementation of Eqn. 4.3, the proper form for $C(\phi,\theta)$ must be determined. The molecular orientation distribution in the film must be taken into account in defining $C(\phi,\theta)$, yielding:

$$C(\phi,\theta) = \overline{C} f(\phi,\theta)\sin\theta \tag{4.8}$$

Here, $\overline{C}$ is the mean number density of molecules in the film as has been used in previous derivations.[86,179,192] For the purposes of the present experiments, it is assumed that the molecules take on random orientations (i.e., $f(\phi,\theta) = 1$) in the film. As a result $C(\phi,\theta) = \overline{C}\sin\theta$.

Inserting the above expressions into Eqn. 4.3 yields the total orientation-dependent signal plus background:

$$i(\phi,\theta) = \frac{1}{2}PK'V\overline{C}\cos^2\phi\left(1 - 0.5\cos^2\theta\right)\sin^3\theta + PVB \tag{4.9}$$

Taking the *average* signal from all molecules over all possible orientations in an image yields:

$$\langle i(x,y)\rangle = \frac{PK'V\overline{C}}{8\pi}\int_0^{2\pi}\cos^2\phi d\phi\int_0^{\pi}\left(1-0.5\cos^2\theta\right)\sin^3\theta d\theta + PVB \qquad (4.10)$$

Under the present experimental conditions, Eqn. 4.10 becomes $\langle i(x,y)\rangle = 0.15PK'V\overline{C} + PVB$.

*Signal Fluctuations* $(\delta i(x,y))^2$. The signal fluctuations are defined in a manner similar to the average signal (Eqn. 4.3), with the important exception that there is no contribution from background counts. Here, the squared signal fluctuations are given by:

$$(\delta i(\phi,\theta))^2 = P^2K^2(\phi,\theta)VC(\phi,\theta) \qquad (4.11)$$

Since the number of molecules in the detection volume is Poisson distributed, the squared signal fluctuations scale linearly with the number density of molecules. Using the same definitions of parameters given above, the mean square fluctuations obtained by averaging over all molecules and orientations is given by:

$$\left\langle(\delta i(x,y))^2\right\rangle = \frac{(PK')^2V\overline{C}}{16\pi}\int_0^{2\pi}\cos^4\phi d\phi\int_0^{\pi}\left(1-0.5\cos^2\theta\right)^2\sin^5\theta d\theta \qquad (4.12)$$

which becomes $\left\langle(\delta i(x,y))^2\right\rangle = 0.043(PK')^2V\overline{C}$ under the present conditions.

*Autocorrelation Amplitude G(0,0).* By combining Eqns. 4.10, 4.12 and 4.1 or 4.2, the autocorrelation amplitude expected as a function of number density for single molecules found in *fixed*, but random, orientations is then given by:

$$G(0,0) = \frac{0.043(K')^2\overline{C}}{V\left(0.023(K')^2\overline{C}^2 + 0.30K'\overline{C}B + B^2\right)} \qquad (4.13)$$

In the presence of a nonzero background, the autocorrelation amplitude does not exhibit a simple dependence on analyte concentration.[179] Rather, the amplitude initially rises, passes

through a maximum and then falls with increasing concentration. The general form of this expression is similar to that given originally by Koppel.[179] However, the amplitude predicted at a given concentration differs because of the orientation-dependent phenomena mentioned above. The maximum in a plot of amplitude vs. number density occurs at $\overline{C}_{max}$ = B/(0.15K') and the maximum autocorrelation amplitude at $\overline{C}_{max}$ for fixed molecules is predicted to be:

$$G(0,0)_{max} = \frac{0.29K'}{4VB} \tag{4.14}$$

Eqns. 4.13, 4.14 demonstrate that when the molecules being detected are found in *fixed* orientations, the signal fluctuations observed are expected to be greater than those from samples exhibiting polarization-*independent* excitation and emission. Under the latter condition, the orientation-dependent factor in the numerator of Eqn. 4.13 (defining the signal fluctuations) changes from 0.043 to 0.023. The autocorrelation amplitude in the case of orientationally-fixed molecules is thus 0.043/0.023 = 1.9 times larger (at all concentrations) than for rapidly reorienting molecules, using parameters common for single molecule experiments (defined above.)

Autocorrelation data taken from both simulated and experimental images and time transients are used below to verify the concentration dependence in Eqn. 4.13 and to demonstrate the differences in autocorrelation data obtained from fixed and rapidly reorienting single molecules.

### *4.3.2 Simulated Images.*

Simulated images were generated by modeling the sample as a 30 X 30 $\mu m^2$ two-dimensional (2D) region. Single molecules were positioned at random sites within the region and were held at these locations throughout the simulations. The number of molecules in the

entire 30 X 30 $\mu m^2$ region was varied from 10 to 40000 ($\overline{C}$ = 0.011 to 44 $\mu m^{-2}$) for the full range of simulations performed. The orientations of the individual molecules were also determined at the start of each simulation and were held fixed throughout. The molecules were assigned a random orientation in the plane of the sample (i.e. in $\phi$). The out-of-plane orientation $\theta$ for each was determined by assuming a random distribution in $\sin\theta$.

In generating the simulated images, a Gaussian excitation profile was "scanned" across the central 10 X 10 $\mu m^2$ region to mimic the recording of actual image data. The Gaussian profile had a variance ($s^2$) of $2.6 \times 10^{-10}$ $cm^2$, as determined from experimental images (see below).[57] The incident light was taken to be linearly polarized along $\phi = 0^o$. The peak signal from each molecule (PK') was assigned a value of 200 counts, while the background count rate (PVB) was set to 20 counts. Gaussian noise having a variance equal to the total counts at each pixel was added to simulate shot noise.

Figure 4.1A shows a representative example of the simulated images obtained. This image was obtained at a number density of 1.1 molecules/$\mu m^2$. Four such images were generated at each concentration defined above and used in the following analysis. All simulated images were autocorrelated using Eqn. 4.2. The autocorrelations were then fit to a Gaussian function, excluding G(0) from the fit:[92]

$$G(\rho) = A_g \exp\left(-\left(\frac{\rho}{2s}\right)^2\right) \tag{4.15}$$

Here, $A_g$ represents the amplitude of the decay and provides an estimate of G(0), while $\rho$ is the radial dimension in a 2D image autocorrelation. The Gaussian function describes the autocorrelation decay expected from the excitation of *fixed* single molecules by a Gaussian incident beam. An additional component might have been included in Eqn. 4.15 to account for

triplet blinking, photobleaching or other fluctuations.[92] Since the image simulations did not include such phenomena and the experimental image data (see below) did not show significant contributions from these sources, all image autocorrelation data could all be fit well with Eqn. 4.15 alone. Note that only the ten points on either side of the central point ($\rho = 0$) were used to fit the data. Figure 4.1B shows the resulting radial component of the image autocorrelation obtained along the horizontal direction in Figure 4.1A, along with its fit to Eqn. 4.15.

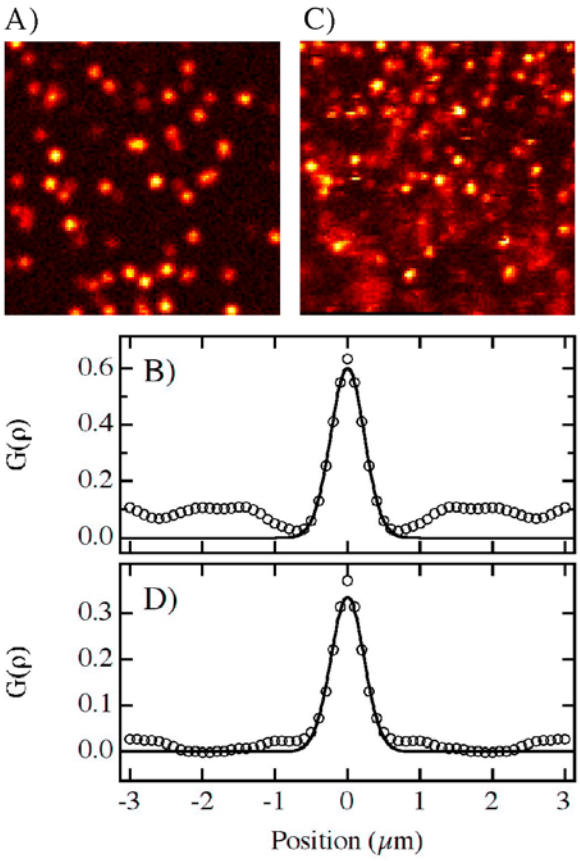


**Figure 4.1.** A) Simulated image for a number density of 1.1 molecules/μm$^2$. B) Autocorrelation along the horizontal direction (open circles) for the image shown in A) and its fit (solid line) to Eqn. 4.15. C) Experimental image (10 X 10 μm$^2$) for 0.9 nM DiI in a dry calcined silica film. D) Autocorrelation along the horizontal direction (open circles) for the image shown in C) and its fit (solid line) to Eqn. 4.15.

Figure 4.2 depicts the autocorrelation amplitude obtained for several simulated images having number densities from $\overline{C}$ = 0.011 to 44 $\mu m^{-2}$. The concentration dependence predicted by Eqn. 4.13 is depicted in these data. The fit shown yielded V = 0.33±0.01 $\mu m^2$, B/K' = 0.31±0.02 $\mu m^{-2}$ and $G(0)_{max}$ = 0.70, consistent with the simulation parameters employed. Input parameters in these simulations include V = $4\pi s^2$ = 0.33 $\mu m^2$, PB = 61 $\mu m^{-2}$ and PK' = 200 (hence, B/K' = 0.31 $\mu m^{-2}$).

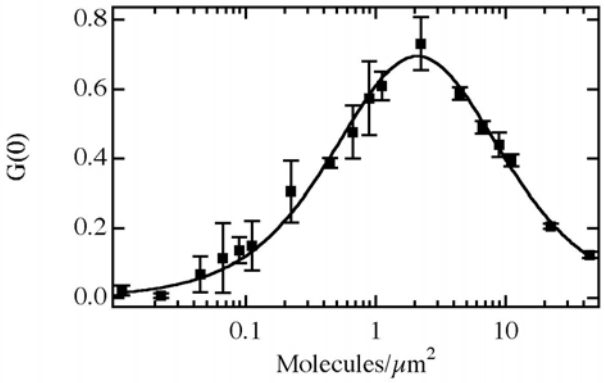


**Figure 4.2**. Concentration dependent autocorrelation amplitude derived from a series of simulated images (filled squares) at the number densities shown. The solid line shows a fit of these data to Eqn. 4.13. Error bars depict the standard deviation of four replicate simulations at each concentration.

### *4.3.3 Simulated Transients.*

Simulated time transients were employed to demonstrate the differences between autocorrelation data obtained from orientationally-fixed molecules and those that are rapidly reorienting. These time transients were obtained in a manner similar to the simulated images, using a 30 X 30 $\mu m^2$ region. Simulations were again performed for a range of number densities ($\overline{C}$ = 0.011 to 44 $\mu m^{-2}$). The single molecules were initially assigned random positions, but were then allowed to move freely throughout the region by taking steps of random size in the sample plane during each simulation time step. The mean square displacement in each direction was

taken as 2Dt, where D is the diffusion coefficient and t is the time step employed. Here, D = $4x10^{-10}$ $cm^2/s$ and t = 0.08 s were used to mimic the parameters of real experiments (see below).[57] The orientation of each molecule was assumed to be randomized on the 0.08 s time scale, making the maximum signal (neglecting shot noise) from each molecule 0.3K'P = 60 counts.

The individual time transients obtained were autocorrelated using the 1D analog to Eqn. 4.2 and were fit to the following expression:

$$G(\tau) = \frac{A_d}{1 + D\tau/s^2} + A_a \exp(-\tau k) \tag{4.16}$$

Only the first 5% (at most) of each autocorrelation was fit, due to the limited signal-to-noise at longer times.[185,204] The first term in Eqn. 4.16 describes the contributions of diffusing species to the autocorrelation decay, while the second describes contributions from a variety of other sources, including spectral diffusion, quantum yield variations,[175] and reversible molecular adsorption.[43,44,200] While such phenomena were not included in the simulations, this second term was included because evidence of these phenomena was found in the experimental data described below.[57] For all simulated data, $A_a$ was set to zero.

Figures 4.3A,B show a representative simulated time transient, its autocorrelation and the fit to Eqn. 4.16. Four transients were generated, autocorrelated and fit in this same manner for each concentration in the range specified above. Figure 4.4 plots the mean amplitude ($A_d$ = G(0)) of the autocorrelation decay at each concentration. The data in Figure 4.4 were fit to the analog of Eqn. 4.13 for freely rotating molecules (i.e. 0.043 in numerator replaced with 0.023). As expected, the amplitude of the time transient autocorrelation data is smaller by a factor of ≈ 1.9 compared to that obtained from simulated images of molecules at fixed orientations. The fit shown yielded V = 0.32±0.01 $\mu m^2$ and B/k = 0.31±0.02 $\mu m^{-2}$. Again, the parameters obtained

from the fit of the simulated time transient data are virtually identical to those input into the simulations (see above).

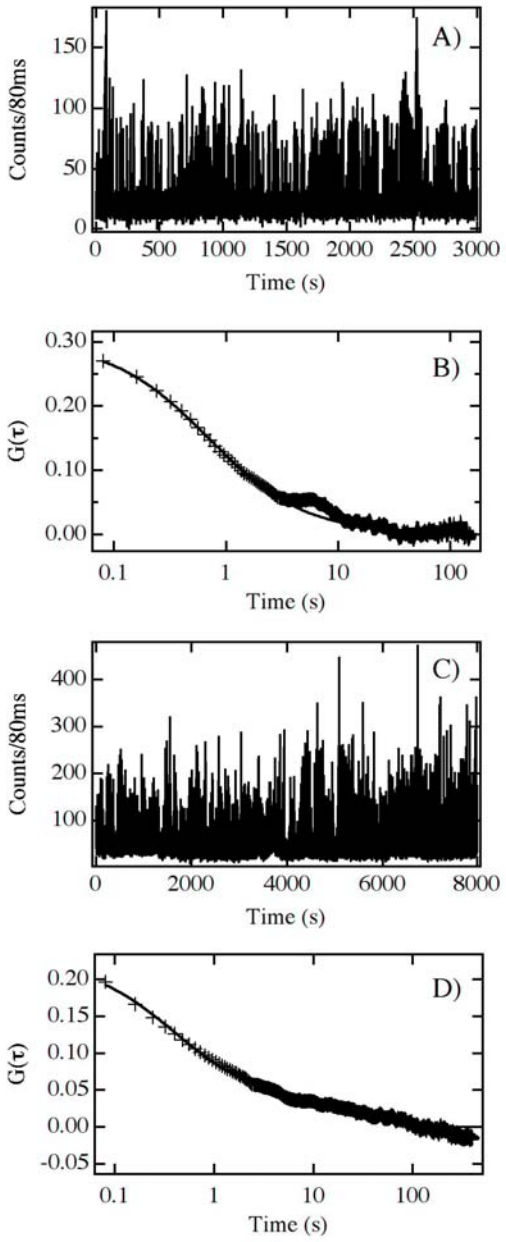


**Figure 4.3**. A) Simulated time transient for a molecular density of 0.67 molecules/$\mu m^2$. B) Autocorrelation (symbols) and fit (solid line) to Eqn. 4.16 for the simulated time transient shown in A). C) Time transient for 1.6 nM DiI in a calcined silica film probed at 50% RH. D) Autocorrelation (symbols) and fit (solid line) for the experimental time transient shown in C).

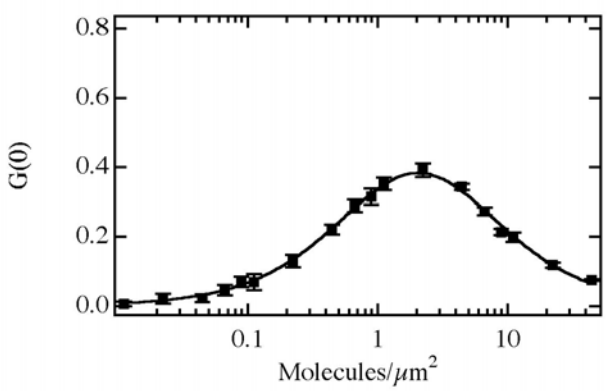


**Figure 4.4.** Concentration dependent autocorrelation amplitude derived from simulated time transients (filled squares) at the number densities shown. The solid line shows a fit of these data to the free-rotation analog of Eqn. 4.13. Error bars (barely visible) depict the standard deviation from four replicate simulations at each concentration. The data are plotted on the same y-scale as Figure 4.2.

### *4.3.4 Experimental Images.*

Autocorrelation data derived from experimental images and time transients provide practical confirmation of the above predictions. Here, images of dry calcined mesoporous silica samples containing low (nanomolar) concentrations of DiI were used to obtain the necessary experimental image data. As we have shown in the Chapter 3, the vast majority of DiI molecules found within mesoporous silica films studied under dry conditions (i.e. 20% relative humidity) are immobile. Permanent (or long-term) adsorption of the molecules in fixed positions is verified by repeatedly imaging the same area while monitoring the positions of the fluorescent spots observed. Verification that the molecules are adsorbed in fixed orientations is obtained by recording time transients for the individual spots under polarized excitation conditions. Molecules that yield invariant emission (aside from shot noise) are concluded to be orientationally-immobile. Adsorption of the molecules at fixed positions and orientations results

from strong ionic interactions between the positively charged DiI and negatively charged silica surface.[57]

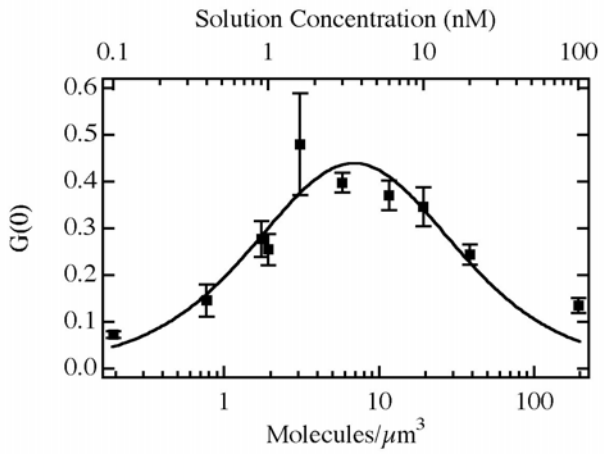


**Figure 4.5.** Concentration dependent autocorrelation amplitude derived from a series of experimental images (filled squares). The solid line shows a fit of these data to Eqn. 4.13. The concentrations on the upper x-axis represent the solution concentrations used to load the films with dye. The number densities shown along the lower x-axis were determined by fitting the data, assuming a detection volume of 0.16 μm$^3$. Error bars depict the standard deviation from three replicate measurements at each concentration.

Figures 4.1C,D show a representative fluorescence image for dry DiI-doped calcined silica films, its autocorrelation along the horizontal direction and its fit to Eqn. 4.15. Again, only a Gaussian model for the autocorrelation decay was employed. Figure 4.5 shows the autocorrelation amplitude obtained from a series of images recorded at different dye concentrations. Three replicate images were recorded at each concentration. The dye concentration in each of the methanolic solutions used to load the films is shown along the upper x-axis in Figure 4.5. DiI concentrations employed were 0.1, 0.4, 0.9, 1.0, 1.6, 3.0, 6.0, 10, 20 and 100 nM. While it is difficult to know the actual number density of dye molecules present in the films from the solution concentration alone, such information can be obtained from the autocorrelation data. To make this determination, the detection volume of the microscope must

be known. This information is available from the average *widths* of image autocorrelations obtained at low concentrations[92] and from the known thickness of the samples. A value of $4\pi s^2 = 0.4 \pm 0.1\ \mu m^2$ is obtained in this case. Using the measured film thickness of ≈ 0.4 μm, the detection volume, V, is found to be 0.16 $\mu m^3$. Assuming the dye concentration in the film scales linearly with the concentration of molecules in the loading solution, a good estimate of the concentration in each film can be determined by fitting the data in Figure 4.5 to Eqn. 4.13, using an adjustable number density.

The number density shown in Figure 4.5 along the lower x-axis depicts the values obtained by the above procedure. The results show that $B/K' = 1.03 \pm 0.05\ \mu m^{-3}$ and that the concentration of image spots is approximately 3-fold greater than expected from the solution concentration alone. An increase in dye concentration in the film (relative to the original solution) might result from strong interactions between the cationic dye and anionic sites on the silica surface.

### *4.3.5 Experimental Transients.*

As predicted, different results are obtained for samples that contain a predominance of freely mobile molecules. DiI doped calcined mesoporous silica films exposed to high relative humidity (50% RH) environments were used in these experiments. Previous studies from our group have shown that the majority of DiI molecules exhibit relatively rapid translational and rotational diffusion under such conditions, yielding average translational diffusion coefficients of $D = 3.1\ (\pm 0.5) \times 10^{-10}\ cm^2/s$.[60] Three time transients were obtained at each concentration, using a bin time of 0.08 s. These time transients were autocorrelated and fit to Eqn. 4.16. Representative data and its autocorrelation are shown in Figure 4.3C,D. Again, only the first ≈ 5% (at most) of each autocorrelation was fit. The first point in each was also excluded from the

fit. Figure 4.6 plots the total autocorrelation decay amplitude ($A_d+A_a$ from Eqn. 4.16 provides the estimate of G(0)) as a function of DiI concentration (upper x-axis) in the methanolic solution used to load the films. As in Figure 4.5, the lower x-axis depicts the number density obtained by fitting the data using V = 0.16 $\mu m^3$. Fitting of these data to the free-rotation analog of Eqn. 4.13 yielded B/K' = 1.16±0.04 $\mu m^{-3}$, with V = 0.16 $\mu m^3$. The similar value obtained for B/K' from the experimental imaging and time transient autocorrelations is expected. This ratio is insensitive to the orientational mobility of the molecules. The concentration of molecules determined by fitting the data (lower x-axis in Figure 4.6) is again greater than in the solutions used to prepare them. In this case, the concentration appears to be a factor of seven greater. The difference in apparent concentrations determined by fitting the image and time transient autocorrelation results (showing three-fold and seven-fold concentration increases, respectively) result in part from significant uncertainties in estimating the detection volume in each case. The large error bars in the time transient data (see below) also contribute to uncertainties in the concentration.

Of most significance to the present work are the *relative* autocorrelation amplitudes obtained from the image and time transient data. As predicted, the amplitudes of the autocorrelation data obtained from the time transients are all smaller than those from the image data. The peak amplitudes of the fits shown in Figures 4.5 and 6 are 0.44 and 0.20, respectively, yielding an amplitude ratio for orientationally fixed vs. reorienting molecules of ≈ 2.2, close to the value of 1.9 predicted above. It should be noted that the amplitude results do not depend upon assumptions of the detection volume and therefore are expected to yield consistent results in situations where the only difference between samples is in the orientational mobility of the molecules.

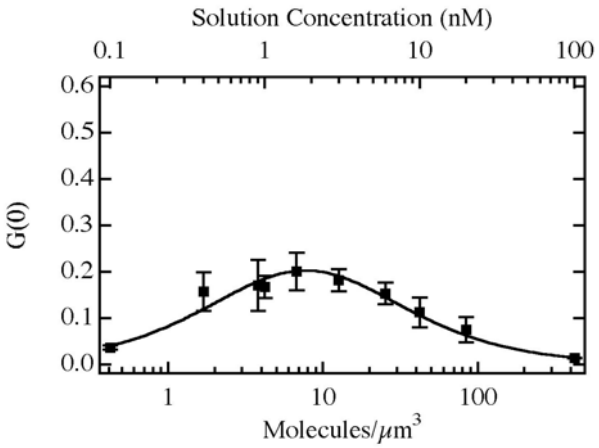


**Figure 4.6.** Concentration dependent autocorrelation amplitude derived from a series of experimental time transients (filled squares). The solid line shows a fit of these data to the free-rotation analog of Eqn. 4.13. The concentrations on the upper x-axis represent the solution concentrations used to load the films with dye. The number densities shown along the lower x-axis were determined by fitting the data, assuming a detection volume of 0.16 $\mu m^3$. Error bars depict the standard deviation from three replicate measurements at each concentration. The data are plotted on the same y-scale as Figure 4.5.

As a final point, it should be noted that the error bars shown in the experimental time transient data are significantly larger than expected from the simulation results (compare Figures 4.4 and 4.6). The error bars in the image autocorrelation data are also expected to be larger than those of the time transient data (compare Figures 4.2, 4.4-6). Measurement errors are expected to scale as the inverse square root of the number of signal fluctuations observed in each image or time transient.[205-208] The number of such fluctuations is directly proportional to the number of data points in each data set. From this argument alone, the time transient data should yield error bars that are significantly smaller, as observed in the simulation data (Figures 4.2 and 4.4). The fact that the error bars are much larger in the experimental time transient data proves that other factors contribute. Possible sources of increased errors include: 1) difficulties in maintaining the microscope focus over the long time periods used in recording the transients, 2) local variations

in film thickness (> 15%) and hence, detection volume and 3) sub-micrometer variations in sample porosity,[67] which might lead to variations in the apparent local concentration.

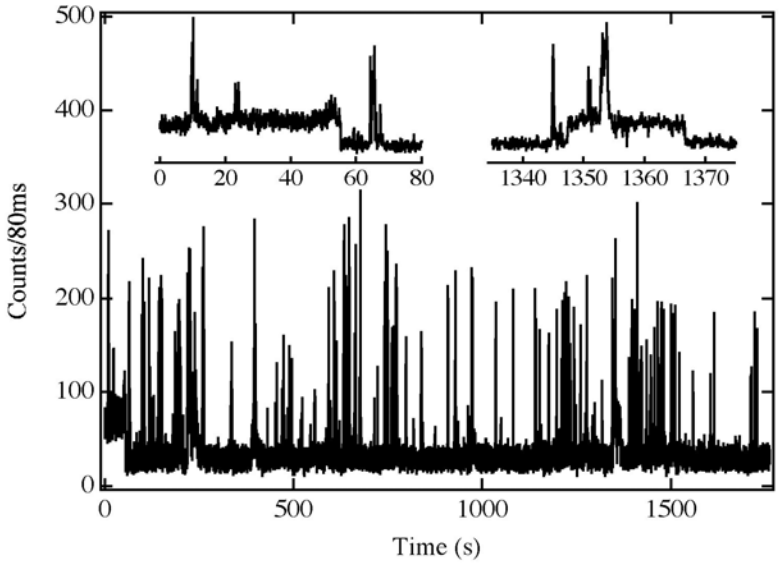


**Figure 4.7.** Time transient obtained at 1.6 nM concentration. The insets show expanded regions of the transient depicting two long adsorption events. This transient was excluded from the data set used to construct Figure 4.6 because of the appearance of these obvious adsorption events.

One other important factor that contributes to the large error bars in Figure 4.6 is the occasional appearance of adsorption events in the time transient data. Figure 4.7 depicts a representative example of this phenomenon with two clear adsorption events highlighted as insets. Such events are typified by observation of an approximately constant level of fluorescence that extends for a period of time substantially longer than most diffusive events.[43-45,55,57,200] Assuming these molecules are adsorbed in fixed orientations, such events should contribute *on average* twice as strongly to the autocorrelation decay amplitude as events due to rapidly reorienting molecules. The appearance of very few such events may have an even larger impact on the autocorrelation amplitude. The transient shown in Figure 4.7 was excluded from the data set used to construct Figure 4.6 for this reason.

## 4.4 Conclusions

A model describing the full concentration dependent amplitude of fluorescence autocorrelation data for samples comprised of single molecules entrapped in fixed but random orientations and exhibiting polarization dependent excitation and emission has been presented. The model has been verified using both simulated and experimental single molecule data. Its differences with previously published models, which assume polarization-independent excitation or emission processes, have been explored. The results prove that the exact nature of molecular orientation (fixed or rapidly reorienting) must be accounted for when determining concentrations (or relative concentrations) from single molecule autocorrelation data. All other parameters being equal, it may be concluded that fixed molecules contribute approximately twice as strongly to the autocorrelation decay as do rapidly reorienting molecules.

The orientation-dependence of autocorrelation amplitudes described here is relevant to concentration determinations in any system comprised of small objects (i.e. single molecules, nanoparticles, etc.) that exhibit polarization-dependent excitation or emission processes and which may be found in fixed orientations on relevant experimental time scales. Although this dependence was demonstrated using single molecule imaging results alone, it is also of importance to the interpretation of autocorrelation data from studies of reversible single molecule adsorption in/on thin films or surfaces, such as have been reported by our group[55,57] and by others.[43-45,164,200]

# CHAPTER 5 - Following the Growth Process in Macroporous Methylsilsesquioxane Films at the Single Macropore Level by Confocal Correlation Spectroscopy

This chapter has been published in *Chemistry of Materials*:

Hanjiang Dong, Fangmao Ye, Daniel A. Higgins* and Maryanne M. Collinson* "Following the Growth Process in Macroporous Methylsilsesquioxane Films at the Single Pore Level by Confocal Correlation Spectroscopy", *Chem. Mater.,* **2007**, *19*, 6528.

In this work, Dr Hanjiang Dong developed the sol recipe and prepared the monoliths, while I trained him on microscope operation and helped collect the light scattering data.

## 5.1 Introduction

Macroporous sol-gel derived monoliths and films represent an intriguing class of materials that have attracted considerable attention recently owing to their unique structural features and potential applications as catalyst supports, stationary phases for chemical separations, superhydrophobic materials, and as materials for drug delivery, chemical sensors and optics.[53,133,135,209-211] One common method for preparing these materials is by polymerization-induced phase separation (i.e., spinodal decomposition) in silicon-alkoxide-derived sols.[212] Methyltrimethoxysilane (MTMOS) represents an important example of the silicon-alkoxide precursors that have been employed in recent synthetic studies.[48,136,209,213] Hydrolysis and condensation of MTMOS in acidic water-methanol mixtures leads to formation of relatively nonpolar methylsilsesquioxane (MSQ) oligomers and polymers. Under appropriate conditions, MTMOS-derived MSQ polymers can spontaneously phase separate from the water-methanol solution, forming a two-phase system. Importantly, phase separation can occur without the use of additives (i.e. organic polymers).[214] Subsequent gelation converts the phase-separated sol to a rigid, porous matrix. Pore size and overall materials morphology can easily be controlled by simply varying the time between phase separation and gelation.[212] These same MSQ-based materials, prepared under slightly different conditions can also yield homogeneous sols, precipitates, or resins.[48,213] The diversity of materials that can be obtained results in part from the complexity of the phase separation and sol-gel transition processes.

A variety of methods such as NMR, XRD, light scattering, SAXS, confocal microscopy, electron microscopy, and porosimetry have been used previously to follow the sol-gel process in pore-forming and related systems and to probe the chemical and physical properties of the resulting materials. Unfortunately, few of these (e.g., NMR, light scattering, SAXS, confocal

microscopy) are capable of following real time changes during the sol-gel transition. The others (e.g., XRD, electron microscopy, porosimetry) can only be used to probe dried materials.[53,132,133,136,212-221] NMR, while invaluable as a means to determine the molecular species present, has not yet been used to probe the sol-gel process in phase-separated systems, likely because of sample inhomogeneity. Although laser scanning confocal microscopy has been used to image the static three-dimensional structures within macroporous sol-gel materials,[133,218] only aged wet gels and dried gels have been investigated. While conventional bulk light scattering methods have provided a wealth of information on the time evolution of such materials,[132,212] these methods primarily probe regions of high polymer concentration (the matrix, after phase separation and gelation have occurred). Importantly, the sol-gel dynamics in regions of low polymer content (the macropores) have not been previously directly probed by these or any other methods. As the silica, catalyst and solvent concentrations differ spatially within all these materials, a full understanding of their formation and aging can only be obtained by probing the dynamics in a spatially resolved manner.

In this chapter, an *in-situ* microscopic technique, confocal correlation spectroscopy (CCS),[137] is used to follow the polymerization of MTMOS films from before phase separation to well after gelation. Implementation of optical microscopic methods allows for the different phases (i.e. pores and matrix) to be distinguished from each other and separately probed with sub-micrometer-scale spatial resolution in real time. Light scattering by the individual MSQ "nanoparticles" that appear in the sol (before phase separation) or within the pores (after phase separation) is used as a means to follow the time evolution of these materials. Conceptually, CCS is similar to fluorescence correlation spectroscopy,[86] commonly used by our groups[55,136] and others to study sol-gel derived materials.[61,90,160] However, because no dyes are employed in

the present studies, the structural evolution of the individual sol-gel derived particles that ultimately come together to form the matrix may be probed without concern for the effects of dye partitioning and dye-matrix interactions.

## 5.2 Experimental Section

### *5.2.1 Sample Preparation.*

All chemicals employed, including methyltrimethoxysilane (MTMOS, >98%), nitric acid ($HNO_3$), water (HPLC grade) and methanol (MeOH, HPLC grade) were obtained from Aldrich and were used as received. Bulk samples were prepared using a procedure modified from the literature.[222] Briefly, 0.50 mL of MTMOS and 0.14 mL of MeOH were first mixed in a small vial. After 5 min, 0.13 mL of 1M $HNO_3$ was quickly added. The mixture was then vigorously agitated for 1 min at room temperature. The final mole ratios of Si:$H_2O$:MeOH were 1:2:1.

Preparation of MSQ films for use in the CCS studies was performed 20 min after preparation of the sol. In this procedure, a 1.5 μL aliquot of the sol was dropped onto the center of a microscope cover slide. The slide was then quickly covered with a second cover glass to spread the sol and to prevent its evaporation. The films obtained were determined to be 2-5 μm thick by optical microscopy (see below).

### *5.2.2 Optical Microscopy.*

Samples prepared by the above procedure were immediately transferred to a sample scanning confocal microscope for imaging and for the recording of time transients. All experiments were performed under ambient lab conditions, with the top cover slide in place. The microscope employed was shown in Figure 2.4 in Chapter 2. Briefly, it is comprised of an inverted light microscope, upon which is mounted a closed-loop piezo-electric X,Y scanning stage. In the present experiments, the microscope was used in the epi-illumination mode to

selectively collect and detect 543.5 nm laser light scattered by the sample matrix and by MSQ particles within the film and pores. Incident light (< 3 μW) was delivered to the sample using a high numerical aperture (NA = 1.3) oil-immersion objective. A dichroic mirror (Chroma Technologies 565DCLP) was used to direct the laser light into the back aperture of this objective. The same objective was used to collect light scattered by the sample. Light collected from the sample subsequently passed through the dichroic mirror and into the detection path. The dichroic mirror served to reduce the intensity of the scattered light into the linear range of the single-photon-counting avalanche photodiode detector.[137] Pulses from the detector were counted using a National Instruments counter-timer card (PCI-6602).

### *5.2.3 Other Characterization Methods.*

SEM images were obtained using a Hitachi S-3500N SEM with an acceleration voltage of 20 KV. The surfaces of the samples were coated with ~ 50 Å of gold before imaging by SEM. Optical density data from the bulk sols were obtained at a wavelength of 543.5 nm, using a HP 8453 diode array spectrometer. Film thickness was obtained using the optical microscope described above. For this purpose, the incident laser light was alternately focused on the glass/sol interfaces of the upper and lower cover glasses. The distance between these two foci was read from the calibrated scale on the microscope focal knob and was recorded as the film thickness.

## 5.3 Results and Discussion

### *5.3.1 Imaging of Macroporous MSQ Films.*

A variety of different materials, including homogeneous and phase separated sols and gels can be prepared when MTMOS is hydrolyzed and condensed.[48] The type of material formed depends on the Si:water ratio, the catalyst, the pH of the sol, and whether a one-step or

two-step polymerization procedure is employed.[48,215] In contrast to what was believed a decade ago, it has recently been shown that gels can be formed from MTMOS sols when the pH is very low.[48,133] In the present work, the Si:water ratio was 1:2, just above the stoichiometric requirement, and the sols were highly acidic (pH ~ 1). Under these conditions, both phase separation and gel formation occur.

Optical images of the films prepared as described above provide a detailed view of MSQ film evolution from before phase separation to well after gelation. Figure 5.1 shows representative examples of the images obtained. The signal at each pixel in these 100 X 100 pixel images was integrated for 40 ms. Spectra of the light collected proved that elastic scattering by the sample was the dominant source of signal and optical contrast in all such images. Also shown in Figure 5.1 is the time dependent optical density of the bulk sol from which this film was prepared. These latter data were recorded from just after sol preparation until just after phase separation.

At early times (i.e. for a period of more than 5 h), no distinct features are observed in the optical images. However, all such images yield signals larger than the dark background of the microscope. As noted above, these signals arise from light scattering by the sol. Here, light scattering is specifically attributed to scattering by MSQ "nanoparticles". The presence of these nanoparticles is supported by the gradual increase in optical density observed for the bulk sol (see Figure 5.1) at early times. SEM data obtained from gelled films (see below) provide further evidence of their existence. The formation of such particles is also well-known from previous SAXS studies of similar materials.[223] However, the nanoparticles formed at early times are not likely to be true solid particles of well-defined shape. Rather, they likely consist of weakly

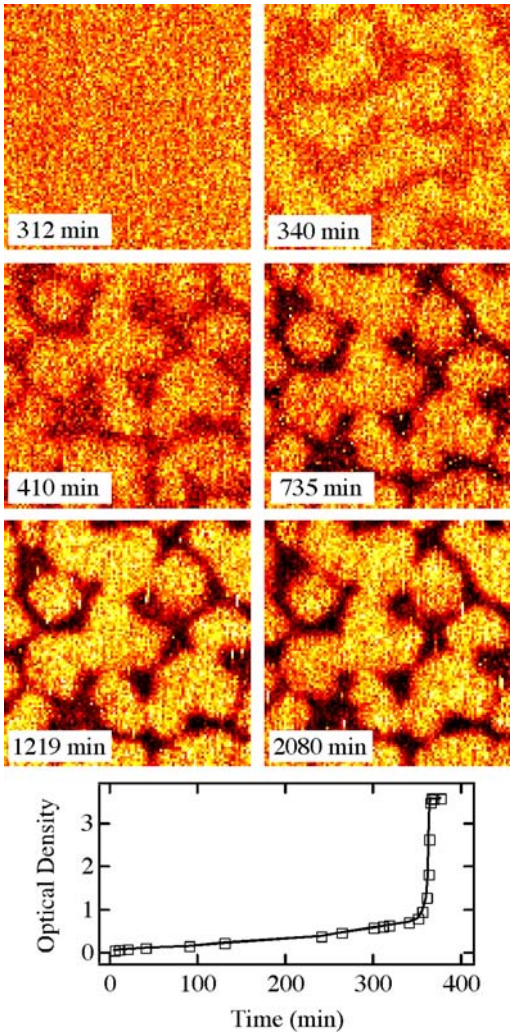


**Figure 5.1.** Optical images (top, 10 X 10 $\mu m^2$) of an MSQ film as a function of time after sol preparation. Prior to phase separation (< 340 min) the film uniformly scatters light. At 340 min, the sol undergoes a spinodal decomposition and a two-phase system appears. The bright regions are the matrix (high silica concentration), the dark regions the pores (low silica concentration). The two phases continue to evolve (i.e. they remain mobile) until sometime after the gel transition in the film (> 410 min). Beyond 735 min, the film structure is observed to be stable, although the optical contrast between matrix and pores continues to improve. Optical density (bottom) at 543 nm as a function of time obtained from the associated bulk gel. These data show that phase separation occurs at approximately the same time in the bulk gel and the film. Gelation occurs in the bulk gel at 405 min.

cross-linked (i.e. low density) MSQ oligomers having optical properties that differ only modestly from the solvent (i.e. methanol).

Phase separation (i.e. spinodal decomposition) is observed to occur in this film just prior to 5 h 40 min (340 min), as evidenced by formation of a two-phase system at this point (see Figure 5.1). The two phases consist of regions high in MSQ polymer concentration (bright regions exhibiting relatively strong light scattering) and those that are low in MSQ concentration (dark regions exhibiting relatively weak scattering). It should be noted that the time at which phase separation occurs is defined here as the first appearance of a two-phase system in the optical microscope. In previous reports, phase separation has often been defined as the time at which the sol just begins to turn turbid.[222] Here, the plot of optical density vs time for the bulk sol (Figure 5.1) provides this information. In this plot, the optical density is observed to gradually increase for more than the first 5 h. It then abruptly rises at 5 h 50 min (350 min), a time that is consistent with the phase separation time deduced from the optical images. These data suggest that there is little difference in the hydrolysis and condensation processes of the bulk sols and films studied here. Similarities between these samples are not surprising since the micron thick films are really "thin monoliths" that are also kept covered (like the bulk samples) to minimize evaporation.

After phase separation but prior to gelation, the regions of high and low MSQ concentration continue to evolve in size, shape and position, as evidenced by the images shown in Figure 5.1. The time between phase separation and gelation is one of the most important factors governing the final morphology of these macroporous materials.[212] At the gelation point, the regions of high MSQ concentration rapidly form a rigid, permanent structure: the "matrix".

The regions of low MSQ concentration become the "pores" of the matrix and are filled primarily with liquid solvent at this point.

The time at which gelation occurs can also be deduced from the images shown in Figure 5.1. In this particular sample, the size and shape of the individual regions show little change after 6 h 50 min (compare images recorded at 410, 735, 1219, and 2080 min). Therefore, this is concluded to be the approximate time of film gelation. The film gelation time closely corresponds to the 6 h 45 min (405 min) gelation time observed in the bulk sample. Gelation was detected in the bulk sample by observation of a dramatic change in sol viscosity.

The optical images obtained after gelation indicate the films are comprised of pores having 1-2 μm cross-sectional dimensions. Because they are interconnected, the pores often appear as "channels" with lengths in excess of 10 μm. The pores are separated from each other by regions of solid MSQ matrix that, on average, are similar in size to the pores. Convolution of physical matrix structures with the ~ 300 nm $1/e^2$ radius of the Gaussian laser profile used to image the samples causes some broadening of the image features.

As a final observation from the optical images (Figure 5.1), it should be noted that while the pore and matrix structures become fixed at the time of gelation, the optical contrast between these regions continues to increase for many hours. This observation is consistent with the continued evolution of the chemical and physical properties of these regions. Specifically, increased light scattering from the matrix reflects its continued densification and a corresponding increase in its refractive index (relative to that of the solvent-filled pores). Likewise, a steady reduction in overall light scattering observed from the pores reflects time-dependent changes in the number of MSQ nanoparticles present. Light scattering from the pores is primarily manifested as bright horizontal "streaks" in the optical images (see Figure 5.1). These results

indicate light scattering from the pores is dominated by "random" passage of mobile MSQ nanoparticles through the focal volume of the microscope. It is noteworthy that the brightness of these steaks increases in time, consistent with continued growth and densification of the nanoparticles long after gelation has occurred.

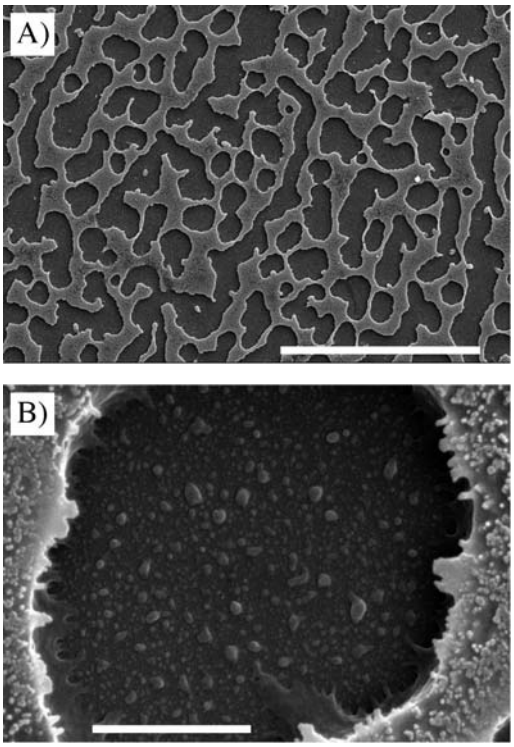


**Figure 5.2.** A) and B) Low and high magnification SEM images of the MSQ film used in the optical studies. The covering glass slide was removed well after gelation and aging (> 35h) to obtain these images. The pores (depressions), matrix (surrounding raised ridges) and small particles are clearly visible. Particles having a broad distribution of sizes are found within the pores. The largest particles observed in this region are ~ 200 nm in diameter. Particles of smaller average size are observed on the matrix. A) Scale bar: 50 μm. B) Scale bar = 2 μm.

Higher resolution images of the MSQ films were obtained by SEM. Figure 5.2 shows representative examples. These images provide further support for the above conclusions pertaining to film morphology and composition. Both images were obtained from the film shown in Figure 5.1, although the areas imaged are different. SEM images provide a good

picture of the final structure of ***dried*** macroporous MSQ materials, but they provide no information on the time evolution of the film structure. The features observed are also potentially altered from their original state during the drying process. However, the optical and SEM images provide a consistent view of the matrix and pores. The SEM image shown in Figure 5.2A depicts round and oblong interconnected pores. The smallest pores observed at this magnification are 1-2 μm in size, while larger pores having widths on the order of 5-10 μm and lengths of more than 50 μm are also frequently observed. Figure 5.2B shows a highly magnified SEM image of a single ***dried*** pore of relatively large (~ 5 μm) diameter. Clearly apparent in this image are a large number of MSQ particles on the matrix surfaces (raised outer regions in the image) and within the pore. Such images prove that the MSQ nanoparticles described above exist within these films. The particles found on the matrix surface are all very small, having diameters of ~ 50 nm or less. In contrast, the particles found within the pore exhibit a broad distribution of sizes with the largest having ~200 nm diameters.

### *5.3.2 Single Point CCS Studies of MSQ Film Evolution.*

While the optical images discussed above provide an initial view of overall MSQ film properties, as well as the phase separation, gelation and aging processes, detailed investigations of these materials in general and the properties of their solvent-filled pores in particular require implementation of altogether different methods. Here, confocal correlation spectroscopy (CCS)[137]provides valuable new data on the time evolution of the film properties in a spatially resolved fashion, by following time dependent changes in the mobilities of MSQ nanoparticles found within the films. Previous studies have on only reported on the static properties[133,218] and bulk dynamics of related materials.[132,212]

CCS involves the recording of time dependent optical signals (i.e. time transients) from selected locations in the sample. As particles of sufficient size and appropriate optical properties migrate through the microscope focal volume, they produce "bursts" of scattered light. Autocorrelation of the time transients obtained provides the average time spent by the particles in the detection volume. The results yield information on the average size of the particles and/or the viscosity of the film region being probed. In the present studies, light scattering arises specifically from passage of MSQ nanoparticles through the detection volume. Interference from other regions of the film (i.e. static scattering by the matrix in gelled MSQ films) is virtually eliminated by the confocal nature of the method.

Representative time transients incorporating numerous bursts of scattered photons are shown in Figures 5.3A and C. Only the first 100 s of each transient is shown to better highlight the bursts, which are most clearly visible in Figure 5.3C. Figure 5.3B shows a greatly expanded section of the transient shown in Figure 5.3A for this same purpose. These time transients were obtained from single points in the film shown in Figure 5.1. In the case of Figures 5.3A,B the transient shown was obtained from a randomly selected position in the uniformly scattering film prior to phase separation. These data were obtained 70 min after sol preparation. The transient shown in Figure 5.3C was obtained by positioning ***an individual pore*** within the microscope focus after phase separation had occurred. This particular transient was obtained 16 h 40 min (1000 min) after sol preparation. Numerous such transients were recorded from this same sample over a period of approximately 35 h. The vast majority of transients were recorded with a time resolution of either 1 ms or 3 ms. In all cases, the transients were obtained from random positions prior to phase separation and from the pores after phase separation. Transients

obtained from the matrix regions (not shown) yielded strong, constant (aside from shot noise) light scattering signals.

After each time transient was recorded, it was subsequently autocorrelated as follows:

$$G(\tau) = \frac{\langle I(t)I(t+\tau)\rangle}{\langle I(t)\rangle^2} - 1 \tag{5.1}$$

In Eqn. 5.1, I(t) represents the time transient, $\tau$ is the discrete time base of the autocorrelation function and the brackets < > indicate the average value over time is taken. Figures 5.3D,E depict the autocorrelation functions obtained from the time transients shown in Figures 5.3A,C. As is obvious from Figures 5.3D,E, the average length of time the nanoparticles spend in the microscope detection volume increases dramatically with time, from ~ 1.1 ms at 70 min to ~ 50 ms at 16 h 40 min.

Quantitative data from these autocorrelation functions was obtained by fitting them to an approximate expression that models free (unhindered) diffusion of the nanoparticles in three dimensions. The results provide estimates of both the amplitude and rate of decay for each set of data. The specific equation employed in fitting the data was:

$$G(\tau) = \frac{A_1}{\left(1 + D_1\tau/s^2\right)\sqrt{1 + D_1\tau/s_z^2}} + \frac{A_2}{\left(1 + D_2\tau/s^2\right)\sqrt{1 + D_2\tau/s_z^2}} + B \tag{5.2}$$

Here, $A_1$ and $A_2$ represent the amplitudes of two distinct diffusional decays, while $D_1$ and $D_2$ represent the apparent diffusion coefficients for these two components. The parameter B is a constant used to properly fit the data, while $s^2$ and $s_z^2$ represent the transverse beam variance (determined elsewhere to be 2.6 X $10^{-10}$ $cm^2$) and the longitudinal beam variance (assumed to be $2s^2$), respectively, at the microscope focus.

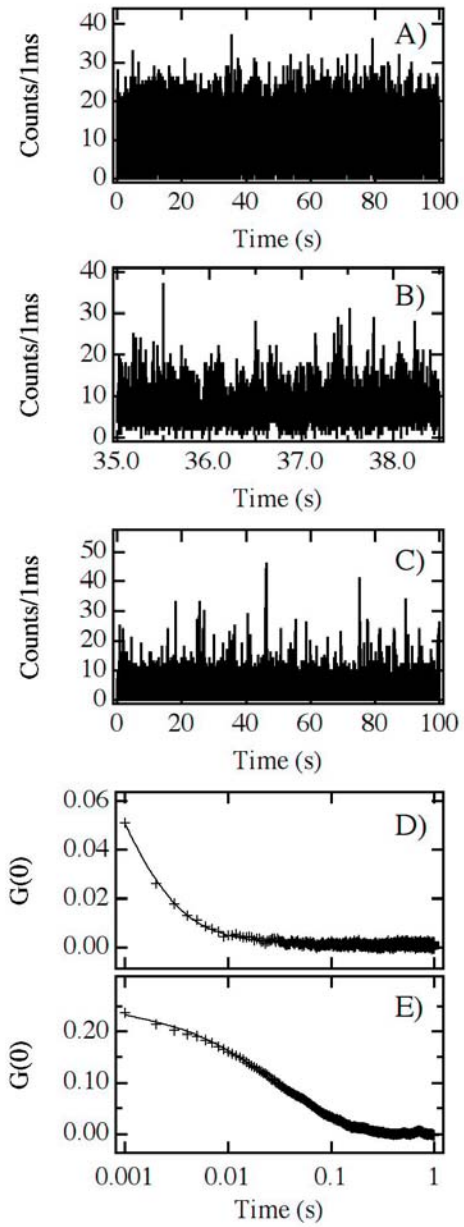


**Figure 5.3.** A)-C) Representative time transients and D), E) associated autocorrelation functions obtained from the film/pores shown in Figure 5.1. A) and D) Data obtained at early times, prior to phase separation (70 min). B) Expanded region of the transient shown in A) and depicting signal fluctuations due to light scattering by small, mobile MSQ particles. C) and E) Data obtained at much later times (1000 min) also depicting scattering by MSQ particles. The longer autocorrelation decays observed at long times (compare D) and E)) reflect much slower, possibly hindered diffusion by larger MSQ particles in the pores of the film.

Prior to phase separation, virtually all of the data obtained could be fit to a single diffusional component (i.e. $A_2 = 0$ in Eqn. 5.2). Such a result is consistent with a monomodal, random distribution of MSQ particle sizes. After phase separation, many of the autocorrelation functions showed clear evidence for the presence of a bimodal distribution of particles. As shown in Figure 5.3E, there is a dominant slow component to the decay and a small component (barely visible) associated with a faster decay. The latter decay occurs on a time scale very similar to that of the autocorrelation data obtained prior to phase separation.

The apparent D values obtained as a function of time provide valuable new insights into the evolution of the MSQ films. Figure 5.4A plots these data. Note that only the D values for the slow diffusional component are plotted in cases where a bimodal decay was observed. The fast component was frequently too small to yield results that could be quantitatively interpreted. In addition, the autocorrelation functions obtained between the phase separation and gelation times could not be reasonably fit to the above model. This is likely because of strong fluctuations in the local sample composition that occur during this time frame. These data have been excluded from Figure 5.4.

Aside from a couple of points at ~11.5 h, where the D values obtained were unexpectedly low, the results in Figure 5.4 can otherwise be roughly divided into two regions: those obtained before 10h and those obtained afterwards. Prior to 10 h, the apparent D values fluctuate around an average of ~ $2 \times 10^{-7}$ $cm^2/s$. This result suggests the MSQ nanoparticles grow rapidly to a certain size but do not grow further until well after gelation. After 10 h (i.e. ~ 3 h after gelation), the apparent D values begin to decrease dramatically, suggestive of either a change in pore viscosity or a resumption of particle growth. This relatively long delay between gelation and the onset of changes in the apparent diffusion coefficient has been observed in several different

experiments on different samples prepared and studied under the same (or very similar) conditions.

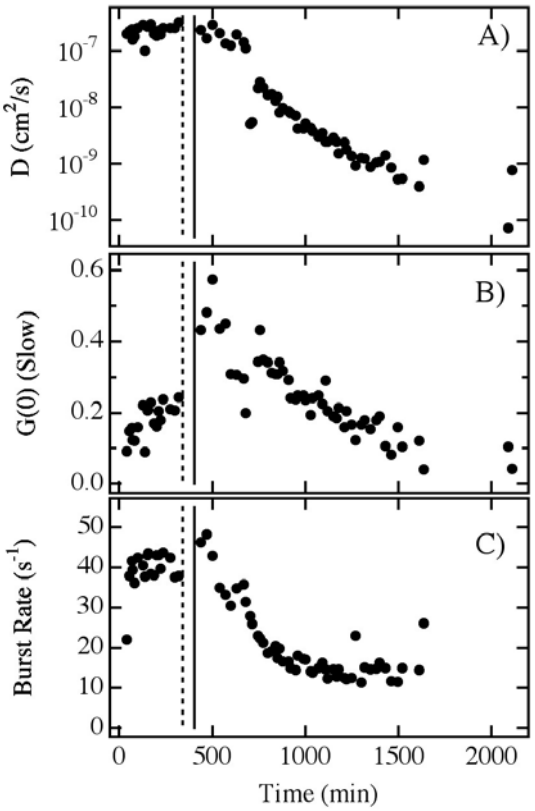


**Figure 5.4.** A) Diffusion coefficient (slow component) as a function of time for MSQ particles found in the pores of the film shown in Figure 5.1. B) Amplitude of the slow diffusion component. These data were obtained by fitting the autocorrelation functions to the equation described in the text. C) Burst rate as a function of time. The vertical dashed line indicates the point at which phase separation occurred. The solid line depicts the time at which gelation of the bulk sample was observed. Data obtained near the phase separation and gelation times was excluded for the reasons discussed in the text. The last two points in C) are not shown because these data were recorded using a longer bin time, yielding burst rates that were difficult to reconcile with the earlier data.

Regardless of the mechanism, it is clear that the average size of the particles detected remains approximately constant over the first 10h. The average D value obtained may be used to estimate the average size of these particles. Assuming the particles are spherical in shape (see

Figure 5.2), the Stokes-Einstein Equation provides an estimate of the particle diameter. Here, d = kT/(3πηD), where k is the Boltzmann constant, T is absolute temperature (293 K), and η is the viscosity of the liquid comprising the film. If the film behaves approximately like a mixture of water and methanol prior to phase separation and gelation, a viscosity of 0.8 cP may be assumed. With an average D = 2 x $10^{-7}$ $cm^2/s$, a particle diameter of ~ 26 nm is obtained. Note that this particle size corresponds reasonably well to the size of the particles observed on the matrix in Figure 5.2B.

The data shown in Figure 5.4 suggests particles of this size appear in the film very early, prior to collection of the first time transient. It is unlikely that the particles all grow rapidly to this size in the first few minutes. Rather, it is more likely that there exists a (broad) distribution of particle sizes and that only particles of a minimum size are being detected.

The minimum detectable particle size was estimated here using Mie Scattering Theory.[224] In making this estimate, it was assumed that only those particles producing signals equivalent to twice the background could be detected. The background count rate in these experiments was estimated to be ~ 3 $ms^{-1}$. Assuming a detection efficiency in the microscope of ~ 1% and an incident power of 3 μW, only those particles having backscattering cross-sections of > 2x$10^{-16}$ $cm^2$ would produce detectable bursts. Assuming a refractive index of 1.33 for the sol and 1.4 for the MSQ particles formed at early times, one obtains a minimum detectable particle diameter of 34 nm from Mie Theory.[224] Since conventional Mie Theory assumes illumination by an infinite plane wave,[224] it is expected the minimum detectable particle size may be somewhat smaller in the microscope. It is therefore concluded that during the initial 10 h of data collection, the MSQ nanoparticles take on a broad distribution of sizes, with the detectable particles growing to a size of ~ 30 nm.

The amplitude of the autocorrelation data provides strong evidence that smaller particles continue to grow to a size of ~ 30 nm prior to film gelation. Figure 5.4B plots these amplitudes (only the slow component is used for bimodal decays) as a function of time. Prior to phase separation and gelation, the amplitude of the autocorrelation decay increases steadily in time. As has been shown previously,[179,225] for background-limited detection of single particles, the autocorrelation amplitude exhibits a complicated dependence on particle concentration. However, at the lowest concentrations, the amplitude may be assumed to increase linearly with concentration. Therefore, these data suggest that while the particles grow no larger than ~ 30 nm at early times, the number of such particles of this size is continuously increasing. The increase in autocorrelation amplitude may also reflect densification of the silica particles, producing particles that have a greater refractive index and more strongly scatter the incident laser light. In either case, these results point to the continued evolution of the MSQ nanoparticles, namely via formation of Si-O-Si bonds. The gradual rise in the optical density of the bulk sample (see Figure 5.1) prior to phase separation is also consistent with this conclusion: either the number of particles present is increasing or their light scattering efficiency is increasing. Shortly after phase separation and gelation (at 410 min), the autocorrelation amplitude begins to decrease, indicative of a time-dependent decrease in the concentration of nanoparticles within the pores. Note that this behavior contrasts with the time dependent D values obtained in that the D values remain approximately constant for a long period of time (~ 3 h) after gelation, suggesting little or no growth of detectable particles is occurring.

Because of the complex dependence of the autocorrelation amplitude on concentration changes,[179,225] the burst rate (i.e. number of bursts per second) observed in each transient was also calculated from the time transient data and used as a means to observe changes in the

particle concentration. The observed burst rate is also expected to be proportional to, among other things, the concentration of detectable particles present, assuming their concentration is sufficiently low. The burst rate was obtained by first determining the average background count rate in each transient. All bursts for which the signal exceeded the background fluctuations at the 99.9% probability level (assuming the background is Poisson distributed) were then counted. Figure 5.4C plots the results obtained. As with the autocorrelation amplitude data, the burst rate increases up until phase separation and gelation, consistent with an increase in the concentration of 30 nm particles during this time. As with the autocorrelation amplitude and in contrast to the D values, the burst rate data also begins to decrease shortly after gelation of the film, suggestive of the onset of a monotonic time-dependent decrease in the number of particles present within the pores. Taken together, the observed changes in the autocorrelation amplitude and the burst rate provide strong evidence for a decrease in the nanoparticle concentration after gelation.

### *5.3.3 Interpretation of CCS Results and Proposed Nanoparticle Growth Mechanism.*

The nanoparticle growth, phase separation, gelation and aging processes are all very complicated, involving chemistries that varying substantially in time. The relevant processes that are believed to occur are described below for the different time periods involved in the evolution of these materials.

#### *5.3.3.1 Prior to Phase Separation*

The initial growth mode likely involves reactions between monomers and small MSQ oligomers. Unfortunately, this early phase of oligomer growth cannot be followed in the present studies because the structures formed are too small to be detected. However, these processes have been investigated previously in related materials by NMR.[216,217,219,226]

Under the conditions employed in MSQ synthesis (pH ~ 1 and Si:water ratio 1:2), hydrolysis of MTMOS is expected to be very rapid.[217,219,226] The hydrolyzed monomeric species thus produced then condense to form dimers, trimers and other small linear and cyclic oligomers.[14,113] Condensation in these materials may occur between neutral and protonated silanol groups. As has been suggested previously, the least condensed MSQ species are expected to incorporate the most basic silanols while the most condensed species are most acidic.[14,113] Steric effects may also play a significant role,[219] with early reactions preferentially occurring between weakly condensed species. As the monomers are consumed, the growth mechanism becomes dominated by reactions between larger oligomers (sterically hindered species that may also incorporate neutral silanols) and smaller oligomers (unhindered species incorporating protonated silanols). As larger polymers are formed, they become visible in the CCS experiments. At the same time, the particle growth rate slows dramatically because the concentration of reactive small species decreases as they are incorporated into larger structures and because of the reduced reactivity (i.e. decreased basicity and increased steric hindrance) of the silanols present on relatively large MSQ polymers. Particle growth by interparticle aggregation is also unlikely at this point because of reduced surface reactivity, increased steric hindrance and a reduction in the rate of particle diffusion (and hence particle collisions) as the particles grow. This decline in particle growth rate becomes most noticeable at times close to phase separation/gelation. In the present experiments, this growth process results in the production of nanoparticles having a maximum size of ~ 30 nm. Particle size remains (temporarily) stable after this point.

#### *5.3.3.2 Phase Separation/Gelation*

While particle growth is interrupted for the above reasons, intraparticle condensation continues to occur. The nanoparticles densify in time and also become less polar. A decrease in polarity results from the time-dependent decrease in silanol density. At some point in time, a critical concentration of nonpolar species is reached and phase separation occurs, forming a two-phase system incorporating regions of high (the "matrix phase") and low (the "pore phase") MSQ concentrations. The least polar, most highly condensed species dominate in the high concentration regions, while the low concentration regions are comprised primarily of solvent, but also incorporate the most polar, least condensed nanoparticles.

Aggregation of the least polar MSQ species in the matrix phase and subsequent condensation of their residual silanol groups leads to gelation of the matrix. In contrast, in the pore phase, the concentration of nanoparticles is relatively low, interparticle collisions are infrequent, and the nanoparticles themselves remain predominantly nonreactive towards each other. The least polar of these particles can still react with and become incorporated in/on the matrix. This process is reflected by the decrease in particle concentration observed shortly after matrix gelation in the autocorrelation amplitude and burst rate data shown in Figure 5. 4.

#### *5.3.3.3 After Gelation*

In time, the condensation reactions occurring within the pore-phase nanoparticles cause them to become sufficiently nonpolar that they begin to aggregate and react with each other. A resumption of particle growth in the individual pores is then observed. In these particular materials, this process requires approximately three additional hours after phase separation, as reflected by the delayed onset of the decrease in D shown in Figure 5.4.

As noted above, the decrease in D after 10 h is consistent with either the resumption of particle growth, or a change in the viscosity of the liquid-filled pores. The latter mechanism is

discounted based on the observation of two-component diffusion within the pores at these later times. The fast diffusional components in many of the autocorrelation decays yield apparent D values similar to those obtained at early times, prior to phase separation. This result suggests that some smaller particles remain in the pores over very long periods of time. Regardless of the origins of these small particles, their relatively fast diffusion indicates that the viscosity of the liquid-filled pores has not changed substantially. It is therefore concluded that the drop in D observed after 10 h results entirely from particle growth by an aggregation mechanism.

The Stokes-Einstein Equation again provides a means to estimate particle size as nanoparticle growth resumes. All such estimates assume the viscosity of the liquid filled pores remains approximately constant. The particles apparently grow from the initial minimum detectable size of ~ 30 nm to diameters of ~ 300 nm after only 3 h of additional aging (beyond 10 h). Only a few hours later, the D values obtained suggest unrealistically large particles of > 3 μm average diameters. The SEM results described above suggest that the particles do not grow significantly beyond a few hundred nanometers in size. The observed decrease in D is thus concluded to reflect the onset of strongly hindered nanoparticle diffusion within the MSQ pores. It is well-known that once the particles grow to sizes larger than ~ 10% of the pore size, the D values obtained will fall precipitously from those expected for free diffusion.[227] As may be estimated from the optical images shown in Figure 5.1, the pores investigated in these studies are at most a few micrometers in diameter, indicating hindered diffusion should become important as the particles grow to diameters of only a few hundred nanometers.

As a final caveat, it should be noted that the SEM images shown in Figure 5.2 provide support for the above particle growth mechanism. The particles trapped on the matrix are all observed to be of relatively small size (~ 50 nm or less in diameter). In contrast, those found

within the pores take on a broad range of sizes from very small to as large as a few hundred nanometers. As defined in the above mechanism, the particles found on the matrix surfaces were likely deposited after phase separation and gelation had occurred but prior to the onset of nanoparticle aggregation. Therefore, they remain smaller in size. In contrast, the particles found in the matrix had the opportunity to grow further by particle aggregation and are observed to be larger as a result.

## 5.4 Conclusions

Optical microscopy was used to directly observe phase separation and gelation in macroporous MSQ films formed from MTMOS under low pH conditions. When coupled with *in situ* single-site confocal correlation spectroscopy and scanning electron microscopy, valuable information on film morphology and the growth of MSQ nanoparticles in the liquid filled pores of the MSQ matrix was obtained. It was found that the MSQ nanoparticles grew to a maximum diameter of ~ 30 nm soon after film preparation and remained in this size range until well after gelation. Nanoparticle size stabilization was attributed to consumption of reactive MSQ species, to a condensation-induced decrease in nanoparticle surface reactivity, and to a decrease in the collision rate of the MSQ particles as they grow. Incorporation of some nanoparticles in/on the matrix commenced shortly after gelation, as evidenced by a time-dependent decrease in the number of particles present in the pores. In contrast, the onset of particle-particle reactions within the individual pores was delayed for approximately three hours after gelation, at which time a significant time-dependent decrease in the nanoparticle diffusion coefficient was observed. Nanoparticle growth in this later phase was attributed to particle aggregation after a further evolution of their properties.

The ability to probe macroporous sol-gel derived films at the single pore level by optical microscopic methods will pave the way to a deeper fundamental understanding of the phase separation, gelation and aging processes in these technologically important materials. Extensions of these methods will also allow for a better understanding of phenomena such as hindered diffusion within the macropores and molecule-matrix interactions in chemical or biomolecule separations.

# CHAPTER 6 - Preparation and Characterization of Silica Thin Films Incorporating Polarity Gradients

A manuscript based on this work has been submitted to *Chemistry of Materials*:

Fangmao Ye, Dong Dong, Maryanne M Collinson* and Daniel A Higgins* "Polarity Gradients in Silica Thin Films by Infusion-Withdrawal Dip-Coating", *Chem. Mater.,* **2009** submitted.

In this work, Dr. Dong Dong (Virginia Commonwealth University) performed all FTIR imaging.

## 6.1 Introduction

The preparation of films and surfaces incorporating physical and chemical (i.e. compositional) gradients is a topic of contemporary scientific interest.[203,228-236] "Functionally graded" materials,[233] incorporating gradients in polarity, porosity, ionic site density, thickness, molecular weight, etc.[203,231,234-236] have potential applications as stationary phases for chemical separations,[228] as materials for combinatorial catalysis[237] and as absorbent/adsorbent layers for use in chemical or biological sensors.[238] Related surface gradients have been used to regulate adhesion of cells,[229,239,240] to direct the growth of neurons,[229] and even to drive the transport of liquids.[205]

A wide variety of approaches have been used to prepare gradient materials.[230,232] Representative examples include solution[207] and gas phase[241] surface modification of organic polymers; deposition of polymers from prepolymer solutions;[242,243] solution and vapor phase diffusion and surface modification using alkanethiols[238,239] and organosilanes;[205,244] and deposition of polymers[236,240] and manipulation of surface reactive species[203,235] by electrochemical means. Additional examples and further discussion of alternative methods and materials can be found in recent reviews on soft matter gradients.[230,232] The methods described in these reviews constitute an extensive toolbox for the spatial and temporal control of materials properties. However, the continued exploration and implementation of alternative materials chemistries in the preparation of gradients is also required if the true potential of these methods is to be fully realized. As eloquently stated by Wang, Haasch and Bohn "… the utility of anisotropic in-plane gradient surfaces scales directly with the range of chemical and physical properties that can be accessed and manipulated…."[236]

The sol-gel process[14,34,79] represents an important and convenient route to the preparation

of a virtually unlimited range of materials having a wide range of physicochemical properties. While simple silica materials can be prepared via the acid-catalyzed hydrolysis and condensation of tetramethoxysilane (TMOS),[14,34,79] more complex organic-inorganic hybrid materials can be prepared using mixed sols containing one or more organoalkoxysilanes ($R'$-$Si(OR)_3$, where R and R' represent organic groups).[21,24,27] In this work, we show for the first time how ***temporal*** control over the sol composition can be utilized to prepare thin silica films with functionally graded properties. The range of gradients that can be prepared by this approach is virtually unlimited due to the enormous selection of commercially available organoalkoxysilanes. Furthermore, materials composition and properties can be altered by simply changing the precursors employed. In spite of its potential utility, the sol-gel process has seldom been employed in the preparation of gradient materials[245] and much remains to be learned about the range of materials and properties that can be accessed.

In this chapter, an unique "infusion-withdrawal dip-coating" process for the preparation of silica films incorporating macroscopic polarity gradients is described. Glass and silicon substrates were coated with sols of time-varying composition produced by slowly mixing TMOS- and MTMOS-based sols together. The time-varying sol composition led to a steady decrease in film polarity along the substrate surface. The gradients thus prepared were characterized by fluorescence spectroscopy, using Nile Red (NR) as a sensitive probe of film polarity properties.[79,99,101,102] Water contact angle measurements[205-208] and FTIR microscopy were used to obtain valuable supporting evidence of gradient formation. The fluorescence spectra obtained from NR-doped films exhibited a monotonic, position-dependent blue shift from the top of the film to the bottom, indicative of a decrease in film polarity from top to bottom. Likewise, water contact angle measurements showed a monotonic increase in the contact angle

from top to bottom, while FTIR microscopy showed an increase in methyl content relative to total silica proceeding down the gradients.

## 6.2 Experimental section

### *6.2.1 Sample Preparation*

Glass coverslips (Fisher Premium) and silicon wafers (Silicon Inc.) were both employed as substrates. Prior to use, all substrates were cleaned in fresh Piranha solution (Caution, Piranha solutions are extremely dangerous and react violently with organic materials); they were subsequently cleaned a second time in an air plasma. This two-step process ensured rigorous removal of all organic contaminants.

Adhesion of the precursor alkoxysilanes during gradient deposition was improved by first coating the substrates with a silica sublayer. Tetramethoxysilane (99%, TMOS, Fisher) sols were prepared for this purpose in a 1:11.5:5.1:0.006 (TMOS:$H_2O$:Ethanol:HCl(0.1 M)) mole ratio and were allowed to age for one day prior to use. The clean substrates were subsequently spin-coated with these sols and dried in a dessicator for one day. The resulting coatings were uniform and had thicknesses of ~180 nm, as determined by both profilometry and ellipsometry.

Production of silica film polarity gradients employed a time-varying mixture of two different sols. The first was a TMOS sol prepared in a 1:80:5.3:0.095 (TMOS:Ethanol:$H_2O$:$NH_4OH$(1 M)) mole ratio and subsequently aged for 6 h. The second was any of several different sols prepared using methyltrimethoxysilane (97%, MTMOS, Fisher). Typically, sols were prepared using different volumes of ethanol and constant water concentration. These sols were prepared in 1:10:4:0.072, 1:20:8:0.072 and 1:40:13:0.072 (MTMOS:Ethanol:$H_2O$:$NH_4OH$(1 M)) mole ratios and were aged for 6 h. All sols are designated

throughout this manuscript by their silane to ethanol mole ratios, i.e., as 1:10, 1:20, and 1:40 MTMOS sols.

Gradient films were deposited on the sublayer-coated substrates in a custom built glass reservoir designed to simultaneously minimize sol volume, decrease sol evaporation and allow for stirring of the sol mixture. A diagram of the apparatus and a photograph of the reservoir are shown in Figure 2.3 in Chapter 2. The glass reservoir includes a rectangular upper region having dimensions of 3.5cm × 0.5cm × 3.0cm (L × W × H) that was designed to admit one inch wide substrates. The lower portion of the reservoir was comprised of a small cylindrical vial (D=1cm, H=1cm). Two small glass tubes were installed at fixed locations inside the reservoir for infusion and withdrawal of the sols. All depositions were performed with the reservoir mounted atop a pneumatic vibration isolation table, with the reservoir housed in a closed Plexiglas box.

Deposition of silica film polarity gradients was accomplished as follows. A sublayer-coated substrate was first suspended in the middle of the reservoir. The initial TMOS sol was then transferred into the reservoir, submersing all but the top 1-2 mm of the substrate. The MTMOS sol selected for a given deposition was then loaded into a syringe and mounted in a syringe pump (NE-1000, New Era Pump Systems, Inc.). The syringe was attached to the reservoir via flexible plastic tubing. Gradient deposition proceeded by slowly infusing the MTMOS sol into the reservoir. The mixed sol contained in the reservoir was simultaneously withdrawn using a second, synchronized syringe pump also attached to the reservoir through flexible plastic tubing. The infusion pump was set to deliver MTMOS sol at a rate of 10.0 mL/h, while the other was set to withdraw 14.2 mL/h of mixed sol. The sol within the reservoir was carefully stirred at a constant rate, using a magnetic stir bar throughout this process. Prior to the start of deposition, it was verified that sol stirring produced no detectable movement of the sol

surface. The difference in infusion and withdrawal rates led to a steady decrease in the height (~ 0.3 mm/min) of the sol in the reservoir. The entire "infusion-withdrawal dip-coating" process lasted for ~ 1 h, producing an overall change of ~ 1.8 cm in sol height. After deposition, residual sol clinging to the bottom of the substrate was gently removed using a Kimwipe. The final gradient films were dried in a dessicator for 2 days.

Preparation of dye-doped silica gradients was performed on sublayer-coated glass coverslips and proceeded exactly as described above, except that both sols incorporated Nile Red (NR) at ~ 1 μM concentration. In some cases, gradients were simultaneously prepared on two coverslips, using the same sol mixture. In this case, the two substrates were assembled back-to-back with a thin film of glycerin between them. The thin layer of glycerin prevented silica deposition on the backside of the substrates. Without the glycerin layer, inadvertent coating of the substrate backside was found to interfere with the determination of polarity properties from the NR emission.

Nongradient silica films having uniform composition and polarity properties were prepared to verify the interpretations of data obtained from the gradients. For this purpose, TMOS (TMOS:$H_2O$:Ethanol:$NH_4OH$=1:80:5.3:0.095) and MTMOS (MTMOS:Ethanol:$H_2O$:$NH_4OH$ =1:10:4:0.072) sols were prepared as described above and aged for 6 h. One- and two-component sols containing different mole fractions of TMOS and MTMOS were then obtained by mixing appropriate amounts of each of these sols. Sols containing 0%, 20%, 40%, 60%, 80% and 100% MTMOS (relative to total silica content) were prepared and vigorously mixed for 20 min. These sol mixtures were then spin cast onto both clean and sublayer-coated substrates. All such films were dried in a dessicator at room temperature for 2 days prior to use.

### *6.2.2 Characterization*

The thickness and roughness of each sample was characterized on a macroscopic scale by spectroscopic ellipsometry (α-SE, J.A. Woollam) and on a microscopic scale by surface profilometry (XP-2, Ambios Technology; Santa Cruz, CA). The ellipsometric film thickness was measured every 1(±0.2) mm along the gradient direction.

Water contact angle measurements were performed on a homebuilt apparatus run by software written in-house. A Navitar camera was used to record droplet images in time. In these experiments, 2.5 μL drops of deionized water were deposited at regular intervals on the samples. Image acquisition was then initiated 3 s after addition of each drop to the sample surface. Automated routines incorporated into the instrument software were used to analyze the images obtained and to determine contact angles.

Fluorescence spectra were obtained from NR-doped gradient and nongradient (spin-coated) films using a home-built fluorescence microscope (see Figure 2.5, Chapter 2). Light (~1 μW) from a green HeNe laser (543.5 nm) was used to excite fluorescence in the samples. This light was focused into the back aperture of a 50X (0.55 numerical aperture) air objective, producing a 20 μm diameter spot in the sample. The same objective was used to collect the sample fluorescence and direct it through a holographic notch filter (Kaiser Optical) and into a 0.15 m spectrograph (Acton Research). A liquid-$N_2$-cooled CCD (Princeton Instruments) was used to record the spectra. Spectra were taken every 1(±0.2) mm along the gradient, using a 30 s integration time.

Transmission-mode FTIR microscopy was performed on a Thermoelectron FTIR Continuum Microscope coupled to a Nexus 670 spectrometer. Spectroscopic imaging was accomplished by averaging 300 interferometer scans using a 150X150$\mu m^2$ aperture. The

spectral resolution was 8 $cm^{-1}$. IR image data were acquired at 0.15 mm intervals along the gradients over a maximum distance of ~ 10 mm. The spectrum acquired in each region was baseline corrected and the areas under the $CH_3$ (2950-3000 $cm^{-1}$) and Si-O-Si (1000-1200 $cm^{-1}$) stretching absorptions were obtained.[14] The ratio of the $CH_3$ to Si-O-Si peak areas was calculated and used to assess the methyl content of the films. In the case of the Si-O-Si band, only the area under the low frequency half of the curve (baseline to peak, i.e., 1000 $cm^{-1}$ to 1080 $cm^{-1}$) was employed.

## 6.3 Results and Discussion

### *6.3.1 Model for Sol Composition*

The "infusion-withdrawal dip-coating" procedure employed in gradient preparation produces a sol of complex, time-varying composition. Predictions of the sol composition at each instant in time can be readily obtained from a simple mathematical model of the process. Here, the rates of change for the TMOS and MTMOS concentrations in the deposition reservoir are defined by the following two differential equations:

$$\frac{dC_{TMOS}(t)}{dt} = -\frac{C_{TMOS}(t)F_{out}}{V_{sol}(t=0) - (F_{out} - F_{in})t} \quad (1)$$

$$\frac{dC_{MTMOS}(t)}{dt} = \frac{C_{MTMOS,b}F_{in} - C_{MTMOS}(t)F_{out}}{V_{sol}(t=0) - (F_{out} - F_{in})t} \quad (2)$$

Here, $V_{sol}(t=0)$ is the initial sol volume (10 mL) in the deposition reservoir. $C_{TMOS}(t)$ and $C_{MTMOS}(t)$ represent the time-dependent concentrations of TMOS and MTMOS in the reservoir, while $C_{MTMOS,b}$ represents the time invariant concentration of MTMOS in the infusion sol. Finally, $F_{in}$ and $F_{out}$ represent the volume flow rates for the infusion and withdrawal processes.

Solution of the above two equations yields the following expressions describing $C_{TMOS}(t)$ and $C_{MTMOS}(t)$:

$$C_{TMOS}(t) = C_{TMOS}(t=0)\left(\frac{V_{sol}(t)}{V_{sol}(t=0)}\right)^{F_{out}/(F_{out}-F_{in})} \quad (3)$$

$$C_{MTMOS}(t) = C_{MTMOS,b}\frac{F_{in}}{F_{out}}\left(1-\left(\frac{V_{sol}(t)}{V_{sol}(t=0)}\right)^{F_{out}/(F_{out}-F_{in})}\right) \quad (4)$$

where, $V_{sol}(t)$ represents the instantaneous sol volume in the reservoir (i.e., $V_{sol}(t=0)-(F_{out}-F_{in})t$). The results of these calculations were subsequently used to determine the time-dependent mole fraction, $R_{MTMOS}(t) = C_{MTMOS}(t)/(C_{MTMOS}(t) + C_{TMOS}(t))$, of MTMOS in the sol. Figure 6.1 plots these results for different MTMOS sol concentrations (i.e., for 1:10, 1:20 and 1:40 MTMOS sols). As shown in the figure, different recipes are expected to yield sols of slightly different compositions, suggesting that gradients having different compositional properties can be prepared.

### *6.3.2 Optical Inspection of Films*

Optical inspection was employed to judge the overall quality of the gradient films obtained. Figure 6.2A shows a representative photograph of a gradient on a sublayer-coated silicon substrate. This particular film was derived from a 1:10 MTMOS sol. It is 1.3 cm wide and the gradient is 1.8 cm in length. It is most noteworthy that a general trend from dark to light is observed from top to bottom along the gradient film. Colorful interference lines are also observed. These run across the film (i.e. perpendicular to the gradient dimension) and appear at "random" locations along the gradient. Observation of the sol during dip-coating indicated that the sol surface was free from any vibrations that might cause such lines. Furthermore, films deposited without stirring also exhibited interference lines, indicating sol motions induced by

stirring played no role in their appearance. Since gradient deposition was performed on a pneumatic vibration isolation table and in a closed Plexiglas chamber, it is unlikely that mechanical vibrations and air currents caused these lines. Extensive additional studies performed with a conventional dip-coater suggest the appearance of these lines is directly related to the sol deposition mechanism and therefore cannot be easily eliminated. The deposition mechanism and the appearance of the interference lines will be discussed further, below. Here, it is sufficient to note that film thickness variations as small as a few tens of nanometers[246] can result in color changes similar to those observed.

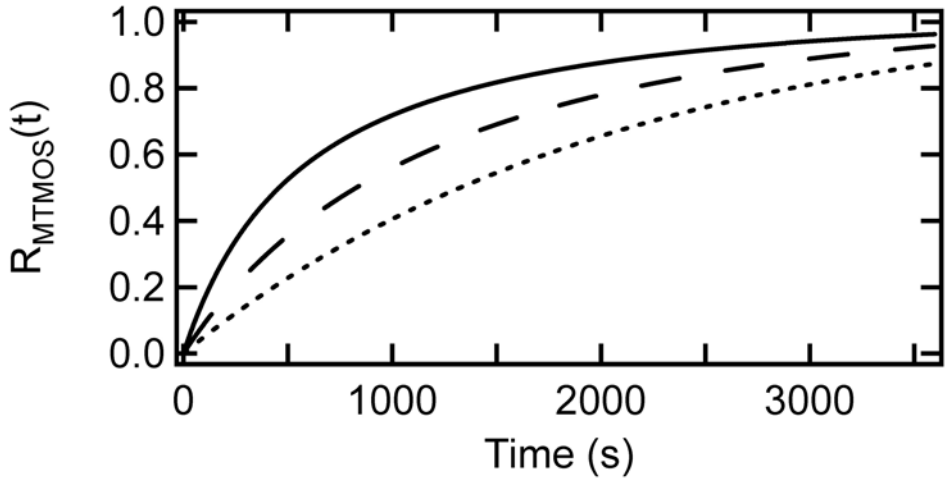


**Figure 6.1.** Plots of time-dependent $R_{MTMOS}(t)$ for 1:10 (solid line), 1:20 (dashed line) and 1:40 (dotted line) MTMOS sols.

### *6.3.3 Film Thickness and Surface Roughness*

The thicknesses of the TMOS sublayers and gradient films were determined using spectroscopic ellipsometry. Film thickness was measured at 1 mm intervals both before and after gradient deposition in approximately the same locations (i.e. within ±0.2 mm) in each case. Subtraction of the full film thickness from that of the sublayer allowed the gradient layer

thickness to be obtained. Figure 6.2 shows representative position-dependent thickness data acquired from a 1:10 MTMOS gradient. Shown are thickness values for the overall film, the TMOS sublayer and the gradient itself. These data show that the TMOS sublayer is relatively uniform across the substrate and ~ 180 nm thick. The gradient film, however, shows a clear decrease in average thickness along the gradient dimension. In this sample, the film thickness is greatest at the top of the gradient, yielding a value of 190 nm and gradually decreases to 40 nm thick at the bottom. Gradients prepared from 1:20 and 1:40 MTMOS sols showed the same film thinning trends (Figure 6.3). These additional data show that more concentrated MTMOS sols produce films of slightly greater thickness, as expected. Film thinning could be due to differences in the wettability of the sublayer to the time-varying mixed sol. It could also result from differences in the degrees of hydrolysis and condensation in the TMOS and MTMOS sols and/or differences in the rates at which these two precursors attach to the sublayer. Future investigations will seek to better understand this behavior.

Surface roughness was determined by profilometry. Representative roughness data for a gradient prepared from a 1:10 MTMOS sol is shown in Figure 6.4 These data depict surface roughness of ~ 11 nm (root mean square, RMS). The roughness is dominated by features separated by ~ 6 mm (on average) and running across the film. These features correspond well with the lines observed in the optical images, indicating the height (i.e. film thickness) variations observed are the cause of the colorful interference lines.

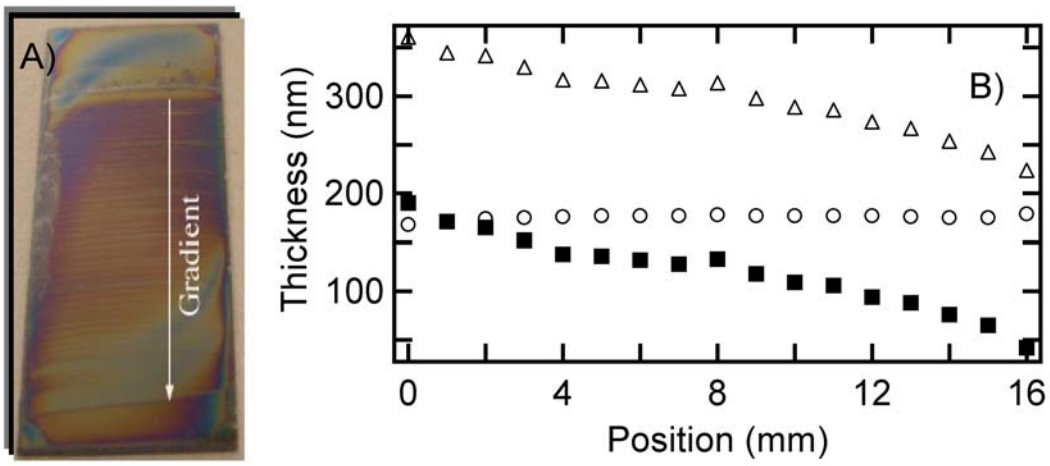


**Figure 6.2.** A) Photograph of gradient silicon wafer sample on a TMOS sublayer, B) position-dependent thickness for a gradient prepared by "infusion-withdrawal dip-coating" in 1:10 sample. Open triangles, overall film thickness; open circles, thickness of TMOS-coated substrate; Solid squares, thickness of gradients.

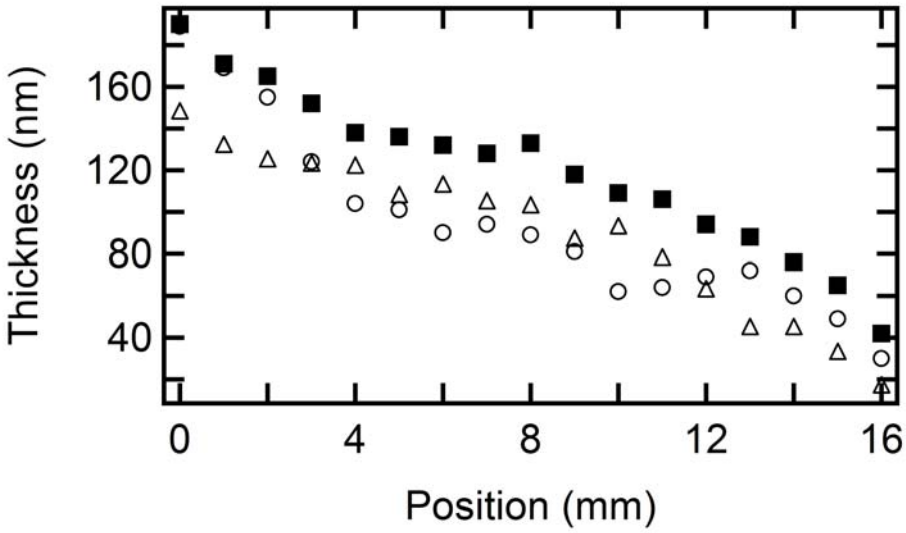


**Figure 6.3.** Position-dependent thickness for three gradients prepared by "infusion-withdrawal dip-coating". Shown are data from 1:40 (open triangles), 1:20 (open circles) and 1:10 (solid squares) MTMOS gradients.

The exact origins of the randomly-positioned, but reproducible film thickness variations and interference lines are unknown at present. However, after extensive experimentation and

consideration of published literature, it is believed that they result from a combination of the sol deposition mechanism described by Brinker[60,247] and the pinning and release (i.e., stick-slip) of the sol contact line with the substrate surface.[248]

As described by Brinker, and coworkers[60,247] sol deposition during dip-coating occurs primarily in the upper regions of the meniscus formed at the sol-substrate-air interface. In this region, evaporation of solvent (primarily ethanol)[60] and capillary flow[249] lead to concentration of the silica precursors and water at the top of the meniscus.[247] As a result of the high silica and water concentrations, hydrolysis and condensation, and hence, silica deposition occur most rapidly in this region. Relatively little silica deposits on the substrate from the bulk of the sol.

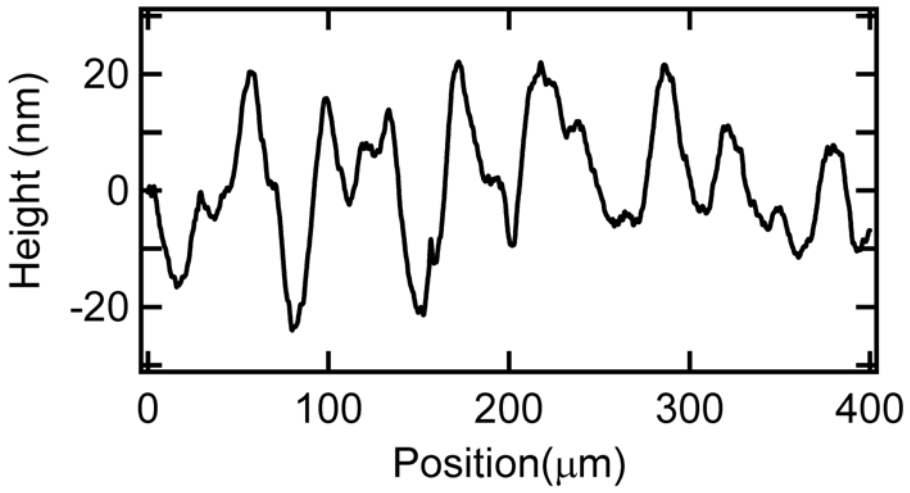


**Figure 6.4.** Surface roughness of a 1:10 MTMOS gradient prepared by "infusion-withdrawal dip-coating" and obtained by profilometry.

It is commonly expected that the meniscus recedes down the substrate at a uniform rate. However, the contact line between the sol and substrate may become briefly pinned at a fixed location, later releasing and rapidly dropping to a new location where it is again pinned. Such a "stick-slip" process provides a mechanism for delivery of varying quantities of silica precursor to the substrate surface during "infusion-withdrawal dip-coating." "Stick-slip" processes of this

type have recently been used in contact-line printing experiments for controlled placement and organization of nanomaterials.[248] It is believed this same process leads to the small variations in film thickness (i.e. the interference lines) observed in the present silica film gradients. Based on this model, and after extensive experimentation, we have concluded that ~ 11 nm RMS roughness on 100 μm length scales is the best that can be achieved using dip-coating methods.

### *6.3.4 Fluorescence Measurements of Film Polarity*

The primary objective of the present work is to produce silica films incorporating polarity gradients. Polarity along the gradient direction in films prepared as described above was probed by entrapping the solvent-sensitive dye NR in the film.[79,99,101,102] NR has been used in the past to probe the polarity properties of a wide range of liquid and solid environments. It is one of the most solvent sensitive fluorescent probes, exhibiting a dramatic bathochromic shift (of ~ 100 nm) in its emission spectrum between nonpolar (i.e., hexane) and polar (i.e., water) solvents.[102] In the present experiments, NR was doped into both gradient and spin cast silica films at ~ 1 μM concentrations.

*NR Emission from Nongradient Films.* NR emission spectra were initially recorded for a series of nongradient TMOS and MTMOS films. These experiments provided valuable information on the NR emission characteristics for films of different polarities. Emission spectra were first acquired from single-component, nongradient films that had been spin cast onto clean coverslips. The fluorescence emission maxima for TMOS and MTMOS derived films appeared at ~ 650 nm and ~ 605 nm, respectively, reflecting the significant polarity differences of these films.

A series of one- and two-component, nongradient silica films prepared on sublayer-coated substrates from sols containing different mole fractions of TMOS and MTMOS were also

characterized. Films derived from 0%, 20%, 40%, 60%, 80% and 100% MTMOS sols (relative to total silane) were investigated. In comparison to the above films, the corresponding TMOS and MTMOS derived films (0% and 100% MTMOS) cast on TMOS sublayers yielded emission maxima at 643 nm and 615 nm, respectively. Comparison of the MTMOS results obtained with and without the sublayer indicate that little of the NR penetrated into the TMOS sublayer. It is therefore concluded that the NR emission spectra primarily reflect the polarity properties of the silica layer deposited on top of the TMOS sublayer.

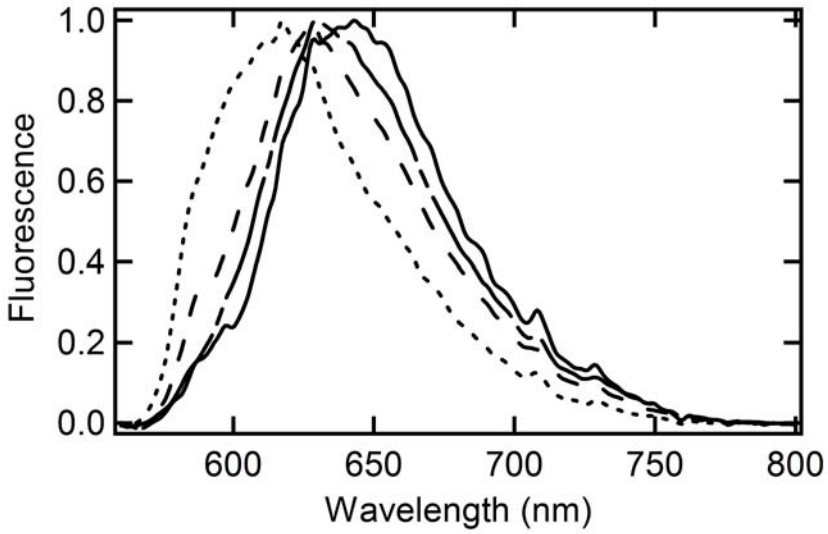


**Figure 6.5.** NR spin coated spectrum with different MTMOS molar fraction (0%, 20%, 60%, 100%). The spectra shown have been smoothed.

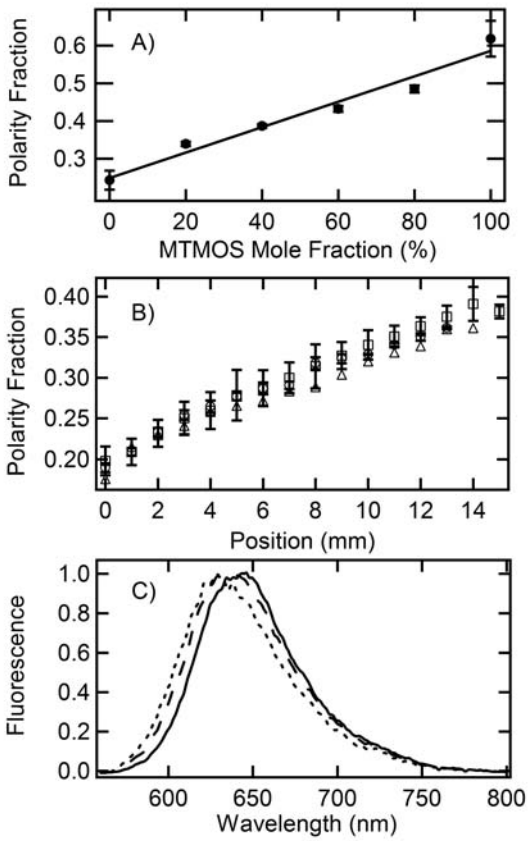


**Figure 6.6.** A) MTMOS polarity fraction (PF value) as a function of MTMOS mole fraction for one and two-component nongradient (spin-coated) films. The solid line has been appended to better depict the trend in the data. B) MTMOS polarity fraction as a function of position for gradient samples. The top of the gradient corresponds to 0 mm. Shown are data from 1:10 (open squares), 1:20 (open triangles) and 1:40 (open circles) MTMOS gradients. C) Representative NR fluorescence spectra (normalized) for a 1:10 MTMOS gradient taken from the top (solid line), middle (dashed line) and bottom (dotted line) of the gradient.

The emission spectra obtained as a function of MTMOS mole fraction in the spin cast films provides a clear view of the hypsochromic shift exhibited by NR upon a change from TMOS-derived films to MTMOS-derived films. Figure 6.5 shows NR fluorescence spectra obtained from several different films prepared using different mole fractions of MTMOS. In order to more quantitatively assess the polarity characteristics observed for films prepared using

different TMOS and MTMOS mole fractions, a "polarity fraction" (PF) was defined. PF was calculated directly from the NR emission spectra by measuring the average NR fluorescence in 10 nm wide bands centered at 605 nm (reflecting nonpolar environments) and 650 nm (polar environments) and determining the fraction of the total emission that occurred in the 605 nm band. Therefore, PF is expected to increase with increasing methyl content of the films. PF values of 0.25 and 0.60 were obtained for nongradient (spin cast) TMOS and MTMOS films (without sublayers), respectively.

Figure 6.6A plots the PF values obtained as a function of MTMOS molar fraction in films spin cast onto TMOS-sublayer-coated substrates. A monotonic and nominally linear increase from 0.25 to 0.48 is observed in the PF value as the mole fraction of MTMOS in the original sol increases from 0% to 80%. The large error bar for the 100% MTMOS film is believed to result from increased film roughness due to decreased sublayer wettability.

*NR Emission from Gradient Films.* NR spectra recorded from the gradient films clearly demonstrate the presence of a polarity gradient. The PF values obtained as a function of position along each of three different gradients are plotted in Figure 6.6B. Representative NR fluorescence spectra are shown in Figure 6.6C. All show a clear monotonic increase in PF from the top of the film (0 mm) to the bottom. The PF values obtained from the gradients are somewhat smaller than those of the spin coated films. For example, the 1:10:4 gradient exhibits an initial PF of 0.19, while a spin coated 0% MTMOS (100% TMOS) film yields 0.24. At the other end of the same gradient, a PF of 0.39 is obtained, while spin coated 80% MTMOS film yields 0.49. These results suggest the gradient films are slightly more polar than the spin coated films. Differences in these films are likely a result of differences in the sol-gel process in each case. Condensation and solvent evaporation occur rapidly and simultaneously in the spin coated

films, while they occur more slowly in the dip-coated samples. In addition, the higher concentration of water expected in the deposition region (upper part of the meniscus) in dip-coated films may lead to greater incorporation of water in the final films, making them appear more polar. Nevertheless, all three gradients show PF values that are similar to those of the spin coated films, suggesting similar variations in the methyl content of the gradients.

Interestingly, all three gradients show almost identical PF values (within experimental error) along the gradient dimension. As shown in Figure 6.1, the compositions of the sol mixtures from which the films were grown are expected to be distinctly different, with higher MTMOS concentrations leading to greater methyl content at intermediate times. Such differences in the sol composition would be expected to appear in the final films as well, with greater methyl content observed in intermediate gradient regions, when relatively high concentration MTMOS sols are employed. The apparent insensitivity of the gradients to MTMOS concentration is again attributable to the details of silica deposition. Differences in the MTMOS sols arise primarily from dilution with ethanol. Since ethanol evaporation occurs efficiently from the top of the meniscus,[60] the concentration of silica precursor in the deposition region is likely more similar than otherwise expected from the composition of the original sol. As a result, little dependence of the final film properties on sol concentration is observed.

### *6.3.5 Water Contact Angle*

Additional evidence for the formation of silica film gradients was obtained from water contact angle measurements.[205-208] The incorporation of methyl groups in sol-gel materials derived from MTMOS makes them much more hydrophobic than those prepared from TMOS. Water contact angle measurements, therefore, provide valuable information on the extent of methyl modification and the spatial variations therein expected for gradients.

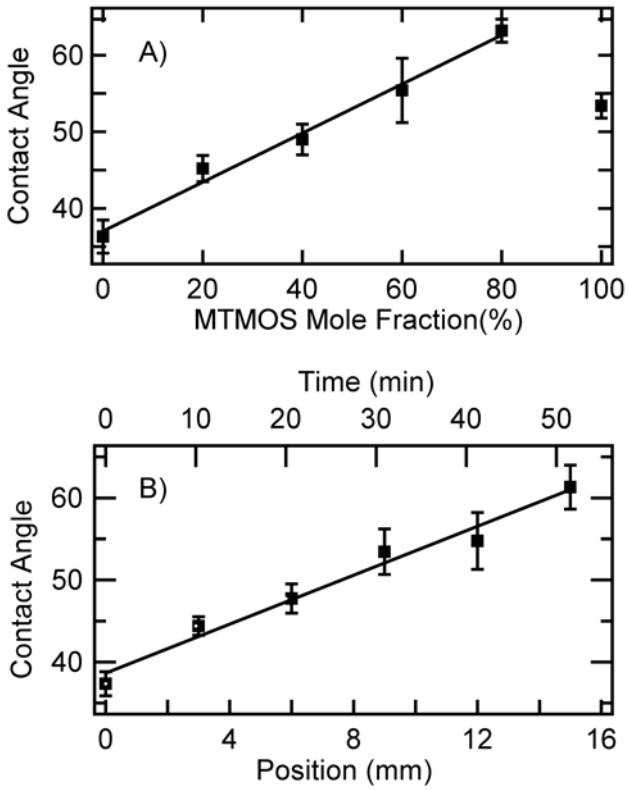


**Figure 6.7.** Contact angle in degrees for A) one- and two-component nongradient (spin coated) films and B) a 1:40 MTMOS gradient, both on TMOS sublayer-coated substrates. The gradient data is plotted as a function of position (lower axis) and approximate time during deposition (upper axis). The solid lines have been added to better depict trends in the data. The error bars show the standard deviations obtained from multiple measurements performed on each sample.

As in the fluorescence measurements described above, variations in the contact angle attributable to methyl modification were initially explored for spin coated films prepared from sols of differing MTMOS and TMOS mole fractions. These results are plotted in Figure 6.7A. A monotonic increase in water contact angle was observed for films derived from 0% to 80% MTMOS sols. For pure TMOS, the water contact angle was 36$^{o}$, while for pure MTMOS, it was 63$^{o}$. The deviation from the observed trend near 100% MTMOS is attributed to a decrease in film homogeneity and an associated increase in roughness.

Water contact angles were measured as a function of position along each of the silica film gradients. Figure 6.7B plots representative position dependent water contact angle results for a 1:40 gradient. The plot is very similar to that obtained from the spin coated films, exhibiting similar contact angles at the top of the gradient ($37^{o}$), and at the bottom ($61^{o}$), and the same monotonic trend. Data obtained on 1:10 films were indistinguishable from those obtained from 1:40 films. These results provide strong supporting evidence for the presence of a polarity gradient resulting from spatial variations in the methyl content of the films. While variations in surface roughness cause variations in contact angle (see above), such effects were deemed insignificant in the present gradients, based on the profilometry data and predictions of sol composition (see Figure 6.1), which never reach 100% MTMOS.

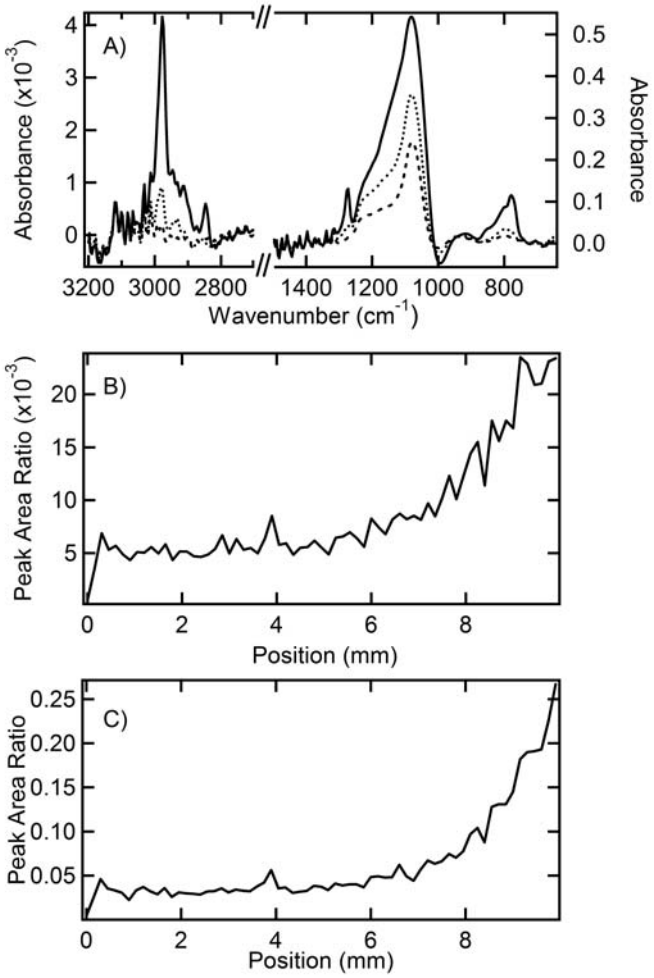


**Figure 6.8.** A) Representative FTIR spectra acquired from the bottom (solid line), middle (dotted line) and top (dashed line) of a gradient sample. As expected, the methyl vibration is strongest near the bottom of the gradient. B) Ratio of the $CH_3$ and Si-O-Si absorption peak areas (see text) as a function of position (top-middle) for a 1:40 MTMOS gradient. C) Ratio of the $CH_3$ and Si-OH absorption peak areas as a function of position (top-middle) for a 1:40 MTMOS gradient. The Si-OH data was obtained by integrating the peak area for the Si-OH vibration found in the 875-1000 $cm^{-1}$ region.

### *6.3.6 FTIR Results*

Vibrational spectroscopy provides a direct means for detecting the $CH_3$ functional groups in MTMOS-derived silica films and for determining methyl content, relative to total silica. Unfortunately, conventional FTIR measurements do not afford the spatial resolution necessary to monitor film methyl content along gradient materials. Here, an FTIR microscope configured to operate in transmission was employed to acquire spatially-resolved IR spectroscopic data (~ 150 μm spatial resolution) on the gradient samples.

IR spectra of both gradient and nongradient silica films were acquired. All such films were prepared on silicon substrates. Clean silicon substrates and TMOS-sublayer coated silicon substrates were both used as blanks in the various experiments. In a typical IR spectrum of an MTMOS-derived silica film, the $CH_3$ groups produced a small, but detectable peak in the 2950-3000 $cm^{-1}$ range. The Si-O-Si stretch produced a very large peak in the 1000-1200 $cm^{-1}$ range.[22] The ratio of these two peak areas (i.e., $CH_3$/Si-O-Si) was used as a measure of the methyl content of the films along the gradient, relative to total silica. Data obtained from the Si-OH vibration is also presented in Figure 6.8C and shows the same trend. Figure 6 shows representative position-dependent data acquired from a 10 mm segment (top-middle) along a 1:40 MTMOS gradient. The data shown represent the maximum distance over which the instrument could map sample absorbance without manually repositioning the sample. As shown in the plot, the methyl content clearly increases as a function of position down the gradient. The functional form of this plot differs from the NR fluorescence and contact angle data because of the different and complex sensitivities of these different methods to film composition. For example, the 1000-1200 $cm^{-1}$ region of the spectrum incorporates contributions from both Si-O-Si and Si-O-$CH_3$ vibrations, making this region sensitive to both the degree of hydrolysis and total silica content. The IR mapping data also infrequently exhibits some unexpected variations. Some of these variations

reflect the low signal-to-noise ratio for the $CH_3$ peak. Others arise from defects sometimes observed in the films. These defects are attributed to occasional, inadvertent contamination of the substrates and/or sublayer-coated substrates prior to gradient deposition. Nevertheless, the IR mapping data provides strong supporting evidence for the presence of a polarity gradient produced by a gradient in the methyl content of the film.

## 6.4 Conclusions

Silica thin films incorporating polarity gradients have been prepared for the first time using an unique "infusion-withdrawal dip-coating" procedure. The gradient is formed by immersing a substrate into a sol whose composition is varied as a function of time in a controlled fashion. Silica films incorporating spatially varying properties are deposited as the sol is withdrawn down the substrate surface. Results from fluorescence spectroscopy, contact angle measurements, and FTIR microscopy prove that the films obtained incorporate polarity gradients derived from increasing concentrations of methyl-modified silica along the length of the film. While in this work sols of time varying TMOS and MTMOS content were used to form polarity gradients on glass slides and silicon wafers, it is anticipated that the infusion-withdrawal dip-coating procedure described herein could be used with nearly any combination of organoalkoxysilanes to prepare gradients whose composition/functionality gradually changes across the film. Polarity gradients like those prepared herein have a variety of potential applications as stationary phases for chemical separations, as solid supports for combinatorial catalysis and as supports for biological sensors. The continued development of sol-gel methods for producing silica film gradients will provide new routes to unique thin film materials of spatially controlled chemical and physical properties. Future studies of these gradients will

include investigations of the nanoscale characteristics of the gradients through application of single molecule spectroscopic methods.[250]

# CHAPTER 7 - Conclusions and Future Directions

## 7.1 Conclusions

In summary, single molecule spectroscopy has been used to probe the interaction between single dye molecules and the silica matrix in mesoporous materials (Chapter 3). A model to determine the actual dye concentration in the single molecule experiments has been presented and verified to be correct by both simulation and experiment results (Chapter 4). Single point correlation spectroscopy was used to follow the formation of thin macroporous monoliths of MTMOS-derived materials from before phase separation to well after gelation at the single-pore/single-nanoparticle level (Chapter 5). Finally, bulk method for preparing silica thin film polarity gradients was developed (Chapter 6). The following several paragraphs give much more detailed conclusions from this work.

In Chapter 3, significant new information on mass transport and molecule-matrix interactions in mesoporous thin-film systems was obtained using single molecule spectroscopic methods. Three different dyes of varying size, charge, and hydrophilicity were used. Neutral NR molecules were found to be highly mobile in surfactant-containing films, regardless of the level of film hydration, while also showing strong evidence for reversible adsorption to the silica surface. It was concluded NR spends much of its time diffusing through the nonpolar, hydrated regions of the surfactant micelles, but also comes in periodic contact with the silica surface, to which it can reversibly bind. In contrast, anionic SPDI molecules were found to be immobile under all conditions studied in CTAB-containing films, due to extremely strong ionic interactions between SPDI and the oppositely charged surfactant. In addition, cationic DiI molecules were found to exhibit dramatic humidity-dependent mobilities and also showed

evidence for reversible surface adsorption. DiI was concluded to be incorporated in the surfactant micelles and to form strong ionic bonds with the negatively charged silica surface. Studies performed in SDS-containing films provided further support for these conclusions. Overall, results from the surfactant-containing films are consistent with those of previous studies in which molecule-matrix interactions were probed by bulk-spectroscopic means. Unlike these previous studies, however, the present results also provide relevant new information on mass transport through the films, evidence of reversible surface adsorption, and quantitative information on variations in these phenomena with film hydration.

The above-mentioned single molecule studies have given detailed information on chemical interactions between single molecules and the silica matrix. However, the actual dye concentration in the focal volume in these experiments was largely unknown. It's important to know the actual dye concentration because the potential applications of those silica materials (separation media, catalysts and sensors) require a full understanding of how the molecules partition between different environments. Unfortunately, the classic equation which is used to determine the number of molecules in the detection volume neglects some important details. Specifically, it neglects the possibility that orientationally-fixed (i.e. adsorbed) molecules might be present. As shown in Chapter 4, the molecule orientation must be fully considered in the determination of concentration. Therefore, a model describing the full concentration dependent amplitude of fluorescence autocorrelation data for samples comprised of single molecules entrapped in fixed but random orientations and exhibiting polarization dependent excitation and emission was presented. The model was verified using both simulated and experimental single molecule data. It differs from previously published models, which assume polarization-independent excitation or emission processes. The results proved that the exact nature of

molecular orientation (fixed or rapidly reorienting) must be accounted for when determining concentrations (or relative concentrations) from single molecule autocorrelation data. All other parameters being equal, it may be concluded that fixed molecules contribute approximately twice as strongly to the autocorrelation decay as do rapidly reorienting molecules. The orientation-dependence of autocorrelation amplitudes described here is relevant to concentration determinations in any system comprised of small objects (i.e. single molecules, nanoparticles, etc.) that exhibit polarization-dependent excitation or emission processes and which may be found in fixed orientations on relevant experimental time scales. Although this dependence was demonstrated using single molecule imaging results alone, it is also of importance to the interpretation of autocorrelation data from studies of reversible single molecule adsorption in/on thin films or surfaces, such as have been reported by our group and by others.

In a typical single molecule experiment, appropriate dyes (such as, NR, DiI and SPDI) are employed. However, all such dyes photobleach under long exposure to excitation light. The use of dyes can be avoided by employing nanoparticles and light scattering phenomena as a means to probe materials properties. In Chapter 5, the use of native silica nanoparticles to probe macroporous silica films was described. An optical microscopy was used to directly observe phase separation and gelation in macroporous MSQ films formed from MTMOS under low pH conditions. When coupled with *in situ* single-site confocal correlation spectroscopy and scanning electron microscopy, valuable information on film morphology and the growth of MSQ nanoparticles in the liquid filled pores of the MSQ matrix was obtained. It was found that the MSQ nanoparticles grew to a maximum diameter of ~ 30 nm soon after film preparation and remained in this size range until well after gelation. Nanoparticle size stabilization was attributed to consumption of reactive MSQ species, to a condensation-induced decrease in

nanoparticle surface reactivity, and to a decrease in the collision rate of the MSQ particles as they grow. Incorporation of some nanoparticles in/on the matrix commenced shortly after gelation, as evidenced by a time-dependent decrease in the number of particles present in the pores. In contrast, the onset of particle-particle reactions within the individual pores was delayed for approximately three hours after gelation, at which time a significant time-dependent decrease in the nanoparticle diffusion coefficient was observed. Nanoparticle growth in this later phase was attributed to particle aggregation after a further evolution of their properties. In addition, the ability to probe macroporous sol-gel derived films at the single pore level by optical microscopic methods will pave the way to a deeper fundamental understanding of the phase separation, gelation and aging processes in these technologically important materials. Extensions of these methods will also allow for a better understanding of phenomena such as hindered diffusion within the macropores and molecule-matrix interactions in chemical or biomolecule separations.

Finally, silica films incorporating polarity gradients have been produced for the first time and were described in Chapter 6. These films were prepared using the newly developed method of "infusion-withdrawal dip-coating". Fluorescence methods were employed to detect the presence of the polarity gradients. The NR emission spectrum was recorded as a function of position along the gradient and compared to results obtained from spin coated sol-gel films incorporating different mole fractions of methyl-modified silica. A blue shift in NR emission was observed as a function of position along the gradient dimension. These results provide strong evidence for the presence of polarity gradients in the films, produced by a gradual increase in methyl-modified silica content. Water contact angle data was used to obtain supporting evidence for the presence of the polarity gradients. The results depicted a monotonically increasing contact angle as a function of position, consistent with increasing

methyl content towards the bottom of the gradients. FTIR results demonstrated that the concentration of $CH_3$ functional groups, relative to total silica (as measured via the Si-O-Si absorption band), increases down the film. In all, the NR fluorescence results, water contact angle data and FTIR microscopy data prove that the films prepared by "infusion-withdrawal dip-coating" using sols of time varying TMOS and MTMOS content are polarity gradients and are dominated by polar TMOS-derived silica at the top and by nonpolar MTMOS-derived silica at the bottom of the gradients.

## 7.2 Future Directions

Single molecule spectroscopy has been shown to be useful in probing the properties of silica materials. It has specifically been used to investigate mass transportation within silica media and chemical interactions between single molecules and the silica matrix. A few additional experiments might be achieved based on the research described in this thesis.

First, as mentioned in Chapter 3, both CTAB and SDS were added to the silica sol to prepare silica films with different pore size and structure and pore properties (charge, hydrophobicity). Such surfactant-templated pores are extremely important for the use of silica materials in chemical separations, sensors and catalysts, because they are all for mass transport and provide potential interaction sites. Other surfactants can be used to change the pore properties (i.e., pore size, pore structure, type of charge, etc ), which includes anionic surfactants (i.e. perfluorooctanesulfonate), cationic surfactants (i.e. cetylpyridinium chloride ) and nonionic surfactants (i.e. alkylphenol poly(ethylene oxide)). The resultant dye-doped silica films containing one of those surfactants will show different mass transport phenomena and different interactions between dye dopants and matrix. These studies will help to fully understand the

properties of the surfactant-containing silica materials and to optimize their properties for their potential applications.

Second, as shown in Chapter 6, silica film gradients have been prepared from TMOS and MTMOS sol mixtures. Their properties were probed entirely by bulk spectroscopic and physical methods. Since silica films studied for this thesis have exhibited extensive local heterogeneity, single molecule studies are then necessary to probe the current gradient by doping a proper dye (i.e. Nile Red) with extremely low concentration (~0.5nM) into the film. Detailed information of the nanoscale characteristics (such as, the presence of nanoscale domains) along the gradients will be provided to better understand and apply the gradient. Since impurities are almost routinely found in single molecule experiments, absolute care must be taken to avoid contamination with solvents and the silica precursors might need to be purified by distillation.

In addition, since we have prepared good and uniform silica thin films with polarity gradients, other gradients might also be achieved by using the same or similar "infusion withdrawal dip-coating" methods. For example, a porosity gradient may be prepared by gradually infusing an acid-catalyzed TMOS sol into a base-catalyzed TMOS sol. The resulting films will likely be useful as stationary phases for separations science. Another polarity gradient might be achieved by adding an APTEOS sol into an MTMOS sol. Such an amine gradient surface can be used to develop other gradient materials by subsequent surface reaction. A pH gradient may also be prepared by applying two different TMOS sols (one base-catalyzed, the other acid-catalyzed). Such films may be useful in pH sensing. Besides the above mentioned silica gradients, organic polymer gradients might also be prepared by using "infusion-withdrawal dip-coating" method. For example, gradient in this case could be prepared by gradually infusing a poly(styrene) (PSt) solution into a poly(methyl methacrylate) (PMMA) solution to make

polymer gradient with gradually increasing ratio of PSt/PMMA. Such a gradient would start with a really soft material (PMMA) and end with hard material (PSt).

## References


(1) Avnir D.; Coradin T.; Lev O.; Livage J. *J. Mater. Chem.* **2006**, *16*, 1013.

(2) Jeronimo P. C. A.; Araujo A. N.; Montenegro M. *Talanta* **2007**, *72*, 13.

(3) Kandimalla V. B.; Tripathi V. S.; Ju H. X. *Crit. Rev. Anal. Chem.* **2006**, *36*, 73.

(4) Frenzer, G.; Maier, W. F. *Annu. Rev. Mat. Res.* **2006**, *36*, 281.

(5) Schubert, U. *New J. Chem.* **1994**, *18*, 1049.

(6) Colon, L. A.; Maloney, T. D.; Anspach, J.; Colon H. *Adv. Chroma.* **2003**, *42*, 43.

(7) Siouffi, A. M. *J. Chroma. A* **2003**, *1000*, 801.

(8) Li, W.; Fries, D. P.; Malik, A. *J. Chroma. A* **2004**, *1044*, 23.

(9) Petit-Dominguez, M. D.; Shen, H.; Heineman, W. R.; Seliskar, C. J. *Anal. Chem.* **1997**, *69*, 703.

(10) Wei, H.; Collinson, M. M. *Anal. Chim. Acta* **1999**, *397*, 113.

(11) Innocenzi, P.; Lebeau, B. *J. Mater. Chem.* **2005**, *15*, 3821.

(12) Liu, H.; Wu, Y. P.; Rahm, E.; Holze, R.; Wu, H. Q. *J. Solid State Electrochem.* **2004**, *8*, 450.

(13) Long, J. W.; Dunn, B.; Rolison, D. R.; White, H. S. *Chem. Rev.* **2004**, *104*, 4463.

(14) Brinker, C. J.; Scherer, G. W. *Sol-Gel Science: The Physics and Chemistry of Sol-Gel Processing*; Academic Press: Boston, 1990.

(15) Hench, L. L.; West, J. K. *Chem. Rev.* **1990**, *90*, 33.

(16) Carturan G.; Dal Toso R.; Boninsegna S.; Dal Monte R. *J. Mater. Chem.* **2004**, *14*, 2087.

(17) Dunn, B.; Zink, J. I. *Acc. Chem. Res* **2007**, *40*, 747.

(18) Brennan, J. D. *Acc. Chem. Res.* **2007**, *40*, 827.

(19) Pagliaro M.; Ciriminna R.; Palmisano G. *Chem. Soc. Rev.* **2007**, *36*, 932.

(20) Sanchez, C.; Julian, B.; Belleville, P.; Popall, M. *J. Mater. Chem.* **2005**, *15*, 3559.

(21) Collinson, M. M. *Trends in Anal. Chem.* **2002**, *21*, 30.

(22) Pagliaro, M.; Ciriminna, R.; Man, M. W. C.; Campestrini, S. *J. Phys. Chem. B* **2006**, *110*, 1976.

(23) Sanchez, S.; Ribot, F. *New J. Chem.* **1994**, *18*, 1007.

(24) Schmidt, H. *J. Sol-Gel Sci. and Tech.* **1994**, *1*, 217.

(25) Schubert, U.; Hüsing, N.; Lorenz, A. *Chem. Mater.* **1995**, *7*, 2010.

(26) Walcarius, A.; Mandler, D.; Cox, J.; Collinson, M. M.; Lev, O. *J. Mater. Chem.* **2005**, *15*, 3663.

(27) Wen, J.; Wilkes, G. L. *Chem. Mater.* **1996**, *8*, 1667.

(28) Nicole, L.; Boissiere, C.; Grosso, D.; Quach, A.; Sanchez, C. *J. Mater. Chem.* **2005**, *15*, 3598.

(29) Bonhomme, C.; Coelho, C.; Baccile, N.; Gervais, C.; Azais, T.; Babonneau. *Acc. Chem. Res.* **2007**, *40*, 738.

(30) Hüsing, N.; Schubert, U.; Misof, K.; Fratzl, P. *Chem. Mater.* **1998**, *10*, 3024.

(31) Lu, Y.; Cao, G.; Kale, R. P.; Prabakar, S.; Lopez, G. P.; Brinker, C. J. *Chem. Mater.* **1999**, *11*, 1223.

(32) Rivera, D.; Harris, J. M. *Anal. Chem.* **2001**, *73*, 411.

(33) Collinson, M. M. *Acc. Chem. Res.* **2007**, *40*, 777.

(34) Avnir, D. *Acc. Chem. Res.* **1995**, *28*, 328.

(35) Dunn, B.; Zink, J. I. *Chem. Mater.* **1997**, *9*, 2280.

(36) Dunn, B.; Zink, J. I. *J. Mater. Chem.* **1991**, *1*, 903.

(37) Keeling-Tucker, T.; Brennan, J. D. *Chem. Mater.* **2001**, *13*, 3331.

(38) Higgins, D. A.; Hou, Y. Single Molecule Spectroscopy Studies to Characterize Nanomaterials. In *Encyclopedia of Nanoscience and Nanotechnology*; Schwartz, J. A., Contescu, C., Putyera, K., Eds.; Marcel-Dekker: New York, 2004; pp 3575.

(39) Moerner, W. E. *J. Phys. Chem. B* **2002**, *106*, 910.

(40) Moerner, W. E.; Fromm, D. P. *Rev. Sci. Instrum.* **2003**, *74*, 3597.

(41) Tamarat, P.; Maali, A.; Lounis, B.; Orrit, M. *J. Phys. Chem. A* **2000**, *104*, 1.

(42) Higgins, D. A.; Collinson, M. M. *Langmuir* **2005**, *21*, 9023.

(43) Wirth, M. J.; Ludes, M. D.; Swinton, D. J. *Appl. Spectrosc.* **2001**, *55*, 663.

(44) Wirth, M. J.; Swinton, D. J. *Anal. Chem.* **1998**, *70*, 5264.

(45) Wirth, M. J.; Swinton, D. J. *J. Phys. Chem. B* **2001**, *105*, 1472.

(46) Wirth, M. J.; Swinton, D. J.; Ludes, M. D. *J. Phys. Chem. B* **2003**, *107*, 6258.

(47) Collinson, M. M. Structure, Chemistry, and Applications of Sol-Gel Derived Materials. In *Chalcogenide Glasses and Sol-Gel Materials*; Nalwa, H. S., Ed.; Academic Press, 2001; Vol. 5; pp 163.

(48) Dong, H.; Brennan, J. D. *Chem. Mater.* **2006**, *18*, 541.

(49) Zhang, K.; Yang, H. *J. Phys. Chem. B* **2005**, *109*, 21930.

(50) Beck, J. S.; Vartuli, J. C.; Roth, W. J.; Leonowicz, M. E.; Kresge, C. T.; Schmitt, K. D.; Chu, C. T.-W.; Olson, D. H.; Sheppard, E. W.; McCullen, S. B.; Higgins, J. B.; Schlenker, J. L. *J. Am. Chem. Soc.* **1992**, *114*, 10834.

(51) Kresge, C. T.; Leonowicz, M. E.; Roth, W. J.; Vartuli, J. C.; Beck, J. S. *Nature* **1992**, *359*, 710.

(52) Corma, A. *Chem. Rev.* **1997**, *97*, 2373.

(53) Hartmann, S.; Brandhuber, D.; Hüsing, N. *Acc. Chem. Res.* **2007**, *40*, 885.

(54) Alberius, P. C. A.; Frindell, K. L.; Hayward, R. C.; Kramer, E. J.; Stucky, G. D.; Chmelka, B. F. *Chem. Mater.* **2002**, *14*, 3284.

(55) Fu, Y.; Ye, F.; Sanders, W. G.; Collinson, M. M.; Higgins, D. A. *J. Phys. Chem. B* **2006**, *110*, 9164.

(56) Jung, C.; Kirstein, J.; Platschek, B.; Bein, T.; Budde, M.; Frank, I.; Muellen, K.; Michaelis, J.; Bräuchle, C. *J. Am. Chem. Soc.* **2008**, *130*, 1638.

(57) Ye, F.; Higgins, D. A.; Collinson, M. M. *J. Phys. Chem. C* **2007**, *111*, 6772.

(58) Jordan, J. D.; Dunbar, R. A.; Hook, D. J.; Zhuang, H.; Gardella, J. A.; Colon, L. A.; Bright, F. V. *Chem. Mater.* **1998**, *10*, 1041.

(59) Brinker, C. J.; Hurd, A. J.; Schunk, P. R.; Frye, G. C.; Ashley, C. S. *J. Non-Cryst. Solids* **1992**, *147/148*, 424.

(60) Brinker, C. J.; Frye, G. C.; Hurd, A. J.; Ashley, C. S. *Thin Solid Films* **1991**, *201*, 97.

(61) Mahurin, S. M.; Dai, S.; Barnes, M. D. *J. Phys. Chem. B* **2003**, *107*, 13336.

(62) Ambrose, W. P.; Moerner, W. E. *Nature* **1991**, *349*, 225.

(63) Orrit, M.; Bernard, J. *Phys. Rev. Lett.* **1990**, *65*, 2716.

(64) Julien, C.; Debarre, A.; Nutarelli, D.; Richard, A.; Tchenio, P. *J. Phys. Chem. B* **2006**, *110*, 3902.

(65) Ha, T. *Methods* **2001**, *25*, 78.

(66) Gilliland, J. W.; Yokoyama, K.; Yip, W. T. *Chem. Mater.* **2004**, *16*, 3949.

(67) Kirstein, J.; Platschek, B.; Jung, C.; Brown, R.; Bein, T.; Bräuchle, C. *Nat. Mater.* **2007**, *6*, 303.

(68) R. Gupta; Chaudhury, N. K. *Bios. & Bioe.* **2007**, *2007*, 2387.

(69) Anedda, A.; Carbonaro, C. M.; Clemente, F.; Corpino, R.; Ricci, P. C. *J. Phys. Chem. B* **2003**, *107*, 13661.

(70) Huang, M. H.; Soyez, H. M.; Dunn, B. S.; Zink, J. I. *Chem. Mater.* **2000**, *12*, 231.

(71) Narang, U.; Wang, R.; Prasad, P. N.; Bright, F. V. *J. Phys. Chem.* **1994**, *98*, 17.

(72) Cros, F.; Korb, J.-P.; Malier, L. *Langmuir* **2000**, *16*, 10193.

(73) Okazaki, M.; Toriyama, K. *J. Phys. Chem. B* **2003**, *107*, 7654.

(74) Shenderovich, I. G.; Buntkowsky, G.; Schreiber, A.; Gedat, E.; Sharif, S.; Albrecht, J.; Golubev, N. S.; Findenegg, G. H.; Limbach, H.-H. *J. Phys. Chem. B* **2003**, *107*, 11924.

(75) Stallmach, F.; Kärger, J.; Krause, C.; Jeschke, M.; Oberhagemann, U. *J. Am. Chem. Soc.* **2000**, *122*, 9237.

(76) Howells, A. R.; Zambrano, P. J.; Collinson, M. M. *Anal. Chem.* **2000**, *72*, 5265.

(77) Kanungo, M.; Collinson, M. M. *Anal. Chem.* **2003**, *75*, 6555.

(78) Gilliland, J. W.; Yokoyama, K.; Yip, W. T. *Chem. Mater.* **2005**, *17*, 6702.

(79) Bardo, A. M.; Collinson, M. M.; Higgins, D. A. *Chem. Mater.* **2001**, *13*, 2713.

(80) Hellriegel, C.; Kirstein, J.; Bräuchle, C.; Latour, V.; Pigot, T.; Olivier, R.; Lacombe, S.; Brown, R.; Guieu, V.; Payrastre, C.; Izquierdo, A.; Mocho, P. *J. Phys. Chem. B* **2004**, *108*, 14699.

(81) Kanungo, M.; Collinson, M. M. *Langmuir* **2005**, *21*, 827.

(82) Walcarius, A.; Delacote, C.; Sayen, S. *Electrochimica Acta* **2004**, *49*, 3775.

(83) Collinson, M. M.; Zambrano, P.; Wang, H.; Taussig, J. *Langmuir* **1999**, *15*, 662.

(84) Collinson, M. M.; Rausch, C. G.; Voigt, A. *Langmuir* **1997**, *13*, 7245.

(85) Dvorak, O.; De Armond, M. K. *J. Phys. Chem.* **1993**, *97*, 2646.

(86) Elson, E. L.; Magde, D. *Biopolym.* **1974**, *13*, 1.

(87) Qian, H.; Sheetz, M. P.; Elson, E. L. *Biophys. J.* **1991**, *60*, 910.

(88) Schmidt, T.; Schuetz, G. J.; Baumgartner, W.; Gruber, H. J.; Schindler, H. *Proc. Nat. Acad. Sci. USA* **1996**, *93*, 2926.

(89) Hellriegel, C.; Kirstein, J.; Bräuchle, C. *New. J. Phys.* **2005**, *7*, 1.

(90) McCain, K. S.; Hanley, D. C.; Harris, J. M. *Anal. Chem.* **2003**, *75*, 4351.

(91) Jung, C.; Mueller, B. K.; Lamb, D. C.; Nolde, F.; Muellen, K.; Bräuchle, C. *J. Am. Chem. Soc.* **2006**, *128*, 5283.

(92) Martin-Brown, S. A.; Fu, Y.; Saroja, G.; Collinson, M. M.; Higgins, D. A. *Anal. Chem.* **2005**, *77*, 486.

(93) Jung, C.; Hellriegel, C.; Michaelis, J.; Bräuchle, C. *Adv. Mater.* **2007**, *19*, 956.

(94) Zuerner, A.; Kirstein, J.; Doeblinger, M.; Bräuchle, C.; Bein, T. *Nature* **2007**, *450*, 705.

(95) Sakamoto, Y.; Kaneda, M.; Terasaki, O.; Zhao, D. Y.; Kim, J. M.; Stucky, G.; Shin, H. J.; Ryoo, R. *Nature* **2000**, *408*, 449.

(96) Avnir, D.; Braun, S.; Lev, O.; Levy, D.; Ottolenghi, M. Organically Doped Sol-Gel Porous Glasses: Chemical Sensors, Enzymatic Sensors, Electrooptical Materials, Luminescent Materials and Photochromic Materials. In *Sol-Gel Optics Processing and Applications*; Klein, L. C., Ed.; Kluwer Academic Publications: Massachusetts, 1994; pp 539.

(97) McCain, K. S.; Schluesche, P.; Harris, J. M. *Anal. Chem.* **2004**, *76*, 939.

(98) McCain, K. S.; Harris, J. M. *Anal. Chem.* **2003**, *75*, 3616.

(99) Higgins, D. A.; Collinson, M. M.; Saroja, G.; Bardo, A. M. *Chem. Mater.* **2002**, *14*, 3734.

(100) Brennan, J. D.; Hartman, J. S.; Ilnicki, E. I.; Rakic, M. *Chem. Mater.* **1999**, *11*, 1853.

(101) Hou, Y.; Bardo, A. M.; Martinez, C.; Higgins, D. A. *J. Phys. Chem. B* **2000**, *104*, 212.

(102) Deye, J. F.; Berger, T. A.; Anderson, A. G. *Anal. Chem.* **1990**, *62*, 615.

(103) Dutta, A. K.; Kamada, K.; Ohta, K. *J. Photchem. Photobiol. A* **1996**, *93*, 57.

(104) Sarkar, N.; Das, K.; Nath, D. N.; Bhattacharyya, K. *Langmuir* **1994**, *10*, 326.

(105) Brunschwig, B. S.; Ehrenson, S.; Sutin, N. *J. Phys. Chem.* **1987**, *91*, 4714.

(106) Marcus, R. A. *J. Chem. Phys.* **1965**, *43*, 1261.

(107) Marcus, R. A. *J. Phys. Chem.* **1990**, *94*, 4963.

(108) Reichardt, C. *Chem. Rev.* **1994**, *94*, 2319.

(109) Reichardt, C. *Solvents and Solvent Effects in Organic Chemistry*; Wiley-VCH: Weinheim, 2003.

(110) Frenkel-Mullerad, H.; Avnir, D. *Chem. Mater.* **2000**, *12*, 3754.

(111) Tang, Y.; Tehan, E. C.; Tao, Z.; Bright, F. V. *Anal. Chem.* **2003**, *75*, 2407.

(112) Fyfe, C. A.; Aroca, P. P. *J. Phys. Chem. B* **1997**, *101*, 9504.

(113) Iler, R. K. *The Chemistry of Silica*; John Wiley and Sons: New York, 1979.

(114) Ong, S.; Zhao, X.; Eisenthal, K. B. *Chem. Phys. Lett.* **1992**, *191*, 327.

(115) Meziani, M. J.; Zajac, J.; Jones, D. J.; Partyka, S.; Roziere, J.; Auroux, A. *Langmuir* **2000**, *16*, 2262.

(116) Inaki, Y.; Yoshida, H.; Yoshida, T.; Hattori, T. *J. Phys. Chem. B* **2002**, *106*, 9098.

(117) Yang, H.; Coombs, N.; Sakolov, I.; Ozin, G. A. *Nature* **1996**, *381*, 589.

(118) Fu, Y.; Collinson, M. M.; Higgins, D. A. *J. Am. Chem. Soc.* **2004**, *126*, 13838.

(119) Brasselet, S.; Moerner, W. E. *Single Mol.* **2000**, *1*, 17.

(120) Whitaker, J. E.; Haugland, R. P.; Prendergast, F. G. *Anal. Biochem.* **1991**, *194*, 330.

(121) Lee, J. E.; Saavedra, S. S. *Anal. Chim. Acta* **1994**, *285*, 265.

(122) Yang, L.; Saavedra, S. S. *Anal. Chem.* **1995**, *67*, 1307.

(123) Mei, E.; Bardo, A. M.; Collinson, M. M.; Higgins, D. A. *J. Phys. Chem. B* **2000**, *104*, 9973.

(124) Akbarian, F.; Dunn, B. S.; Zink, J. I. *J. Phys. Chem.* **1995**, *99*, 3892.

(125) Kneipp, K.; Wang, Y.; Kneipp, H.; Perelman, L. T.; Itzkan, I.; Dasari, R. R.; Feld, M. S. *Phys. Rev. Lett.* **1997**, *78*, 1667.

(126) Kobayashi, H.; Nakanishi, K.; Minakuchi, H.; Ishizika, N. *Anal. Chem.* **2001**, *73*, 420A.

(127) Nie, S. M.; Emery, S. R. *Science* **1997**, *275*, 1102.

(128) Somers, R. C.; Bawendi, M. G.; Nocera, D. G. *Chem. Soc. Rev.* **2007**, *36*, 579.

(129) Szymanski, C.; Wu, C.; Hooper, J.; Salazar, M. A.; Perdomo, A.; Dukes, A.; McNeill, J. *J. Phys. Chem. B* **2005**, *109*, 8543.

(130) Tomasulo, M.; Yildiz, I.; Raymo, F. M. *J. Phys. Chem. B* **2006**, *110*, 3853.

(131) Michaels, A. M.; Nirmal, M.; Brus, L. E. *J. Am. Chem. Soc,* **1999**, *121*, 9932.

(132) Kaji, H.; Nakanishi, K.; Soga, N.; Inoue, T.; Nemoto, N. *J. Sol-Gel Sci. Technol.* **1994**, *3*, 169.

(133) Nakanishi, K.; Kanamori, K. *J. Mater. Chem.* **2005**, *15*, 3776.

(134) Nakanishi, K.; Tanaka, N. *Acc. Chem. Res.* **2007**, *40*, 863.

(135) Dong, H.; Brook, M. A.; Brennan, J. D. *Chem. Mater.* **2005**, *17*, 2807.

(136) Dong, H.; Ye, F.; Higgins, D. A.; Collinson, M. M. *Chem. Mater.* **2007**, *19*, 6528.

(137) Kuyper, C. L.; Budzinski, K. L.; Lorenz, R. M.; Chiu, D. T. *J. Am. Chem. Soc.* **2006**, *128*, 730.

(138) Grosso, D.; Balkenende, A. R.; Albouy, P. A.; Ayral, A.; Amenitsch, H.; Babonneau, F. *Chem. Mater.* **2001**, *13*, 1848.

(139) Grosso, D.; Balkenende, A. R.; Albouy, P. A.; Lavergne, M.; Mazerolles, L.; Babonneau, F. *J. Mater. Chem.* **2000**, *10*, 2085.

(140) Hernandez, R.; Franville, A.-C.; Minoofar, P.; Dunn, B.; Zink, J. I. *J. Am. Chem. Soc.* **2001**, *123*, 1248.

(141) Huang, M. H.; Dunn, B. S.; Soyez, H.; Zink, J. I. *Langmuir* **1998**, *14*, 7331.

(142) Lu, Y.; Ganguli, R.; Drewien, C. A.; Anderson, M. T.; Brinker, C. J.; Gong, W.; Guo, Y.; Soyez, H.; Dunn, B.; Huang, M. H.; Zink, J. I. *Nature* **1997**, *389*, 364.

(143) Tolbert, S. H.; Schäffer, T. E.; Feng, J.; Hansma, P. K.; Stucky, G. D. *Chem. Mater.* **1997**, *9*, 1962.

(144) Yang, H.; Kuperman, A.; Coombs, N.; Mamiche-Afara, S.; Ozin, G. A. *Nature* **1996**, *379*, 703.

(145) Zhao, D.; Yang, P.; Margolese, D. I.; Chmelka, B. F.; Stucky, G. D. *Chem. Communic.* **1998**, 2499.

(146) Liu, N.; Assink, R. A.; Brinker, C. J. *Chem. Communic.* **2003**, 370.

(147) Liu, N.; Assink, R. A.; Smarsly, B.; Brinker, C. J. *Chem. Communic.* **2003**, 1146.

(148) Wong, E. M.; Markowitz, M. A.; Qadri, S. B.; Golledge, S. L.; Castner, D. G.; Gaber, B. P. *Langmuir* **2002**, *18*, 972.

(149) Ferrer, M.; Lianos, P. *Langmuir* **1996**, *12*, 5620.

(150) Ogawa, M. *Langmuir* **1995**, *11*, 4639.

(151) Wirnsberger, G.; Scott, B. J.; Stucky, G. D. *Chem. Communic.* **2001**, 119.

(152) Bae, J. Y.; Jung, J.-I.; Bae, B.-S. *J. Mater. Res.* **2004**, *19*, 2503.

(153) Loerke, J.; Marlow, F. *Adv. Mater.* **2002**, *14*, 1745.

(154) Marlow, F.; McGehee, M. D.; Zhao, D.; Chmelka, B. F.; Stucky, G. D. *Adv. Mater.* **1999**, *11*, 632.

(155) Yang, P.; Wirnsberger, G.; Huang, H. C.; Cordero, S. R.; McGehee, M. D.; Scott, B.; Deng, T.; Whitesides, G. M.; Chmelka, B. F.; Buratto, S. K.; Stucky, G. D. *Science* **2000**, *287*, 465.

(156) Huang, M. H.; Dunn, B. S.; Zink, J. I. *J. Am. Chem. Soc.* **2000**, *122*, 3739.

(157) Minoofar, P. N.; Dunn, B. S.; Zink, J. I. *J. Am. Chem. Soc.* **2005**, *127*, 2656.

(158) Minoofar, P. N.; Hernandez, R.; Chia, S.; Dunn, B.; Zink, J. I.; Franville, A.-C. *J. Am. Chem. Soc.* **2002**, *124*, 14388.

(159) Watson, J.; Zerda, T. W. *Appl. Spectrosc.* **1991**, *45*, 1360.

(160) Seebacher, C.; Hellriegel, C.; Deeg, F.-W.; Brauchle, C.; Altmaier, S.; Behrens, P.; Müllen, K. *J. Phys. Chem. B* **2002**, *106*, 5591.

(161) Qi, Z.-M.; Honma, I.; Zhou, H. *Appl. Phys. Lett.* **2006**, *88*, 0535031.

(162) Wu, J.; Abu-Omar, M. M.; Tolbert, S. H. *Nano Lett.* **2001**, *1*, 27.

(163) Shera, E. B.; Seitzinger, N. K.; Davis, L. M.; Keller, R. A.; Soper, S. A. *Chem. Phys. Lett.* **1990**, *174*, 553.

(164) Zhong, Z.; Lowry, M.; Wang, G.; Geng, L. *Anal. Chem.* **2005**, *77*, 2303.

(165) Schütz, G. J.; Schindler, H.; Schmidt, T. *Biophys. J.* **1997**, *73*, 1073.

(166) Gao, F.; Mei, E.; Lim, M.; Hochstrasser, R. M. *J. Am. Chem. Soc.* **2006**, *128*, 4814.

(167) Betzig, E.; Chichester, R. J. *Science* **1993**, *262*, 1422.

(168) Viteri, C. R.; Gilliland, J. W.; Yip, W. T. *J. Am. Chem. Soc.* **2003**, *125*, 1980.

(169) Weston, K. D.; Carson, P. J.; Metiu, H.; Buratto, S. K. *J. Chem. Phys.* **1998**, *109*, 7474.

(170) Blum, C.; Stracke, F.; Becker, S.; Müllen, K.; Meixner, A. J. *J. Phys. Chem. A* **2001**, *105*, 6983.

(171) Holman, M. W.; Liu, R.; Adams, D. M. *J. Am. Chem. Soc.* **2003**, *125*, 12649.

(172) Zang, L.; Liu, R.; Holman, M. W.; Nguyen, K. T.; Adams, D. M. *J. Am. Chem. Soc.* **2002**, *124*, 10640.

(173) Lu, H. P.; Xie, X. S. *Nature* **1997**, *385*, 143.

(174) Ha, T.; Enderle, T.; Chemla, D. S.; Selvin, P. R.; Weiss, S. *Chem. Phys. Lett.* **1997**, *271*, 1.

(175) Hou, Y.; Higgins, D. A. *J. Phys. Chem. B* **2002**, *106*, 10306.

(176) Petersen, N. O.; Höddelius, P. L.; Wiseman, P. W.; Seger, O.; Magnusson, K.-E. *Biophys. J.* **1993**, *65*, 1135.

(177) Guan, Y.; Zakrevskyy, Y.; Stumpe, J.; Antonietti, M.; Faul, C. F. J. *Chem. Communic.* **2003**, 894.

(178) Zakrevskyy, Y.; Faul, C. F. J.; Guan, Y.; Stumpe, J. *Adv. Func. Mater.* **2004**, *14*, 835.

(179) Koppel, D. E. *Phys. Rev. A* **1974**, *10*, 1938.

(180) Berquier, J.-M.; Nael, P.; Jupille, J.; Jacquiod, C. *J. Sol-Gel Sci and Tech.* **2000**, *19*, 83.

(181) Skluzacek, J. M.; Tejedor, M. I.; Anderson, M. A. *Micropor. Mesopor. Mat.* **2006**, *94*, 288.

(182) Erdman, L.; Rigler, R. *Proc. Nat. Acad Sci. USA* **2000**, *97*, 8266.

(183) Kim, H. D.; Nienhaus, G. U.; T., H.; Orr, J. W.; Williamson, J. R.; Chu, S. *Proc. Nat. Acad Sci. USA* **2002**, *99*, 4284.

(184) Lu, H. P.; Xun, L.; Xie, X. S. *Science* **1998**, *282*, 1877.

(185) Schenter, G. K.; Lu, H. P.; Xie, X. S. *J. Phys. Chem. A* **1999**, *103*, 10477.

(186) Werley, C. A.; Moerner, W. E. *J. Phys. Chem. B* **2006**, *110*, 18939.

(187) Bartko, A. P.; Xu, K.; Dickson, R. M. *Phys. Rev. Lett.* **2002**, *89*, 026101/1.

(188) Lu, C.-Y.; Vanden Bout, D. A. *J. Chem. Phys.* **2006**, *125*, 124701/1.

(189) Wei, C.-Y. J.; Kim, Y. H.; Darst, R. K.; Rossky, P. J.; Vanden Bout, D. A. *Phys. Rev. Lett.* **2005**, *95*, 173001/1.

(190) English, D. S.; Harbron, E. J.; Barbara, P. F. *J. Chem. Phys.* **2001**, *114*, 10479.

(191) Yip, W.-T.; Hu, D.; Yu, J.; Vanden Bout, D. A.; Barbara, P. F. *J. Phys. Chem. A* **1998**, *102*, 7564.

(192) Petersen, N. O. *Biophys. J.* **1986**, *49*, 809.

(193) Petersen, N. O.; Johnson, D. C.; Schlesinger, M. J. *Biophys. J.* **1986**, *49*, 817.

(194) Costantino, S.; Comeau, J. W. D.; Kolin, D. L.; Wiseman, P. W. *Biophys. J.* **2005**, *89*, 1251.

(195) Digman, M. A.; Brown, C. M.; Sengupta, P.; Wiseman, P. W.; Horwitz, A. R.; Gratton, E. *Biophys. J.* **2005**, *89*, 1317.

(196) Nishimura, G.; Kinjo, M. *Anal. Chem.* **2004**, *76*, 1963.

(197) Rigler, R.; Mets, Ü.; Widegren, J.; Kask, P. *Eur. Biophys. J.* **1993**, *22*, 169.

(198) Hebert, B.; Costantino, S.; Wiseman, P. W. *Biophys. J.* **2005**, *88*, 3601.

(199) Aragón, S. R.; Pecora, R. *J. Chem. Phys.* **1976**, *64*, 1791.

(200) Ludes, M. D.; Wirth, M. J. *Anal. Chem.* **2002**, *74*, 386.

(201) Axelrod, D. *Biophys. J.* **1979**, *26*, 557.

(202) Ha, T.; Laurence, T. A.; Chemla, D. S.; Weiss, S. *J. Phys. Chem. B* **1999**, *103*, 6839.

(203) Balss, K. M.; Coleman, B. D.; Lansford, C. H.; Haasch, R. T.; Bohn, P. W. *J. Phys. Chem. B* **2001**, *105*, 8970.

(204) Wohland, T.; Rigler, R.; Vogel, H. *Biophys. J.* **2001**, *80*, 2987.

(205) Chaudhury, M. K.; Whitesides, G. M. *Science* **1992**, *256*, 1539.

(206) Morgenthaler, S.; Lee, S.; Zurcher, S.; Spencer, N. D. *Langmuir* **2003**, *19*, 10459.

(207) Ueda-Yukoshi, T.; Matsuda, T. *Langmuir* **1995**, *11*, 4135.

(208) Yu, X.; Wang, Z.; Jiang, Y.; Zhang, X. *Langmuir* **2006**, *22*, 4483.

(209) Shea, K. J.; Loy, D. A. *Chem. Mater.* **2001**, *13*, 3306.

(210) Shirtcliffe, N. J.; McHale, G.; Newton, M. I.; Perry, C. C. *Langmuir* **2003**, *19*, 5626.

(211) Yuan, Z.-Y.; Su, B.-L. *J. Mater. Chem.* **2006**, *16*, 663.

(212) Nakanishi, K. *J. Porous Mater.* **1997**, *4*, 67.

(213) Loy, D. A.; Baugher, B. M.; Baugher, C. R.; Schneider, D. A.; Rahimian, K. *Chem. Mater.* **2000**, *12*, 3624.

(214) Baney, R. H.; Itoh, M.; Sakakibara, A.; Suzuki, T. *Chem. Rev.* **1995**, *95*, 1409.

(215) Dong, H.; Brennan, J. D. *Chem. Mater.* **2006**, *18*, 4176.

(216) Dong, H.; Lee, M.; Thomas, R. D.; Zhang, Z.; Reidy, R. F.; Mueller, D. W. *J. Sol-Gel Sci. Techn.* **2003**, *28*, 5.

(217) Devreux, F.; Boilot, J. P.; Chaput, F.; Lecomte, A. *Phys. Rev. A* **1990**, *41*, 6901.

(218) Kanamori, K.; Ishizuka, N.; Nakanishi, K. *J. Sol-Gel. Sci and Tech.* **2003**, *26*, 157.

(219) Rankin, S. E.; Macocko, C. W.; McCormick, A. V. *AIChE J.* **1998**, *44*, 1141.

(220) Sanchez, J.; Rankin, S. E.; McCormick, A. V. *Ind. Eng. Chem. Res.* **1996**, *34*, 117.

(221) Smått, J.-H.; Schunk, S.; Lindén, M. *Chem. Mater.* **2003**, *15*, 2354.

(222) Kanamori, K.; Yonezawa, H.; Nakanishi, K.; Hirao, K.; Jinnai. *J. Sep. Sci.* **2004**, *27*, 874.

(223) Boukari, H.; Lin, J. S.; Harris, M. T. *Chem. Mater.* **1997**, *9*, 2376.

(224) Born, M.; Wolf, E. *Principles of Optics*; Cambridge University Press: Cambridge, 1998.

(225) Ye, F.; Collinson, M. M.; Higgins, D. A. *Anal. Chem.* **2007**, *79*, 6465.

(226) Alam, T. M.; Assink, R. A.; Loy, D. A. *Chem. Mater.* **1996**, *8*, 2366.

(227) Beck, R. E.; Schultz, J. S. *Science* **1970**, *170*, 1302.

(228) Cabrera, C. R.; Finlayson, B.; Yager, P. *Anal. Chem.* **2000**, *73*, 658.

(229) Dertinger, S. K. W.; Jiang, X.; Li, Z.; Murthy, V. N.; Whitesides, G. M. *Proc. Nat. Acad. Sci. USA* **2002**, *99*, 12542.

(230) Genzer, J.; Bhat, R. R. *Langmuir* **2008**, *24*, 2294.

(231) May, E. L.; Hillier, A. C. *Anal. Chem.* **2005**, *77*, 6487.

(232) Morgenthaler, S.; Zink, C.; Spencer, N. D. *Soft Matter* **2008**, *4*, 419.

(233) Neubrand, A. *J. Appl. Electrochem.* **1998**, *28*, 1179.

(234) Plummer, S. T.; Bohn, P. W. *Langmuir* **2002**, *18*, 4142.

(235) Terrill, R. H.; Balss, K. M.; Zhang, Y.; Bohn, P. W. *J. Am. Chem. Soc.* **2000**, *122*, 988.

(236) Wang, X.; Haasch, R. T.; Bohn, P. W. *Langmuir* **2005**, *21*, 8452.

(237) Senkan, S. *Angew. Chem. Int. Ed.* **2001**, *40*, 312.

(238) Liedberg, B.; Tengvall, P. *Langmuir* **1995**, *11*, 3821.

(239) Mougin, K.; Ham, A. S.; Lawrence, M. B.; Fernandez, E. J.; Hillier, A. C. *Langmuir* **2005**, *21*, 4809.

(240) Wang, Q.; Jakubowski, J. A.; Sweedler, J. V.; Bohn, P. W. *Anal. Chem.* **2004**, *76*, 1.

(241) Wijesundara, M. B. J.; Fuoco, E.; Hanley, L. *Langmuir* **2001**, *17*, 5721.

(242) Tomlinson, M. R.; Efimenko, K.; Genzer, J. *Macromolecules* **2006**, *39*, 9049.

(243) Xu, C.; Wu, T.; Mei, Y.; Drain, C. M.; Batteas, J. D.; Beers, K. L. *Langmuir* **2005**, *21*, 11136.

(244) Elwing, H.; Welin, S.; Askendal, A.; Nilsson, U.; Lundstrom, I. *J. Colloid Interface Sci.* **1987**, *119*, 203.

(245) Thierry, T.; Bruno, B.; Christian, F. *J. Appl. Polym. Sci.* **2007**, *104*, 1504.

(246) Hecht, E. *Optics*; Addison-Wesley: Reading, Massachusetts, 1987.

(247) Nishida, F.; McKiernan, J. M.; Dunn, B.; Zink, J. I.; Brinker, C. J.; Hurd, A. J. *J. Am. Ceram. Soc.* **1995**, *78*, 1640.

(248) Huang, J.; Fan, R.; Connor, S.; Yang, P. *Angew. Chem. Int. Ed* **2007**, *46*, 2414.

(249) Deegan, R. D.; Bakajin, O.; Dupont, T. F.; Huber, G.; Nagel, S. R.; Witten, T. A. *Nature* **1997**, *389*, 827.

(250) Ye, F.; Collinson, M. M.; Higgins, D. A. *Phys. Chem. Chem. Phys.* **2009**, *11*, 66.